




University of
Stavanger

Faculty of Science and Technology

MASTER'S THESIS

Study program/Specialization: Mathematics and Physics	Spring semester, 2021 Open / Restricted access
Writer: Tina Knudsen	 (Writer's signature)
Faculty supervisor: Olena Zavorotynska External supervisor(s): Smagul Karazhanov, Elbruz Murat Baba	
Thesis title: Study of Photochromic Effect in Yttrium Oxyhydride Films	
Credits (ECTS): 60	
Key words: Photochromic materials, oxyhydrides, mixed-anion materials, materials physics, Raman spectroscopy, X-ray diffraction	Pages: 74 + enclosure: 23 Stavanger, 15/06/2021 Date/year

UNIVERSITY OF STAVANGER

DEPARTMENT OF MATHEMATICS AND PHYSICS

**Study of Photochromic Effect in Yttrium
Oxyhydride Films**

Author

Tina KNUDSEN

Supervisors

Assoc. Prof. Olena ZAVOROTYNSKA

Dr. Smagul KARAZHANOV

Dr. Elbruz M.BABA

June 15, 2021

Abstract

Mixed anion compounds have multiple different anions as part of their structure. Due to the different nature of individual anions the mixed anion compounds may exhibit other properties than the well known single-anion compounds (examples being oxides and hydrides). One group of the relatively new field of mixed anion compounds is the oxyhydrides. The oxyhydrides contain both H^- and O^{2-} anions. In this work yttrium oxyhydride (YHO), regarded as one of the rare-earth oxyhydrides (RE-O-H), was studied. This compound had already been observed to have interesting photochromic (PC) properties when illuminated by UV and visible light. A complete understanding on the origin of the PC effect and its limitations had although not yet been established.

The aim of this thesis was to study thin films of YHO on glass before and after UV-illumination to understand more of the color changing mechanism. Thin films of YHO deposited by reactive magnetron sputtering were studied by the methods of Raman spectroscopy, X-ray diffraction (XRD) and cyclic optical testing. Some films coated with thin layers of palladium (Pd) were studied with regards to electrical resistivity as well. The latter was an attempt on revealing whether hydrogen diffusion takes part in the photo-darkening. The electrical measurements were performed with a four point probe.

The thin films of YHO were observed to easily burn when exposed to lasers of wavelength 532 and 633 nm. From Raman measurements within the damaged spots on the film it was clear that the sample had been destroyed by the lasers. Thus, a large part of this work was related to optimizing the measurement conditions for Raman spectroscopy. The Raman peaks of the obtained spectra before and after UV exposure were assigned by literature study on similar compounds and factor group analysis (FGA).

The average grain size of the films was estimated by the Scherrer equation from the diffractograms obtained by XRD. Average grain size was shown to decrease with increasing deposition pressure. The experimental diffraction patterns were compared to reference patterns of yttrium hydrides and yttria in addition to theoretical patterns of different YHO structures. Raman and XRD showed possible hydrogen distortion after UV-illumination performed in Ar atmosphere and the possibility of multiple crystal structures present.

Contents

Abstract	1
Contents	1
Preface	4
Acknowledgements	5
1 Introduction	8
1.1 Thesis purpose	8
1.2 Background	8
2 Theory	11
2.1 Magnetron Sputtering	11
2.2 Raman Spectroscopy	13
2.2.1 Origin and Intensity of Raman	13
2.2.2 Factor group analysis	18
2.2.3 Instrumentation	20
2.3 Cyclic Optical Testing	21
2.4 Four Point Probe	22
2.5 X-Ray Diffraction	24
2.5.1 Diffraction geometry	24
2.5.2 The diffraction pattern	25
2.5.3 Scherrer Equation	28
3 Methods	31
3.1 Reactive Magnetron Sputtering	31
3.2 Setup and Procedure	32
3.2.1 Raman Spectroscopy	32
3.2.2 Cyclic Optical Testing	33
3.2.3 UV-Illumination	34
3.2.4 Four Point Probe	35
3.2.5 XRD	36

4	Results and Discussion	38
4.1	Raman Measurements	38
4.1.1	FGA and Literature Study	39
4.1.2	Optimisation of measurement conditions	42
4.1.3	Raman spectra of films before illumination	46
4.1.4	Effect from UV on glass	50
4.1.5	Raman of UV-illuminated samples	51
4.2	Cyclic Optical testing	55
4.3	Electrical measurements	57
4.4	XRD	59
4.4.1	Diffraction pattern	59
4.4.2	Grain size estimation	63
5	Conclusions	65
	Bibliography	66
	List of Figures	73
	List of Tables	77
	Appendices	78
A	Additional Raman spectra	78
B	Factor group analysis	82
C	Grain size estimation	85
D	Electrical measurements data	89

Preface

This thesis completes a Master's degree in Mathematics and Physics from the University of Stavanger (UiS). The thesis is given as a part of the Complex of Online and Onsite Lectures on Materials for Hydrogen Generation by Solar Water Splitting (COOL LONGBOAT). The project leader of COOL LONGBOAT is Dr. Smagul Karazhanov, senior researcher from Institute for Energy Technology (IFE).

The measurements and data analysis in the Master project have been performed by me at UiS and IFE with supervision from Associate Professor Olena Zavorotynska, Dr. Elbruz M. Baba, Mr. Damir Z. Mamedov and Senior engineer Chang C. You. The different samples of YHO used for measurements had been prepared in advance by reactive magnetron sputtering by Elbruz M. Baba and Chang C. You at IFE. Some samples were capped with palladium (Pd) by Dr. Jeyanthinath Mayandi at the University of Oslo (UiO) due to issues with the sputter machine at IFE at that time. Therefore, I was not able to get an introduction to the sample preparation processes during my stay at IFE as planned.

The thesis aims at an audience with background in physics at a master's level, but without considerable knowledge of oxyhydrides and the experimental methods utilized.

TINA KNUDSEN
June 2021
Stavanger, Norway

Acknowledgements

I will sincerely thank my supervisor Olena Zavorotynska, Associate Professor in Materials Physics at the University of Stavanger (UiS). It has been a pleasure to work with you during two full semesters. Your guidance in the laboratory and constructive way of supervising me through the project have really been appreciated. I cannot imagine doing the master project without you as my supervisor.

I want to express my gratitude to my co-supervisors Dr. Smagul Karazhanov and Dr. Elbruz Murat Baba from IFE. Thank you for your guidance and for fruitful discussions. Your knowledge, proficiency and dedication have inspired me to work hard and be curious.

I also want to acknowledge Senior Engineer Chang Chuan You (IFE) and Mr. Damir Zamirovich Mamedov for offering me training in necessary instruments for the project. Thank you Dr. Jeyanthinath Mayandi, for coating our samples with Pd.

Then, I would like to thank the people in the solar corridor at IFE for being so welcoming to me as a visiting student. I am thankful for your hospitality despite the situation of Covid-19.

I would also like to thank the people at the Department of Mathematics and Physics (DMF) at UiS for arranging enlightening seminars and social events during my five year studies. I am left with the feelings of appreciation and joy for choosing DMF for my studies.

Finally, I will thank my husband, Kristian Dyrnes, for always supporting me and for cheering my work from start to finish.

Thank you.

Abbreviations and constants

The collection of abbreviations and their full expressions used throughout the thesis are listed alphabetically. Scientific constants are listed as well.

Al	Aluminium
Ar	Argon
CCD	Charge-coupled device
COOL LONGBOAT	Complex of Online and Onsite Lectures on Materials for Hydrogen Generation by Solar Water Splitting
DC	Direct Current
fcc	Face centered cubic
Fig.	Figure
FGA	Factor group analysis
FWHM	Full width at half maximum
H	Hydrogen
ICDD	International Centre for Diffraction Data
IFE	Institute for Energy Technology
DMF	Department of Mathematics and Physics
IR	Infrared
NA	Numerical aperture
No.	Number
O	Oxygen
SPGN	Space group number
PC	Photochromic
Pd	Palladium

P_d	Deposition pressure
PDF	Powder diffraction file
PL	Photoluminescence
ppm	Parts per million
RE	Rear-earth
RE-O-H	Rear-earth oxyhydride
ref	Reference
RF	Resonance Fluorescence
RR	Resonance Raman
sccm	Standard cubic centimeters per minute
UV	Ultraviolet
UiO	University of Oslo
UiS	University of Stavanger
WD	Working distance
WP	Wyckoff position
Y	Yttrium
YHO	Yttrium oxyhydride
XRD	X-ray diffraction
<i>c</i>	Speed of light in vacuum
<i>n</i>	Refractive index of air
<i>h</i>	Planck's constant
<i>k</i>	Boltzmann constant
<i>K</i>	Scherrer constant

Chapter 1

Introduction

1.1 Thesis purpose

The aim of this thesis was to study thin films of the photochromic mixed-anion compound yttrium oxyhydride (YHO). The goal was to understand more about the underlying reason for the photodarkening when the compound is exposed to ultraviolet light on the atomic scale. A large part of the work was also intended to learn how to operate different instruments such as the Raman microscope and the X-ray diffractometer, to subsequently process and analyze the obtained data, and finally, relate it to the theory. The motivation for studying YHO was the broad range of its potential applications. It can, e.g., be used in smart windows, energy storage devices and sensors. [1]–[3]. Thus, this study gives further insight into a relevant compound for up-to-date applications.

1.2 Background

In materials physics there are some compounds that contain several different anions. An unifying term is the mixed anion compounds. Compared to single anion compounds, the study of the mixed anion compounds is relatively new, being only "in its infancy" by 2018 according to Kageyama *et al.* [4]. The fact that individual anions differ in nature with regards to properties like e.g. electronegativity, polarizability and charge makes the structure of a mixed anion compound more complex than single anion structures. In the same paper from 2018 two interesting properties of the hydrogen anion is explained. It is shown that H^- is both flexible in size and a labile ligand. Hence, it can adapt to many different atomic and molecular environments and allow for anionic conductivity. The properties of size flexibility and good adaptability of H^- stands for the case when both H^- and O^{-2} anions are present in a compound. Such compounds are called oxyhydrides and contain both hydrogen and oxygen anions in addition to metal cations [4].

The rear-earth oxyhydrides can generally be written in short form as RE-O-H or expressed by $\text{REO}_x\text{H}_{3-2x}$ allowing for different stoichiometries, where $x \in [0.5, 1.5]$ [5], [6]. The value

of x affects the properties of the RE-O-H and depends on the working parameters of sample preparation and further oxidation [7]. When a RE-O-H is prepared as a thin film the color of the film changes for different values of x [5]. Also, the unit cell volume depends on the value of x as the two anions have different atomic radii and charge.

One of the very interesting RE oxyhydrides is the yttrium oxyhydride (YHO). It is composed of hydrogen and oxygen anions and the RE element yttrium (Y). Y has atomic number 39 and the electronic configuration $[\text{Kr}]4d^15s^2$. When Y is ionized to Y^{3+} it bonds independently with H^- and O^{2-} and together they constitute the mixed anion compound YHO. Even though, the Y^{3+} is "the most favourable" ionic state for YHO, some cations of the compound may be less ionized, according to ref [3]. Thin films of YHO have been observed to have very interesting properties when exposed to ultraviolet (UV) and visible light [8]. The origin of one of the most studied properties, photochromism, has not yet been established [5], [9].

The pioneering work which brought YHO into the research spotlight was published in 1996 by Huiberts *et al.* [10]. Their study reported a switchable transparency for thin films of yttrium hydride when tuning the concentration of hydrogen [10], [11]. Starting with pure yttrium, they observed a shiny metallic appearance for the film. Adding hydrogen to obtain YH_2 they still observed the reflective mirror properties. Adding more hydrogen to the film at a pressure of 10^5 Pa obtaining YH_3 they observed a clear change towards transparent properties. These results showed a great potential for smart windows by the use of $\text{YH}_2 \longleftrightarrow \text{YH}_3$ transition. A challenge to this application was the sensitivity of the yttrium hydride to air. The presence of oxygen in yttrium hydride films became of great interest after accidental oxidation of the films in air. The oxidation of thin films of yttrium hydride resulted in thin films of YHO with stable transparent properties. The first believed cause for the oxygen present in the films was the incorporation of oxygen inside the sputtering chamber [12], which actually occurred simply due to exposure of the films to air [13]–[15].

Thin films of YHO have later been observed to possess photochromic (PC) properties when illuminated with UV and visible light under normal pressure and temperature conditions [16]–[18]. Both green and red light has been observed to induce photodarkening. Green light of wavelength 532 nm (2.33 eV) affects the film more than red light of wavelength 623 nm (1.99 eV) [18]. Montero *et al.* have shown that the degree of transmittance of the YHO sample decreases with increasing illumination time. They proposed a formation of metallic domains within the clear state of YHO under illumination as a reason for the photo darkening [16]. When thin films of YHO were removed from the light source they restored their initial color and transparency with time [17]. The bleaching time of YHO has been shown to depend on the amount of oxygen contained in the surrounding atmosphere. The term bleaching is used for the process when the photodarkened film restores its initial transparency. It has been proposed that oxygen diffusion or oxygen exchange plays a role in the PC phenomenon [8], [16]. Another property of YHO influenced by UV-radiation is the dimensions of the crystal lattice. YHO with a cubic structure and lattice parameter $a = 5.34 \text{ \AA}$ has been shown to contract upon UV-radiation in which the

lattice parameter changed to $a = 5.20 \text{ \AA}$ [8]. When removing the illumination source, the unit cell restores its dimensions (in an expansion process) [8], [17]. This cycle of contraction and expansion during illumination and bleaching of YHO was proposed to be due to oxygen diffusion or oxygen exchange which stabilizes when oxygen again is incorporated. This phenomenon has been referred to as "breathing" by E. M Baba *et al.* [8]. Most recently, in the work of Moro *et al.* [9], an unchanged PC response for encapsulated YHO thin films was reported. Thus, the proposed role of oxygen transport (between thin film and surrounding environment) in the PC process in YHO can be debated. Moreover, since the capping materials were oxygen and hydrogen free, any material transport to or from the thin film as a reason for the photodarkening should be up for discussion [9].

YHO can be studied when prepared as e.g. thin films. The thin films of YHO can be prepared by the process of reactive magnetron sputtering [13] as discussed in section 2.1. In this work, four thin films of YHO deposited onto glass substrates were studied by Raman spectroscopy before and after illumination with UV-light. YHO thin films were also studied by X-ray diffraction (XRD), cyclic optical testing and four point probe measurements.

Chapter 2

Theory

This section includes the theoretical background for the experimental techniques employed. Among others, Raman spectroscopy was used in order to gain information about structural properties of YHO before and after illumination by UV-light. Cyclic optical testing was performed in order to study the PC effect i.e., the PC contrast, due to UV-illumination. Electrical measurements were made with a four-point probe before and after illumination. XRD was used to assign the crystallographic phase and to determine the average grain size of the samples prepared with different deposition pressures.

2.1 Magnetron Sputtering

The thin films of YHO were prepared at the Institute of Energy Technology (IFE) by reactive magnetron sputtering. This is a two step process which includes an initial sputter deposition of YH_x onto a glass substrate followed by an oxidation in air [13], [19].

In the reactive magnetron sputtering process, the atoms of the target material are sputtered off due to ionized gas molecules bombarding the target. The kinetics of the sputtered atoms include energies up to 10 eV and a cosine angular distribution. This distribution can be illustrated as a circle (or a sphere in three dimensions) showing the relative number of sputtered atoms in any direction. Whether the sputtered atoms follow the cosine angular distribution or not can be affected if the incident ion has lower or higher energy resulting in wider or narrower emission distribution (shown in Fig. 2.1) [20]. For an atom of the target to be sputtered, a physical momentum exchange has to occur. Stroke by an incident ion the target atom transfers momentum to its surrounding atoms resulting in fur-

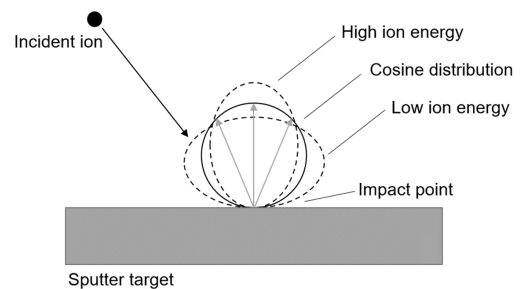


Figure 2.1: Simplified model of angular emission distribution for sputtered atoms [20].

ther collisions. Some of the target atoms close to the surface obtain enough momentum in the outward direction to get sputtered (shown in Fig. 2.2) [21].

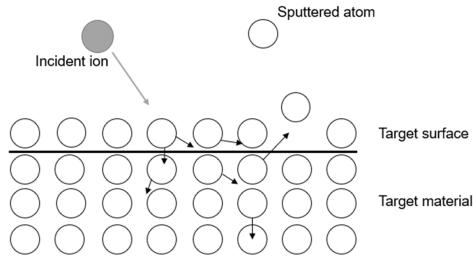


Figure 2.2: Magnetron sputtering illustrated on the atomic scale.

The sputtered atoms from the target material appear in the plasma between a magnetron cathode and anode which are directly connected to a power circuit. This makes it a Direct Current (DC) Sputtering process. The atoms in the plasma get deposited onto a chosen substrate in the form of a thin film due to condensation.

In a sputtering process there are many important parameters that can be adjusted in order to produce specific thin films. For thicker films the process may be left for longer and for changes in density and electrical resistivity the working pressure can be adjusted. E.g. as the deposition pressure is increased the density of the film decreases [20].

A schematic of the DC Magnetron Sputtering is shown in Fig. 2.3. The cathode and anode setup is directly connected to a current which creates a magnetic field surrounding the target material. The substrate is mounted on top of the anode, and the target is placed at the cathode side of the setup.

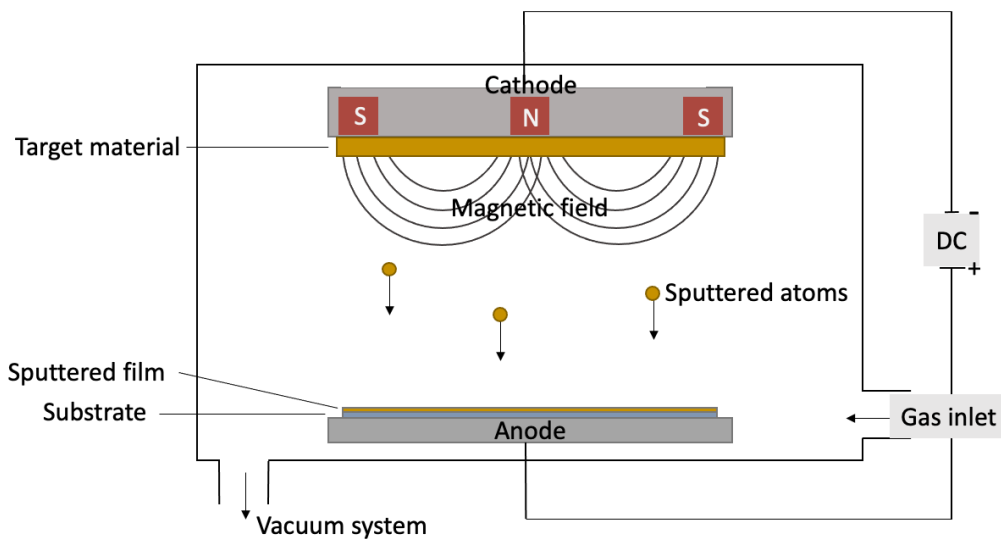


Figure 2.3: Schematic of the DC Magnetron Sputtering. Illustration inspired by [22].

2.2 Raman Spectroscopy

The Raman effect occurs due to the inelastic scattering of light in matter [23]. Depending on the change in polarization of the molecule induced by a laser, the scattered light from the sample may have a small shift in energy compared to the incident laser. This small change in energy, measured in wavenumbers ω , is what is known as the Raman effect, first explained and published in 1928 by C.V. Raman [24] and K.S. Krishnan [25]. Raman spectroscopy includes a source of intense monochromatic light in the UV-visible part of the electromagnetic spectrum. The laser beam which irradiates the sample propagate in the direction perpendicular to the scattered light detected. This geometry originates from a filter positioned at the entrance. The filter acts like a dichroic beam splitter. This means that its properties depend on the incident laser's wavelength. The filter reflects the incoming laser beam in the direction of the sample while the Raman light from the sample is transmitted [26]. More details about the Raman instrument used in this study are provided in section 2.2.3. Lasers are used to detect shifts in the frequency of light due to interaction between incident light with matter. This interaction distorts the electron clouds which induces polarization of the molecules resulting in Raman activity [26], [27, p. 30].

2.2.1 Origin and Intensity of Raman

Using the theory of classical electromagnetism one can describe the origin of Raman scattering by deriving the dipole moment μ . Following the same steps as ref [27, pp. 6–7], an incident light wave with amplitude E_0 and frequency ν is given by

$$E = E_0 \cos 2\pi\nu t, \quad (2.1)$$

where t is time. When a molecule (diatomic) is exposed to the light, it gets an induced dipole moment μ expressed by the product of the light wave (in the form of the electromagnetic wave E) and a polarizability factor α :

$$\mu = \alpha E. \quad (2.2)$$

The polarizability is a second rank tensor (3x3 matrix) with components α_{ij} .

A molecular vibration of frequency ν_i accounts for a nuclear displacement q given by

$$q = q_0 \cos 2\pi\nu_i t, \quad (2.3)$$

with q_0 being the amplitude of the vibration. In the case of vibrations of smaller amplitude the polarizability can be expressed as a function of the nuclear displacement. Then α can be approximated from a truncated Taylor (Maclaurin) expansion to first power:

$$\alpha = \alpha_0 + \left(\frac{\partial \alpha}{\partial q} \right)_0 q, \quad (2.4)$$

where the first term is the equilibrium polarizability and the second term represents the rate of change of the polarizability with respect to the nuclear displacement q . Meant by the equilibrium polarization, is the initial polarizability of the molecule. From Eqs. 2.2-2.4 the final expression for the dipole moment is

$$\begin{aligned}\mu &= \left[\alpha_0 + \left(\frac{\partial \alpha}{\partial q} \right)_0 q \right] E_0 \cos 2\pi \nu t \\ &= \alpha_0 E + \frac{1}{2} \left(\frac{\partial \alpha}{\partial q} \right)_0 q_0 E_0 [\cos 2\pi(\nu + \nu_i)t + \cos 2\pi(\nu - \nu_i)t].\end{aligned}\tag{2.5}$$

In Eq. 2.5 the first term describes the Rayleigh scattering and the second term the Raman scattering. From this equation one sees that in order for the scattering to be Raman-active, the molecule has to have a change in polarizability during the vibration. If not $(\partial \alpha / \partial q)_0 = 0$ and the Raman scattering disappears from the equation. This criterion constitutes a selection rule for the Raman scattering [28, p. 24], saying that at least one of the components of the polarizability tensor has to change during the molecular vibration for it to be Raman active [27, p. 32].

We have the cases of Stokes Raman scattering (increased ω) and anti-Stokes (decreased ω) Raman scattering [29, p. 122], shown by the first and second term of the Raman part of Eq. 2.5, respectively. The Stokes Raman scattering occur when a molecule in the ground vibrational state ν_0 is excited to a virtual state and then relaxes (vibrational relaxation) to e.g. the first excited vibrational state ν_1 . At ambient conditions, when most of molecules are in the ground state, this is the most common Raman scattering. The phenomenon of anti-Stokes Raman scattering occurs when a molecule in an excited vibrational state relaxes back to the ground vibrational state [30], [31]. If there is no difference between the incident and outgoing scattered light, the process is elastic and called Rayleigh scattering. The three different cases of Raman scattering mentioned (Stokes, anti-Stokes and Rayleigh) are illustrated in Fig. 2.4.

The wavenumber and wavenumber shift have units of reciprocal cm from its definition as the inverse of wavelength shown in Eq. 2.6, where c is the speed of light, ν is the frequency of the electromagnetic wave and λ is the wavelength:

$$\omega = c/\nu = 1/\lambda\tag{2.6}$$

When the incident energy from the light source (laser) and the energy of an electronic transition of the atom or molecule match, one gets the situation of resonance Raman scattering (RR) [27, p. 98]. This is manifested as a significant increase in the Raman intensity due to the fact that the electronic transition has a much larger energy than a vibrational transition. If the energy in such case gets absorbed and re emitted by the molecule, scattering light with less energy than the incoming laser, one has the phenomenon of resonance fluorescence (RF) [27, p. 8]. RF is a form for photo luminescence (PL) and will often overshadow the much weaker Raman scattering. In some cases, different substrates show

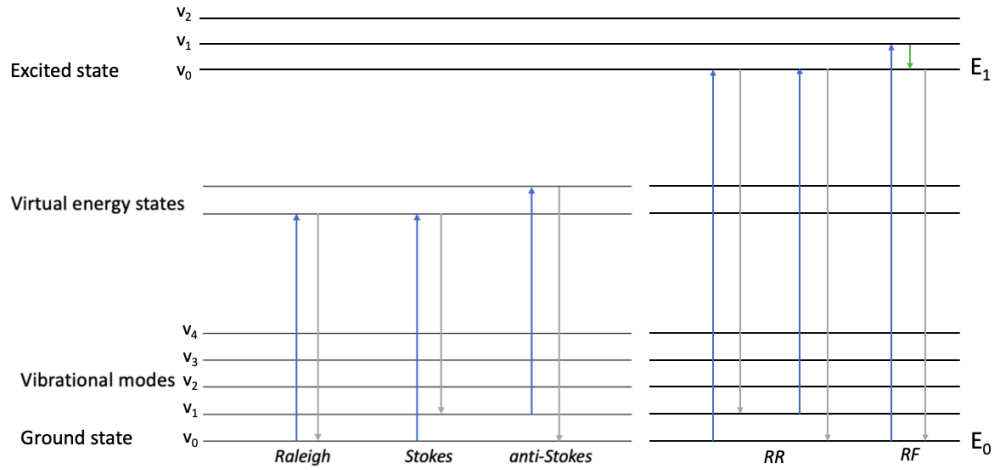


Figure 2.4: The Stokes, anti-Stokes, Rayleigh, resonance Raman (RR) and resonance fluorescence (RF) phenomena illustrated.

fluorescence with specific laser wavelengths. There are, however, methods to avoid this background effect. One possibility is to do measurements with other excitation wavelengths (green or blue lasers) or to change the support substrate of the sample [30], [31]. The RR and RF are illustrated together with the former described effects in Fig. 2.4.

Raman intensity of a measurement depends strongly on the chosen laser and its wavelength. We can derive this relation starting from Eq. 2.5. For simplicity the term for the Stokes radiation is considered only. The dipole moment of the Stokes scattering is then given by

$$\begin{aligned} \mu_{Stokes} &= \frac{1}{2} \left(\frac{\partial \alpha}{\partial q} \right)_0 q_0 E_0 \cos[2\pi(\nu - \nu_i)t] \\ &= \frac{1}{2} \left(\frac{\partial \alpha}{\partial q} \right)_0 q_0 E_0 \cos[(\omega - \omega_i)t], \end{aligned} \quad (2.7)$$

using the relation

$$\omega = 2\pi\nu, \quad (2.8)$$

where ω (omega) is the angular frequency of the incident light. From here, we introduce the power emitted by an ideal dipole, also known as a Hertzian dipole [28]. The ideal dipole models the oscillating induced dipole well with its length being much smaller than the wavelength scale [28, p. 26], [32]. The emitted power from the ideal dipole is proportional to the absolute value of the double time derivative of μ_{Stokes} squared [28]

and is given by

$$\begin{aligned}
 P &= \frac{|\ddot{\mu}|^2}{6\pi\epsilon_0 c^3} \\
 &= \frac{q_0^2}{24\pi\epsilon_0 c^3} \left(\frac{\partial \alpha}{\partial q} \right)_0 (\omega - \omega_i)^4 E_0^2 \cos^2[(\omega - \omega_i)t].
 \end{aligned} \tag{2.9}$$

Doing a time average of the oscillating cosine factor, using the trigonometric identity

$$\sin(a + b) = \sin(a) \cos(b) + \cos(a) \sin(b), \tag{2.10}$$

we get the rest of the proportionality factor of a half:

$$\begin{aligned}
 \langle f(t) \rangle &= \frac{1}{2\pi} \int_t^{t+2\pi} \cos^2(\omega t) dt \\
 &= \frac{1}{2\pi} \left[\frac{2\omega t + \sin(2\omega t)}{4\omega} \right]_t^{t+2\pi} \\
 &= \frac{1}{2\pi} \left[\frac{2\omega(t + 2\pi) + \sin(2\omega t + 4\pi\omega)}{4\omega} - \frac{2\omega t + \sin(2\omega t)}{4\omega} \right] \\
 &= \frac{1}{2}.
 \end{aligned} \tag{2.11}$$

Thus, Eq. 2.9 can be written as

$$P = \frac{q_0^2}{48\pi\epsilon_0 c^3} \left(\frac{\partial \alpha}{\partial q} \right)_0 (\omega - \omega_i)^4 E_0^2. \tag{2.12}$$

The intensity of the Stokes Raman scattering I_{Stokes} detected in a Raman microscope is proportional to the power P of the ideal dipole induced [28, p. 26]. Hence, the important relation between the intensity of Raman scattering and the laser wavelength to the fourth power can be expressed by

$$I_{Stokes} \propto \left(\frac{\partial \alpha}{\partial q} \right)_0 (\omega - \omega_i)^4 E_0^2, \tag{2.13}$$

where

$$\omega = \frac{2\pi}{\lambda} c. \tag{2.14}$$

This classical derivation provides a good understanding of the relation between the intensity of the Raman lines and the laser wavelength, but does not describe the phenomenon of e.g. RR scattering [28, p. 27]. Thus, we need the quantum mechanical theory of light

scattering as the basis for Raman intensity. The following equation for Raman intensity has been derived thoroughly in sections 1.20-1.21 of ref [27]:

$$I_n = KI_0 \frac{(\nu_0 - \nu)^4}{\mu\nu(1 - e^{-h\nu/kT})} [45(\bar{\alpha})^2 + 13\gamma^2], \quad (2.15)$$

where:

K - Summarizing constant (a product of all other constant factors)

I_0 - Intensity of the incident light ($\propto E^2$)

ν_0 - Frequency of the incident light

ν - Frequency of the scattered light (Stokes frequency)

μ - Reduced mass

h - Planck's constant

k - Boltzmann constant

T - Temperature

$\bar{\alpha}$ - Mean value of the polarizability tensor (resulting from the averaging over random orientations for liquid/gas samples)

γ^2 - Anisotropic part of the polarizability averaged over all orientations for liquid/gas samples.

Raman scattering at room temperature usually involves scattering of molecules initially in the ground vibrational state. This is not always the case, so the intensity will, according to the Maxwell-Boltzmann distribution law, depend on the temperature T . As T increases the exponential term of Eq. 2.15 approaches one. Physically the increase of T (above room temperature) makes it more probable for the initial state of the molecule to be above the ground vibrational state. One also sees, as already shown in Eq. 2.13, that the intensity is directly proportional to the fourth power of the incident light frequency. As the incident frequency increases, the Raman intensity increases proportionally. Thus, shorter excitation wavelengths are preferred to obtain stronger Raman peaks. However, there are other dependencies which have to be taken into account when choosing the excitation source. The phenomenon of PL may appear for some wavelengths, but not others. Accordingly, one can agree that the theoretical background for Raman spectroscopy gives a good indication on the parameters of optimal setups, even though it regularly has to be modified for practical reasons.

In the derivation of Eq. 2.15 [27] the average of the polarizability components is considered for the case of randomly oriented molecules, which takes place inside the square brackets of the equation, where

$$\bar{\alpha} = \frac{\text{Tr}(\alpha)}{3} \quad (2.16)$$

and

$$\gamma^2 = 0.5[(\alpha_{xx} - \alpha_{yy})^2 + (\alpha_{yy} - \alpha_{zz})^2 + (\alpha_{zz} - \alpha_{xx})^2 + 6(\alpha_{xy}^2 + \alpha_{yz}^2 + \alpha_{zx}^2)]. \quad (2.17)$$

The vibrational transitions appear in the region of wavenumbers ranging from $\omega = 10^4$ to $\omega = 10^2 \text{ cm}^{-1}$ and originate from vibrating nuclei in molecules [33, p. 5]. The vibrational energies disclosed by Raman spectroscopy can provide information about the phase of the compound, the structure of the molecules and crystal structure of the compound [33], [34].

In a Raman spectrum the wavenumber or Raman shift in units of reciprocal cm is plotted against the intensity of detected scattering. The Raman spectrum will only show lines or peaks for compounds with Raman active modes. Whether a certain compound have Raman active modes or not, is related to the crystal structure of the compound. This important relation will be pointed out in the following section.

2.2.2 Factor group analysis

There is a direct relation between the crystal structure of a compound and its vibrational modes possible to detect with Raman microscopy. The space group of a compound describes its spacial symmetry and includes symmetry operations like translations, screw axes and glide and mirror planes. There are in total 230 different space groups which can be expressed using (at least) two different notations; The Hermann-Mauguin and the Schönflies notation [27]. The Hermann-Mauguin notation is used consistently for the space groups introduced, while the Schönflies notation is more common when referring to point groups and site symmetries (as expressed in Table 4.1).

Table 2.1: Meaning of the Mulliken symbols

Symbol	Describing properties
A	Singly degenerate, symmetric with respect to principal axis
B	Singly degenerate, anti-symmetric with respect to principal axis
E	Doubly degenerate
F (T)	Triply degenerate
1	Symmetric with respect to additional rotations
2	Anti-symmetric with respect to additional rotations
g	Symmetric with respect to inversion through center
u	Anti-symmetric with respect to inversion through center
'	Symmetric with respect to horizontal plane of symmetry
"	Anti-symmetric with respect to horizontal plane of symmetry

Character tables of specific point groups can be used for obtaining necessary information about what impact different symmetry operations have on a compound. The irreducible representations in the first column of a character table, expressed by Mulliken symbols (A, B, E, F, 1, 2, g, u, ' and "), are central for finding Raman active modes. For the Mulliken symbols the capital letters denote degeneracy and symmetry with respect to the principle axis of rotation and the other symbols, appearing as subscripts or superscripts, express the symmetry with respect to mirror planes, inversion centers and additional rotation

axis. An overview of the Mulliken symbols and their meaning is given in Table 2.1. The character tables also contain columns of polarization functions that show which of the modes are having linear or quadratic functions. The linear functions tell about translation in 3 dimensions, while quadratic functions for instance tell if modes are Raman active.

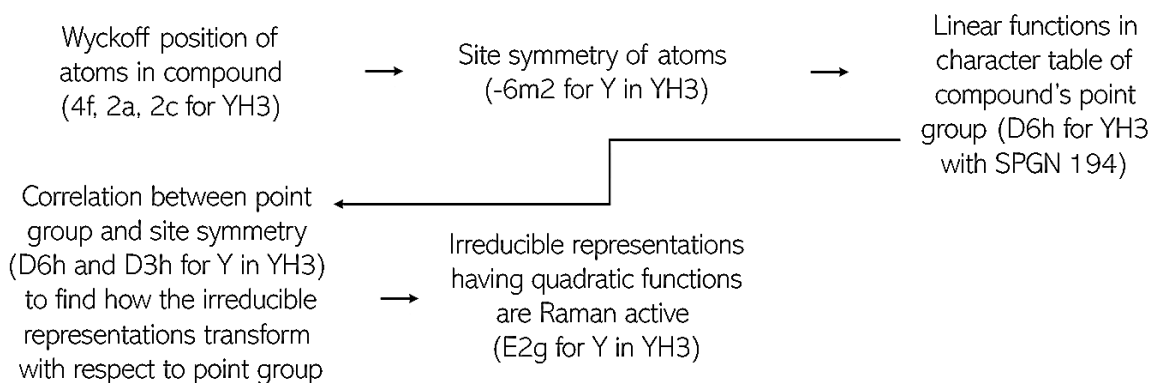


Figure 2.5: The procedure used to find Raman active modes of a compound by factor group analysis.

The process starting with atomic positions of a compound and a certain space group resulting in the determination of Raman active modes is called a factor group analysis (FGA) [35]. Such an analysis has been performed on relevant compounds for interpreting the Raman spectra of the samples of YHO. This includes FGA of YH₂, YH₃, Y₂O₃, Y, Y₂H₃O and YHO. The structure of these six compounds is shown in Fig. 4.4. The main steps of the FGA are summarized in Fig. 2.5. In the paper of Carsteanu *et al.* from 2004, the Raman spectrum of YH₂ was measured [36]. Doing a FGA for this compound one sees the relation between Raman active modes and crystal structure (section 4.1.1).

2.2.3 Instrumentation

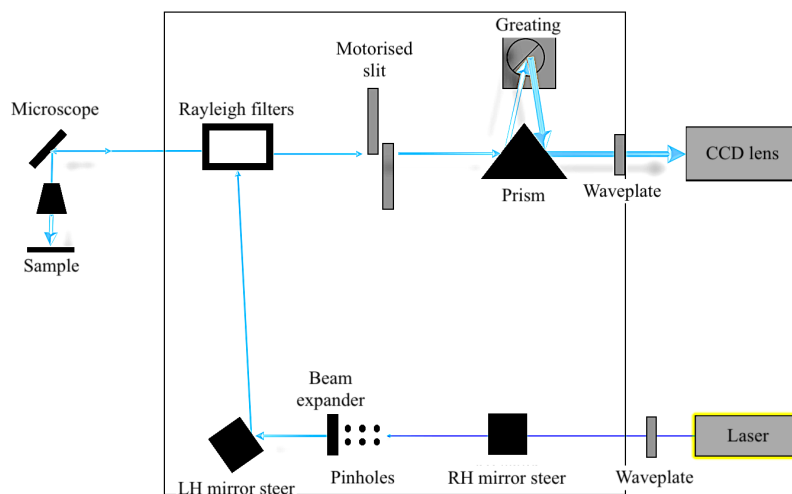


Figure 2.6: Schematic of the Renishaw inVia Raman instrument adapted from the Renishaw user manual.

A schematic setup of the Raman instrument is shown in Fig. 2.6. At the bottom of the schematic the incoming laser gets steered (by the RH and LH mirror steer and through a beam expander) in the direction of the Rayleigh filters. Except from the very small portion of Raman scattered light all light gets absorbed in the filters including the laser. A diffraction grating (top right of schematic) divides the Raman scattered light into the wavelengths of which it is composed. Finally, a CCD (Charge-coupled device) lens detects the Raman spectrum. The wavelength of the laser affect how much gets detected as an effect of the dispersion relation of Eq. 2.6. A good illustration on why shorter laser wavelength implies more spectrum detected from ref [26] is shown in Fig. 2.7.

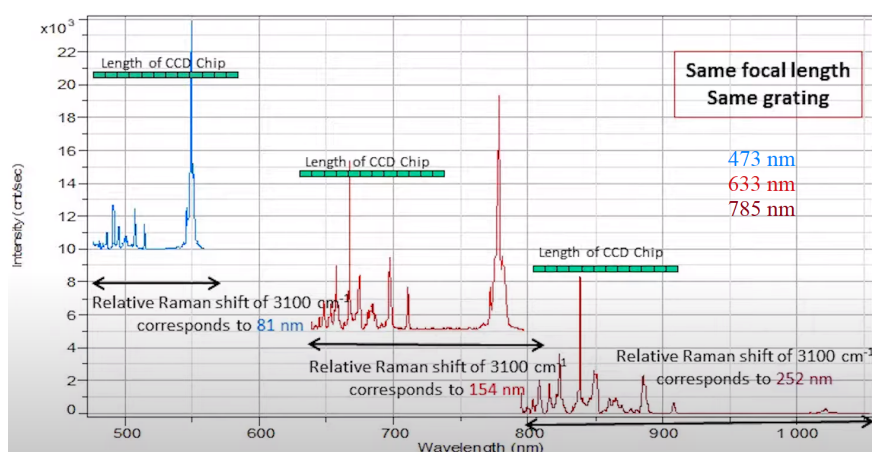


Figure 2.7: Illustration showing how the laser's wavelength affects CCD coverage due to the dispersion [26].

Table 2.2: Relevant objective and laser beam properties for the Raman measurements. WD is short for working distance. NA and laser spot sizes have been calculated by Eqs. 2.18 - 2.19 with $M^2 = 1$ and refractive index $n = 1.0003$.

Objective	WD [mm]	NA	α	Laser spot size [μm]	
				He-Ne	Diode
				632,8 nm	532,5 nm
x 5	14,0	0,12	0,120	6,433	5,414
x 20	1,15	0,40	0,411	1,930	1,624
x 50	8,20	0,50	0,523	1,544	1,299
x 100	0,33	0,85	1,016	0,908	0,764

The laser spot size varies depending on the properties of objective and laser source and is calculated using the formula

$$Laser\ spot\ size = \frac{M^2 \times 1.22 \times \lambda}{NA \times 1000} . \quad (2.18)$$

Here M^2 is the propagation ratio of the laser beam giving information about how close the laser beam is to have a perfect Gaussian distribution. For the laser spot calculations M^2 has been set to equal 1. Thus, it had no influence on the laser spot size. λ is the laser beam's wavelength in units of nm and NA is called the numerical aperture of the lens. NA determines how bright and resolved the image is for a specific objective and depends on the refractive index of the relevant medium ($n \sim 1$ for air) and the lens aperture angle α by the following equation,

$$NA = n \times \sin \alpha . \quad (2.19)$$

High NA results in short working distance (WD), small spot size and high laser power density at the sample. How this affects the measurement depends on the sample. For homogeneous transparent materials it can be advantageous to work with low NA objectives for better signal to noise ratio. Low NA corresponds to increased volume covered by the measurement. While opaque samples can be measured very well with high NA objectives since the laser will not be able to penetrate as deep into the material [26]. Some laser spot sizes are given in table 2.2.

2.3 Cyclic Optical Testing

The photochromic contrast of the YHO thin films can be determined as the difference in % transmittance between the initial and final state of a time interval t by the equation,

$$\Delta T(w, t) = T_i(w, 0) - T_f(w, t) , \quad (2.20)$$

where w is the wavenumber, T is the % transmittance and t is the time in minutes for the initial (i) and final (f) transmittance values. The value of ΔT is usually averaged over a wavenumber interval.

2.4 Four Point Probe

To examine possible hydrogenation of a metal the setup of a four-point probe can be used in order to measure the change in sheet resistance of the surface of a sample. The sheet resistance is proportional to the sheet resistivity by a factor of $\pi/\ln 2$. An increase in sheet resistivity, of e.g. a Pd coating on top of another material, can in principle indicate hydrogenation of Pd. This is an indication that H might leave the material underneath the Pd coating during a specific process (like annealing or photodarkening, for instance).

The sample measured in a four-point probe is assumed to have an infinite area with small sample thickness in comparison to s , the distance between the probe tips. Then, in the colinear setup of the four probes in which current flows between the two outer probes, the current will spread as concentric rings from the contact point between the probe tip and sample surface (Fig. 2.8). The measurement needs to be taken as close to the surface center as possible to hold on to the assumption of an infinite sample. There are factors for correction to be included in the case of this type of error.

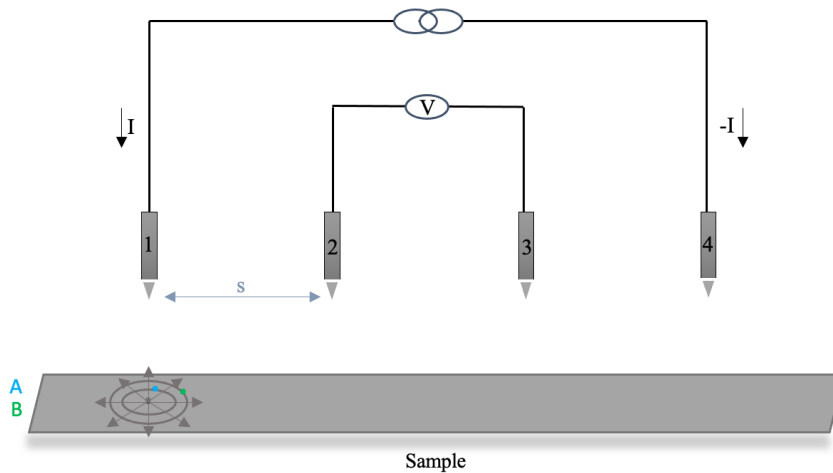


Figure 2.8: Schematic of the four-point probe configuration. All point probes are equally separated. The circular geometry of Eq. 2.21 is shown in the left hand side of the sample surface.

When current, I , crosses a ring with radius r , an infinitesimal drop in voltage can be given by

$$dV = \rho I \frac{dr}{2\pi r d}, \quad (2.21)$$

where d is the layer thickness, different from dr , the infinitesimal radial distance. By integrating both sides of Eq. 2.21 between points A and B on the surface, the change in

voltage between the two points is given by

$$\begin{aligned}\Delta V &= \int_A^B \rho I \frac{dr}{2\pi r d} \\ &= \frac{\rho I}{2\pi d} \int_A^B \frac{dr}{r} \\ &= \rho_s \frac{I}{2\pi} \ln r_B / r_A,\end{aligned}\tag{2.22}$$

where the sheet resistivity is represented by $\rho_s = \rho/d$.

The change in voltage, called the voltage drop, from tip number 2 to 3 is influenced by the current of both outer probe tips, I_1 and I_4 . Due to superposition the total voltage drop from tip number 2 to 3 becomes

$$\Delta V_{23} = \Delta V_{I_1} + \Delta V_{I_4},\tag{2.23}$$

by which the limits of integration are the concentric ring radii r_A and r_B with lengths s and $2s$ for I_1 and radii r_A and r_B with lengths $2s$ and s for I_4 , respectively. Using Eq. 2.22 we get

$$\begin{aligned}\Delta V_{23} &= \frac{\rho_s}{2\pi} \left[I_1 \ln \left(\frac{r_{B1}}{r_{A1}} \right) + I_4 \ln \left(\frac{r_{B4}}{r_{A4}} \right) \right] \\ &= \frac{\rho_s}{2\pi} \left[I_1 \ln(2) + I_4 \ln \left(\frac{1}{2} \right) \right] \\ &= \frac{\rho_s}{2\pi} [I_1 \ln(2) - I_4 \ln(2)] \\ &= \rho_s \frac{\ln 2}{2\pi} (I_1 - I_4),\end{aligned}\tag{2.24}$$

where $I_1 = I = -I_4$. Inserting these values for the currents at probe tip 1 and 4 the total voltage drop ΔV_{23} can be expressed by

$$\Delta V_{23} = \rho_s \frac{\ln 2}{\pi} I,\tag{2.25}$$

which implies the proportionality equation between the sheet resistance and sheet resistivity given by

$$\rho_s = k \frac{V}{I}.\tag{2.26}$$

From this, the proportionality constant k has the value of $\pi / \ln 2 \approx 4.53$ [37, p. 10]. This shows that by measuring the sheet resistance using a four-point probe, one can easily convert it to the often desired value of resistivity.

The point probes of the instrument, linearly aligned (Fig. 2.8), are equally spaced with a distance of $s = 1.59$ mm. The probe tips consist of a tungsten metal with finite radii

and each of the tips is supported by a spring at the other end for minimizing potential damages of the sample during probing. The four probe tips are mounted to an auto-mechanical stage which moves vertically during measurement as a reaction to crests and hills appearing at the sample surface.

To supply the outer probes (probe number 1 and 4 in Fig. 2.8) a source of current with high impedance is used. High impedance corresponds to circuits of low current and high voltage [38]. In order to determine the sample resistivity a voltmeter measures the voltage drop between the two inner probes (probe number 2 and 3). Taking the ratio of the voltage drop and the current supplied, the sheet resistance is found. As formerly described, this result has to be multiplied by a factor of correction depending on the geometry of the probe and the ratio of the probe spacing s and the film thickness d . In this case the assumption of a semi-infinite thin sheet can be made and the geometric factor takes the value of $k = \pi / \ln 2$.

2.5 X-Ray Diffraction

The physics of x-ray interaction with matter as well as structural properties of crystals are important factors for understanding the phenomenon of XRD. As for interaction of visible light with matter the properties of absorption, reflection and refraction can occur in the case of x-rays. When a high energy photon from an x-ray beam is incident on a compound the typical cases observed include Compton scattering, Thomson scattering, Auger emission and Fluorescence. These phenomena include elastic and inelastic scattering and absorption in which electrons or photons are emitted. For XRD we have the case of Thomson scattering, meaning elastic and coherent scattering from the target [39].

2.5.1 Diffraction geometry

Crystals appear as periodically arrangements of atoms or molecules. The distances within a crystal structure are of the order of a few Angstroms¹. This length coincides with the wavelength of x-rays [40, p. 2]. The fact that these two lengths coincide is crucial for the phenomenon of XRD. This is better understood from deriving Bragg's law. Based on the simplified illustration of two incident x-ray beams on a 2D crystal structure, shown in Fig. 2.9, one can perform the derivation, and better understand the geometry of diffraction. The parallel beams 1 and 2 incident on atoms 1' and 2', respectively, are incoming at angle θ . From the illustration one sees that beam 2 has to travel a longer distance than beam 1 by an integer number of wavelengths $n\lambda$ expressed by

$$AB + BC = n\lambda . \quad (2.27)$$

Using the geometry of Fig. 2.9, where $AB = BC = d \sin \theta$, Eq. 2.27 becomes

$$2d \sin \theta = n\lambda , \quad (2.28)$$

¹1 Å = 10⁻¹⁰ m

known as Bragg's law, where d is the distance between the crystal planes, n is an integer, λ is the wavelength of the incident light and θ is the angle between the incident light and the crystal plane. Hence, using the method of XRD one can, e.g., determine the inter-planar spacing within a crystal structure.

Rearranging Bragg's law one sees that in order for diffraction to occur, meaning constructive interference of scattered beams in phase, the order of magnitude of the incident wavelength and the inter-planar distances has to be the same because sine of some angle θ is always smaller than one:

$$\frac{n\lambda}{2d} = \sin \theta < 1. \quad (2.29)$$

In summary, when crystals are being irradiated by high energy photons, like in the case of x-rays having the same order of magnitude of its wavelength as of the inter-atomic spacing, diffraction may occur and a diffraction pattern is to be observed.

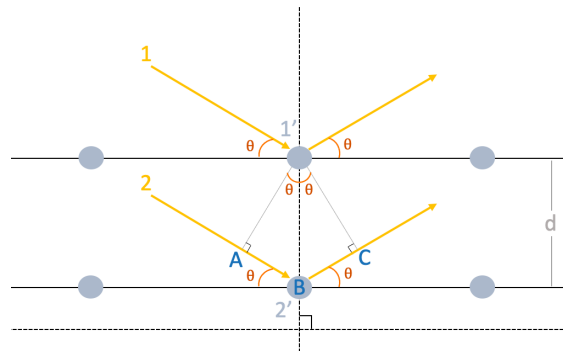


Figure 2.9: Geometry of two parallel x-ray beams, 1 and 2, incident on two crystal planes separated by a distance, d .

2.5.2 The diffraction pattern

The peaks observed in a diffraction pattern give information about the angle of which diffracted light scatter off and at what intensity. By comparing experimentally obtained patterns with theoretical patterns from international databases, one can get an indication on which reflection planes the experimental peaks represent. The calculations behind a theoretical diffraction pattern includes determination of scattering angle, structure factor, polarization factor and requires data on excitation source, lattice type/parameters, atomic positions of the unit cell and experimental geometry. The relation between Bragg's law (Eq. 2.28) and the interplanar distance d is important. Rewriting Eq. 2.28 and introducing the equation for the interplanar distances in a cubic lattice

$$d = \frac{a}{\sqrt{h^2 + k^2 + l^2}}, \quad (2.30)$$

we arrive at the formula for calculating the diffraction angle:

$$\sin^2 \theta = \frac{\lambda^2(h^2 + k^2 + l^2)}{4a^2}. \quad (2.31)$$

There is a direct relation between the particular directions of diffracted x-ray beams and the positions of atoms in the unit cell. An example on the procedure of finding a theoretical diffraction pattern for a given compound is now presented. Further, theoretical powder diffraction files (PDFs) from international databases can be used to make such analyses less time consuming.

Example

The compound of interest is YHO with space group $F\bar{4}3m$ (No. 216). The space group tells that the unit cell is a face centered cubic (fcc). For this lattice structure the miller indices (hkl) are required unmixed, i.e. all even or all odd for each set of hkl, in order for the reflection to be allowed [41, p. 79].

Table 2.3: Position of the atoms in the unit cell of fcc YHO $F\bar{4}3m$ [42].

Atom	Atomic positions			
	From cif. file	Face centering translations		
Y	1/4, 1/4, 1/4	1/4, 0, 3/4	3/4, 0, 1/4	3/4, 1/4, 3/4
H	1/2, 1/2, 1/2	1/2, 0, 0	0, 1/2, 0	0, 0, 1/2
O	0, 0, 0	1/2, 0, 1/2	1/2, 1/2, 0	0, 1/2, 1/2

The first six allowed reflection planes are represented in column 2 of Table 2.4. The index of zero is regarded even because $e^{2n\pi i} = e^0 = 1$. Column 3 represents the sum of squares of the miller indices which is used for determining the scattering angles of column 7 by Eq. 2.31. Columns 4-6 are directly related to the scattering angle 2θ . The atomic scattering factors (also called form factors) for Y, O and H atoms (in columns 9, 10, 11) are found from Table 6.1.1.1 in ref [43]. The atomic scattering factor depends on the scattering angle and excitation wavelength via the relation in column 8. The structure factor F (squared in column 12) for each of the six reflection planes is found from the equation

$$F = \sum_j^N f_j e^{2\pi i(hu_j + kv_j + lw_j)}. \quad (2.32)$$

Here N is the number of lattice points in the unit cell, f is the atomic scattering factor and u , v and w are the atomic positions. In this case $N = 4$ and the atomic positions of Table 2.3 are used. So, the structure factor is a sum of the scattered waves from the atoms of the unit cell. The values of p in column 13 are the multiplicity factors. This factor depends on the Bravais lattice (in this case fcc) and on the miller indices of the reflection plane and is found in Table 2.2 of ref [41, p. 28]. Column 14 is the Lorentz polarization factor depending solely on the scattering angle. Lorentz polarization factor is the combination

of the polarization factor and the Lorentz factor given by $1/(4 \sin^2 \theta \cos \theta)$ and $1/[2(1 + \cos^2 2\theta)]$, respectively. It depends on the geometry of the experiment, the intensity of diffraction peaks with small deviations in 2θ , and on the number of crystals oriented around 2θ .

Table 2.4: Spreadsheet for calculating the theoretical diffraction pattern of YHO (SPGN 216). The table includes explanations and notes (in blue) to the different columns.

1	2	3	4	5	6	7	8	9	10	
Line	hkl	$h^2 + k^2 + l^2$	$\sin^2 \theta$	$\sin \theta$	θ (deg)	2θ (deg)	$\frac{\sin \theta}{\lambda} (\text{\AA}^{-1})$	Atomic scattering		
								f_Y	f_O	
1	111	3	0,06	0,25	14,47	28,94	0,16	32,44	6,30	
2	200	4	0,08	0,29	16,77	33,54	0,19	31,08	5,79	
3	220	8	0,17	0,41	24,08	48,16	0,26	36,39	7,50	
4	311	11	0,23	0,48	28,58	57,17	0,31	26,11	3,96	
5	222	12	0,25	0,50	29,98	59,96	0,32	25,73	3,83	
6	400	16	0,33	0,58	35,24	70,48	0,37	24,01	3,28	
Satisfy hkl requirements for fcc			$\sin^2 \theta = \frac{(h^2+k^2+l^2) \cdot \lambda^2}{4 a^2}$				Parameter of atomic scattering factors of Col. 9-11	From Table 6.1.1.1 - International Tables of Crystallography Vol. C Col. 9-11		
11	12	13	14	15	16	17	18	19		
factor	f_H	F^2	p	Integrated intensity		Relative intensity	$\cos^2 2\theta$	$\cos \theta$		
				$\frac{1 + \cos^2 2\theta}{\sin^2 \theta \cos \theta}$	Calculated $\times 10^5$					
0,61	7458,3	8	32,06	1912610	19,13	1	0,94	0,97		
0,51	9817,6	6	24,05	1416775	14,17	0,74	0,92	0,96		
0,87	1121,7	12	12,06	162392	1,62	0,08	0,83	0,91		
0,24	5615,74	24	8,81	1187616	11,88	0,62	0,77	0,88		
0,22	263,0	8	8,09	17024	0,17	0,01	0,75	0,87		
0,16	12060,0	6	6,13	443618	4,44	0,23	0,67	0,82		
structure factor $F = \sum_j f_j e^{2\pi i(hu_j + kv_j + lw_j)}$ Determined for each set of miller indices (Col. 2)		Multiplicity factor found from tables (p. 28 - Waseda)	Lorentz polarization factor	$F^2 \cdot p \cdot \frac{1 + \cos^2 2\theta}{\sin^2 \theta \cos \theta}$		To be used in Col. 14				

The squared structure factor of column 12, the multiplicity factor of column 13 and the Lorentz polarization factor of column 14 are all contributing to the integrated intensity of the diffraction peaks. In column 15 the intensity is determined as a product of the three former columns. Column 16 contains the same data as column 15 divided by a factor of 10^5 . The relative intensity in column 16 represents all the intensities relative to the first reflection plane (111). The theoretical diffraction pattern of YHO (F43m, No. 216) with lattice parameter of 5.34 Å and X-ray excitation wavelength of 1.5046 Å is depicted in Fig. 2.10.

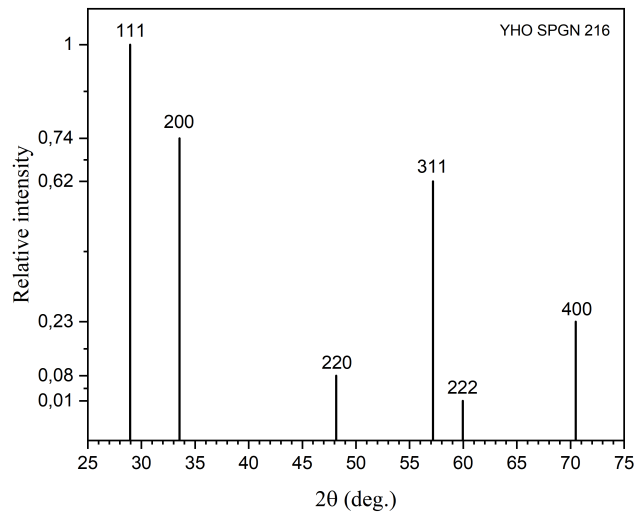


Figure 2.10: Diffraction peaks of YHO (216) obtained by theory. The intensity scale shows the relative intensities in the data set (Table 2.4)

2.5.3 Scherrer Equation

The diffraction peaks from different samples may vary in width. This can give information about the crystallite properties of the sample, provided that the contribution from instrumental broadening is accounted for. Broad peaks disclose small grain size, and sharp, thin peaks can reveal large grain size [44]. As a rule of thumb, broader peaks disclose smaller particle size with the extreme case of diffraction peaks turning into a broad "background" when the sample is amorphous. Using basic physics of constructive interference one can derive the Scherrer equation and determine the grain size. Following the same idea and main steps as of ref [44] the Scherrer equation can be derived in the following way.

Multiple reflection planes of a sample are separated from each other by a distance d . The difference in path length of different beams incident on different atoms was explained to be an integer number of wavelengths in Eq. 2.28 and will in this case be referred to as δ . The total amount of diffracted beams reaching the detector is the sum over all the

individual beams from different reflection planes:

$$\begin{aligned}
 b &= \sum_{i=1}^n b_i \\
 &= \sum_{i=1}^n A e^{ik[x+(i-1)\delta]} \\
 &= A e^{ikx} \frac{1 - e^{ink\delta}}{1 - e^{ik\delta}} \\
 &= A e^{ikx} \frac{e^{ink\delta/2}}{e^{ik\delta/2}} \left(\frac{e^{-ink\delta/2} - e^{ink\delta/2}}{e^{-ik\delta/2} - e^{ik\delta/2}} \right) \\
 &= A e^{ikx} \frac{e^{ink\delta/2}}{e^{ik\delta/2}} \frac{\sin(nk\delta/2)}{\sin(k\delta/2)},
 \end{aligned} \tag{2.33}$$

where n is the total number of beams reaching the detector. Further, the relation $n = t/d$ between separation distance d and thickness of sample t is used:

$$\begin{aligned}
 &= A e^{ikx} \frac{e^{ink\delta/2}}{e^{ik\delta/2}} \frac{\sin(tk \sin \theta)}{\sin(kd \sin \theta)} \\
 &= A e^{ikx} \frac{e^{ink\delta/2}}{e^{ik\delta/2}} \frac{\sin(tk \sin \theta)}{\sin\left(\frac{tk \sin \theta}{n}\right)}.
 \end{aligned} \tag{2.34}$$

The number of detected beams n is usually large enough ($n > 10$ [44]) for making the approximation of

$$\sin\left(\frac{tk \sin \theta}{n}\right) \approx \frac{tk \sin \theta}{n}. \tag{2.35}$$

Utilizing Eq. 2.35, we continue the algebraic part of the derivation from Eq. 2.34:

$$= n A e^{ikx} \frac{e^{ink\delta/2}}{e^{ik\delta/2}} \text{sinc } tk \sin \theta. \tag{2.36}$$

The superposition of the beams detected has an intensity proportional to the absolute square of the superposition b expressed as

$$I \propto |b|^2 = I_0 \text{sinc}^2(tk \sin \theta). \tag{2.37}$$

The width of the diffraction peak is related to the grain size calculation by the value of the peak's full width at half maximum (FWHM) which can be defined to be the width of the peak when $I = I_0/2$ is satisfied [44]. Combining this definition with Eq. 2.37 we get

$$\text{sinc}(tk \sin \theta) = \frac{1}{\sqrt{2}}. \tag{2.38}$$

If we let the angles $\theta \pm \Delta\theta$ satisfy Eq. 2.38, we can write

$$\begin{aligned}
 tk \sin(\theta + \Delta\theta) &= \text{sinc}^{-1}\left(\frac{1}{\sqrt{2}}\right) \\
 &\text{and} \\
 tk \sin(\theta - \Delta\theta) &= -\text{sinc}^{-1}\left(\frac{1}{\sqrt{2}}\right),
 \end{aligned}
 \tag{2.39}$$

and take the difference which gives

$$tk \cos \theta \sin \Delta\theta = 2\text{sinc}^{-1}\left(\frac{1}{\sqrt{2}}\right). \tag{2.40}$$

Small $\Delta\theta$ allows the approximation of $\sin \Delta\theta = \Delta\theta$ which can be defined as FWHM divided by two ($\Delta\theta = B/2$) [44]. The case of $\text{sinc}^2 x \approx \pi/2$ can be made from the condition $\text{sinc}^2 x \approx 1/2$ when x is positioned at the center of the peak's maximum ($x=\pi/2$). This gives $\text{sinc}^{-1}(1/\sqrt{2}) \approx \pi/2$. Thus, Eq. 2.40 can be expressed in an approximate form as

$$tk \cos \theta \frac{B}{2} \approx 2\text{sinc}^{-1}\left(\frac{1}{\sqrt{2}}\right) \tag{2.41}$$

$$tk \cos \theta \frac{B}{2} \approx \pi$$

$$t = \frac{\lambda}{B \cos \theta}, \tag{2.42}$$

where $k = 2\pi/\lambda$. Eq. 2.42 is the derived equation for the original Scherrer formula. It is common to multiply the right hand side by a constant factor K similar to unity (e.g. $K=0.94$ [45] or $K=0.90$ [46][47]). The general Scherrer formula can thus be written as

$$t = \frac{K\lambda}{B \cos \theta}, \tag{2.43}$$

where K is a constant close to one, λ is the wavelength of the x-ray source, B is the FWHM of the diffraction peak and θ is one half of the Bragg angle in radians.

Chapter 3

Methods

In this chapter there will be explanations with regards to the different experimental setups and procedures used for studying the YHO samples. The first section includes the method of Reactive Magnetron Sputtering for preparing the samples. This preparation was not a part of the project, but gives at least an insight.

3.1 Reactive Magnetron Sputtering

For the case of preparing the thin films of YHO, metallic yttrium (Y) was used as the target material. Ionized argon (Ar) bombarded the metallic yttrium in an atmosphere containing hydrogen (H_2). Both Y and H reacted in the plasma and got sputtered onto a glass substrate (soda lime glass) in the form of a thin film as a result. After the deposition the film was exposed to air in which oxygen (O) got incorporated into the thin film of YH_x resulting in a thin film of YHO. The technical setup for the preparation followed the same details as described in ref [13] by Montero *et al.* and the working parameters are listed in Table 3.1. The metallic yttrium used as target had a purity of 99.99 % and the argon to hydrogen gas ratio (purity 5N) in the sputter chamber was 0.125. The substrate used as support for the films was a soda lime glass, and the thickness of the prepared films ranged from ~ 500 to 1300 nm on top of the 1 mm thick glass substrate².

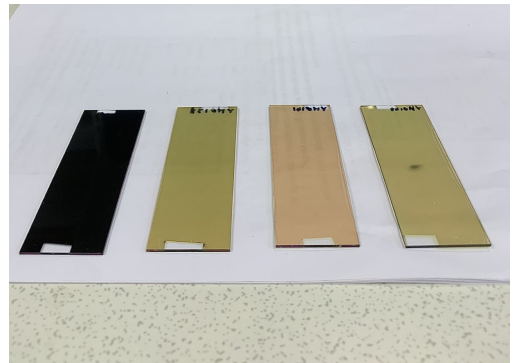


Figure 3.1: The collection of four YHO thin films prepared by reactive magnetron sputtering. The right most sample had a photodarkened spot at the moment. The deposition pressure used for each sample increases from left to right.

²1 mm = 10^6 nm

Table 3.1: Working parameters for the preparation of YHO thin films by reactive magnetron sputtering in a Leybold Optics sputter unit [13].

Parameter	Value	Note
Power density	1.33 W/cm ²	
Base pressure	$\sim 10^{-4}$ Pa	
Flux ratio	1.25 : 10	H(5N) : Ar(5N)
Deposition thickness	500-1300 nm	
Substrate dim.	75 x 26 x 1 mm ³	Soda-lime glass

A collection of four thin films were deposited at different deposition pressures (P_d), all below 1 Pa, shown in Fig. 3.1. The thin film properties are summarized in Table 3.2. They differed in thickness from 580 to 1300 ± 10 nm. Three out of four samples appeared transparent yellow (in different shades of yellow) while one of the samples appeared black and non-transparent.

Table 3.2: Properties of the thin films of YHO used for Raman spectroscopy, X-ray diffraction and cyclic optical testing.

Sample	P_d (Pa)	H ₂ /Ar-ratio	Thickness (nm)	Color
138	0.63	0.125	750 \pm 10	Yellow
141	0.72	0.125	580 \pm 10	Yellow
148	0.82	0.125	1300 \pm 10	Yellow
155	0.53	0.125	780 \pm 10	Black

3.2 Setup and Procedure

In between preparation and the different measurements the collection of YHO thin films was stored in a MBraun glove box to protect them from air. The glove box at UiS was filled with Ar. It had an average amount of H₂O less than 0.5 ppm and contained less than 8 ppm of O₂ [48]. The glove box at IFE was filled with nitrogen (N) and an average containment of H₂O and O₂ less than 0.1 ppm and 0.1 ppm, respectively.

3.2.1 Raman Spectroscopy

For the Raman measurements a Renishaw inVia Raman microscope equipped with two laser sources and a Leica DM2700 M microscope with four different objectives (x5, x20, x50, x100) was used. The two laser sources available were the 633 nm He-Ne laser and the 532 nm diode laser. Working parameters of the Raman microscope, like acquisition time, laser power and magnification lens, varied in order to obtain best possible spectra for the different measurements. All measurements were made with the door shut and with the lamp in the instrument switched off. The lamp was switched on for short

periods only (when searching for focus of the sample and when taking pictures in the microscopic view) in case it would induce a photodarkening of the sample and affect the measurements.

We optimised the measurement conditions by comparing spectra obtained with different working parameters. This included a variety of different laser powers, two different laser wavelengths, changes in acquisition times and switching between different objective lenses.

Measurements of the glass support before and after illumination with UV was done in order to see how it was affected by illumination. In that case it could have had an impact on the Raman spectra of YHO before and after UV.

Literature study on earlier measurements of similar compounds was done in the process of interpreting the obtained Raman spectra of YHO. In order to assign the peaks we had to compare with other spectra of other compounds because of very few previously reported measurements on YHO, in fact only one [16]. Raman spectra of YH_2 , YH_3 and Y_2O_3 and their assignments were considered.

FGA for different phases of YHO, yttrium hydrides and yttrium oxides was also made in order to understand the vibrational symmetries of the compounds and to determine which of the vibrational modes were Raman active and expected in spectra.

3.2.2 Cyclic Optical Testing

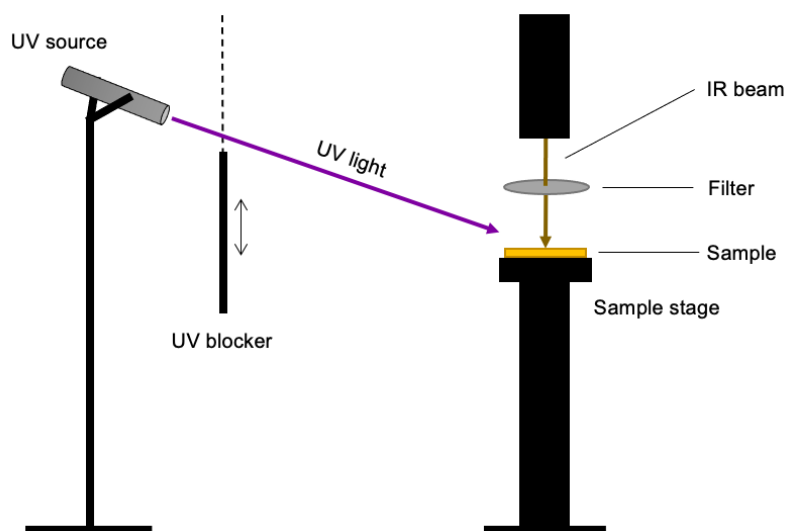


Figure 3.2: Simplified overview of the cyclic optical measurement setup.

For each of the samples of YHO (Table 3.2) an infrared (IR) transmittance spectrum was measured as a reference. The four spectra were measured by the usage of a Bruker IFS 125HR Fourier transform spectrometer. The spectrometer was equipped with a light

source of quartz (SiO_2), an InSb detector and a CaF_2 beam splitter in order to filter out radiation that could induce photodarkening of the films.

Then, a cyclic optical testing was performed with the same instrument. We did cycles of 30 minutes UV-illumination followed by 30 minutes bleaching for a total of 2 cycles for each sample (2 hours total). In the first part of the cycle a collimated UV laser diode was used (section 3.2.3). For the next part of the cycle, where the films bleached, a nontransparent black sheet was placed in the trajectory of the UV-light source which stopped the UV-light from reaching the film. During the 2 hours of cyclic testing of each film the % transmittance got measured approximately every 0.8 second and averaged between 700 and 900 cm^{-1} . The averaged range was determined from the response in the reference IR transmittance spectra. The measurement setup for the cyclic experiment is illustrated in Fig. 3.2.

3.2.3 UV-Illumination

For illumination of the YHO samples different light sources were used. In the case of Raman spectroscopy before and after UV-illumination a collimated UV laser diode (Thorlabs GmbH) with wavelength of 402.9 nm and an output power of 4.6 mW was used. With this source the four samples of Table 3.2 were illuminated for at least 30 minutes and at most 1 hour in air. The setup is illustrated in Fig. 3.3, where it is shown that the UV-light was perpendicularly incident to the film surface.

The same UV laser diode was used for irradiating the YHO samples inside the glove-box in an Ar atmosphere for 2-3 hours before Raman measurements. The UV-light was, also in this setup, incident to the sample surface at a right angle.

For the cyclic optical testing a collimated UV laser diode (Thorlabs CPS405) with wavelength of 405 nm and an output power of $(4.5 \pm 0.5) \text{ mW}$ was used.

In the case of the electrical measurements of Pd coated samples before and after UV-illumination a Wavelabs SINUS-220 solar simulator was used. The samples were light soaked by LED-lamps simulating the radiation of 1 sun. Both AM 1.5 G light soaking and UV-channels light soaking programs were used to photodarken the Pd coated YHO films.

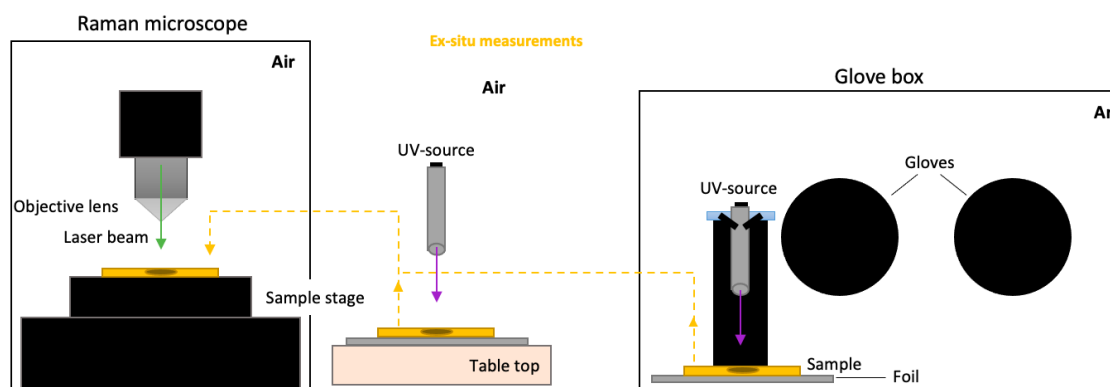


Figure 3.3: Setup for the UV illumination of YHO thin films in air and in glove box of before Raman measurements.

3.2.4 Four Point Probe

The Keithley 197 Autoranging Microvolt DMM in a direct current (DC) mode measuring sheet resistance in units of Ω was used. The samples for investigation had different thicknesses in Pd coating ranging from 5 to 50 nm (Table 3.3). Prior to the Pd coating the YHO samples had been deposited by reactive magnetron sputtering on glass at a deposition pressure of 1 Pa with Ar and H₂ flow of 160 and 20 sccm, respectively. The YHO thin films had all a thickness of ~ 2400 nm measured by a stylus based profilometer (Alpha-step 200).

Six samples of Pd coated YHO thin films, depicted in Fig. 3.4, were measured with the four-point probe before and after UV-illumination in a solar simulator (section 3.2.3). The samples were placed under the four point probe with the Pd side up. They were measured as close to the surface centre as possible for a set of 10 measurements, removing and replacing the sample each time. When illuminating the samples after the initial four-point probe measurement they were placed with the glass side up (Pd pointing downwards) inside the solar simulator. Immediately after illumination the samples were placed with the Pd pointed upwards for the probing. Each measurement was made 10 times for a final arithmetic average to reduce the random uncertainties. The mean standard deviation was calculated for random uncertainty within the 10 data points of measured sheet resistance.

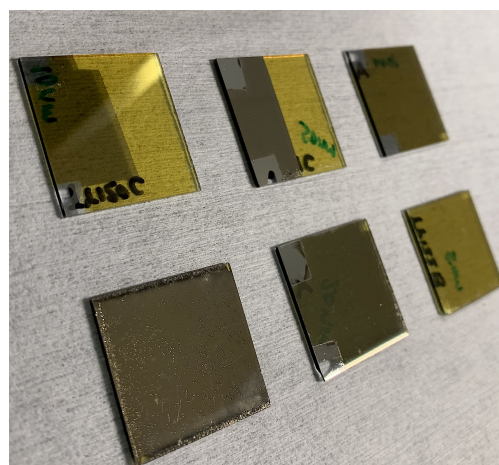


Figure 3.4: Picture of six Pd coated thin films of YHO used for electrical measurements with the four-point probe.

The electrical measurements were made once more for the same samples after 3 weeks

stored in a glove-box (N atmosphere). This time the samples were light soaked in the same solar simulator for continuously 1 hour with UV-channels. The two days of electrical measurements of Pd/YHO/glass combined with UV-illumination are denoted A and B and were performed 1 month apart. All the measured data can be found in Appendix D.

Table 3.3: An overview of the six Pd/YHO/glass samples measured with the four-point probe before and after UV-illumination and the chosen properties of illumination in the solar simulator for each sample.

Sample	Pd (nm)	Illumination A	Illumination B
TY121B	50	1 h AM 1.5 G + 10 min UV channels	1 h UV channels
TY121C	50	1 h AM 1.5 G + 15 min UV channels	1 h UV channels
TY120A	20	1 h AM 1.5 G	1 h UV channels
TY120C	10	1 h AM 1.5 G + 20 min UV channels	1 h UV channels
TY121A	10	1 h AM 1.5 G + 30 min UV channels	1 h UV channels
TY122B	5	1 h AM 1.5 G	1 h UV channels

3.2.5 XRD

For the XRD measurements of YHO a D2 PHASER X-ray diffractometer from Bruker with Cu K-alpha radiation source (0.15406 nm) was used. The instrument was equipped with a LynxEye XE-T detector which filters out most of the Cu K-beta radiation. The zero point offset of the angular scale less than 0.01° , made the uncertainty in step size between data points negligible. Both the sample stage and detector were rotating ($\theta - 2\theta$ configuration) during the measurement as shown in the simple illustration of Fig. 3.5, sometimes referred to as a Bragg-Brentano geometry.

The films of YHO were placed in four different holders and attached using gum on the glass side. Then the holders were placed at four of the six positions of the sample stage. During the measurement the Bragg angle 2θ went from 1 to 100 degrees in one hour for each of the four samples.

For the analysis of the obtained XRD spectra Origin software (Pro 2019 version) was used for Gaussian peak fitting and FWHM determination needed for grain size calculations. The average grain size for each of the samples was estimated by the Scherrer equation (Eq. 2.42) with the Scherrer constant K of 0.9. This constant value has commonly been used in relevant literature [46], [47]. When using the Scherrer equation, the particles were assumed to have spherical shape.

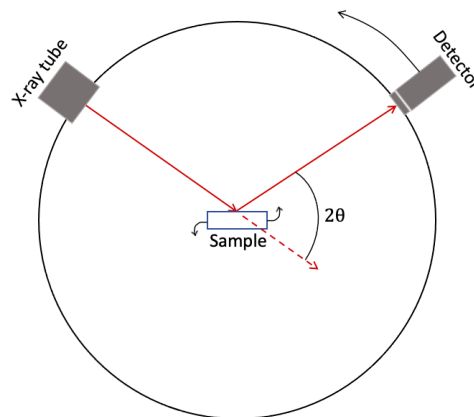


Figure 3.5: Geometry of the XRD setup.

In order to assign the reflection planes present the measured patterns were compared to powder diffraction files (PDFs) of similar compounds (Y_2O_3 , YH_2 and $YH_{2\pm\delta}$) from the International Centre for Diffraction Data (ICDD). The reason for only comparing the obtained diffractograms of YHO with similar compounds was the overall lack of references on YHO in ICDD.

Chapter 4

Results and Discussion

In this chapter the results from the different experimental methods are presented. First the results from the Raman study and the associated experiments will be introduced. This accounts for the main part of the thesis. Then the resulting spectra of the cyclic optical testing will be presented. This shows the photochromic response of the YHO samples. Then, the results from electrical measurements of Pd coated samples are given, and finally, the XRD patterns obtained for YHO are shown with comparison to different references.

In case of the sputtering, the non-transparent sample was deposited at 0.53 Pa. Thus, it seems like the critical limit for the deposition pressure of transparent films is below 0.63 Pa. The colors of the thin films are related to the band gap energy of the sample [7]. This energy relates to the oxygen content of the sample which is dependent on the P_d of the sputtering process. Higher pressure results in higher oxygen content in the thin film after oxidation. The oxygen content has been shown to be negatively linked to the hydrogen content in the film [7], [14], [49], [50]. Thus, the band gap increases with increasing P_d along with the O/Y ratio [51].

4.1 Raman Measurements

The results of the Raman measurements include FGA of two different YHO stoichiometries and different yttrium hydrides and yttrium oxides as well as peak assignments after literature study of similar compounds. A large part of the experimental work with the Raman microscope involved optimization of the measurement conditions. Thus, results of different working parameters and the best fitted parameters found are included here. The spectra obtained for the photodarkened state compared with the clear state are presented, in addition to the glass substrates' effect on the measurements.

4.1.1 FGA and Literature Study

Table 4.1: Data for input to the FGA retrieved from ref [52]. WP is short for Wyckoff position and the right most column (Sym.) shows the site symmetries of the atomic positions.

Compound	Space group	Point group	WP	Sym.
YH ₂	Fm $\bar{3}$ m (225)	O _h ⁵	8c, 4a	O _h , T _d
YH ₃	P6 ₃ /mmc (194)	D _{6h} ⁴	4f, 2c, 2a	C _{3v} , D _{3h} , D _{3d}
Y ₂ O ₃	Im $\bar{3}$ (206)	T _h ⁴	48e, 24d, 8a	C ₁ , C ₂ , S ₆
Y	P6 ₃ /mmc (194)	D _{6h} ⁴	2c	D _{3h}
Y ₂ H ₃ O	Pn $\bar{3}$ m (224)	O _h ⁴	6d, 4b, 2a	D _{2d} , D _{3d} , T _d
YHO	F $\bar{4}$ 3m (216)	T _d ²	4c, 4b, 4a	T _d

YH₂ has space group number (SPGN) 225 expressed in Hermann-Mauguin notation as Fm $\bar{3}$ m [36]. This corresponds to the point group O_h⁵ in Schönflies notation. The space group tells us that YH₂ has a face-centered cubic Bravais lattice (F), two mirror planes (m) and a six fold rotation-reflection axis ($\bar{3} = S_6$). In YH₂ the yttrium atom is positioned at the origin while the hydrogen atoms are positioned at coordinates (1/4, 1/4, 1/4) and (3/4, 3/4, 3/4) with site symmetries O_h (m $\bar{3}$ m) and T_d (43m) [53]. From the character tables of O_h and T_d [27, pp. 365–366] the yttrium and hydrogen atoms have translational modes F_{1u} and F₂ which according to the correlation table between O_h and T_d [27, p. 405] transform as F_{1u} and F_{2g}. From the character table of the point group O_h⁵ only the F_{2g} mode is Raman active. F_{2g} represents a three dimensional (triply degenerate) irreducible representation (F), anti-symmetric with respect to principal axis rotation (2) and symmetric with regards to inversion (g). This single Raman active mode agrees with the single peak appearing in the spectrum of YH₂ shown in Fig. 4.3. This peak, centered at $\sim 1142 \text{ cm}^{-1}$, is due to tetrahedral sites of hydrogen and is thought to be broad due to interaction between hydrogen atoms [36].

When more hydrogen is added to the highly symmetric YH₂ the symmetry reduces and more modes appear [36]. This can be observed from the spectra of YH_{2+ δ} and YH₃ in Fig. 4.3. The factor group analysis for YH₃ of SPGN 194 (P6₃/mmc) was carried out in the same way as for the YH₂ and is summarized in Table 4.2. It has non-degenerate (A_{1g}) and doubly degenerate (E_{1g}, E_{2g}) active modes, all symmetric to inversion through the center (g). Since the FGA of YH₃ with space group P6₃/mmc gave four Raman active modes, shown in Table 4.2, while the experimental spectrum of Fig. 4.3 shows 9, it suggests that YH₃ has another structure. Carsteanu *et al.* proposed the space group I4/mmm for an intermediate state YH_{2+ δ} [36].

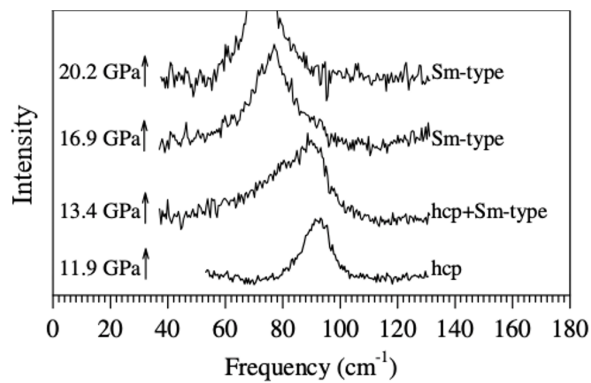


Figure 4.1: The lowermost spectrum for metallic Y in hcp phase shows one broad peak at approximately 90 cm^{-1} . Modified to not include all the measured spectra [54].

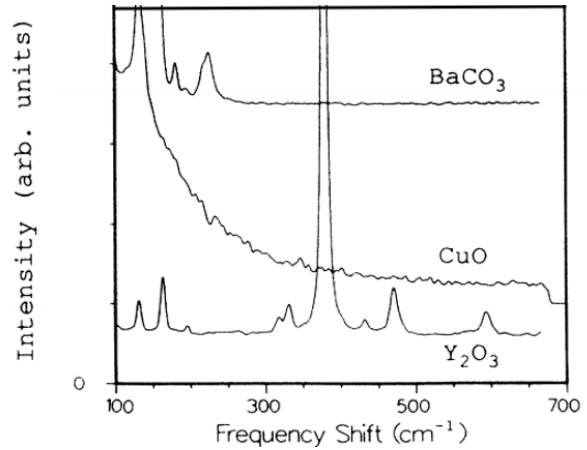


Figure 4.2: Raman spectrum of Y_2O_3 shows 9 peaks in the range $100 - 700 \text{ cm}^{-1}$. Modified to include less of the measured spectra of other compounds [55].

Y_2O_3 with SPGN 206 ($\text{Im}\bar{3}$) is expected to have 22 Raman-active vibrational modes when studied with Raman spectroscopy according to the FGA with 16 units of Y_2O_3 per unit cell and a total of $3N = 3 \cdot 16 \cdot 5 = 240$ normal vibrations. The total vibrational modes were determined as

$$O_{vib} + Y_{vib} = (3A_g + 3E_g + 9F_g) + (A_g + E_g + 5F_g). \quad (4.1)$$

The Raman spectrum of Y_2O_3 for a truncated range is shown in Fig.4.2.

Metallic yttrium has hexagonal close packed (hcp) structure and SPGN 194 ($P6_3/mmc$) which corresponds to the point group D_{6h} . The atomic coordinates of the Y atoms are $(\frac{1}{3}, \frac{2}{3}, \frac{1}{4})$ with site symmetry D_{3h} ($\bar{6}m2$). According to the character table for the site symmetry the translational modes (T_x, T_y, T_z) for Y are E' and A_2'' [27, p. 362]. According to the correlation table between D_{6h} and D_{3h} the symmetry species for the translational modes transform to E_{2g}, E_{1u}, B_{2g} and A_{2u} of which only the first mode is Raman active [27, p. 401]. This agrees with the experimental Raman spectra obtained by Olijnyk with 647 nm Kr^+ laser containing only one peak (Fig. 4.1) [54]. E_{2g} represents a two dimensional irreducible representation, anti-symmetric with respect to principal axis rotation and symmetric to inversion. The Raman microscope at hand during this project had a cutoff in the frequency range at about 100 cm^{-1} . Hence, potential formations of metallic domains could not be observed for our YHO samples.

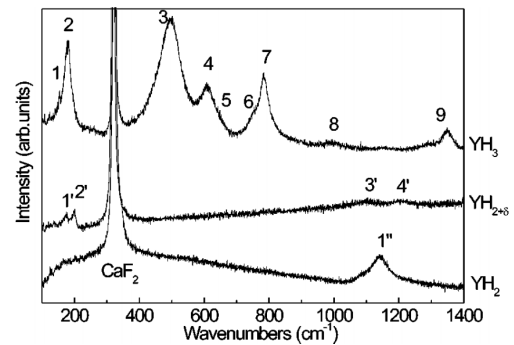


Figure 4.3: Raman spectra of three phases of yttrium hydride [36].

For the case of YHO the stoichiometry preferred from the energy point of view is YH_xO_y with $x=y=1$ and space group $F\bar{4}3m$ (SPGN 216) [8][42]. This space group corresponds to the point group T_d which denotes full tetrahedral symmetry for the atoms of hydrogen and oxygen. For this phase of YHO there is one Raman active mode, F_2 , determined by FGA. This result agrees with Supplementary Table 28 of Supporting Information of ref [42] and with Raman active modes from Bilbao Crystallographic Server [56]. F_2 denotes a three dimensional representation (triply degenerate) anti-symmetric with respect to the improper rotation S_4 . S_4 consists of a rotation by 90° about the C_4 axis followed by a reflection across the plane perpendicular to the C_4 axis.

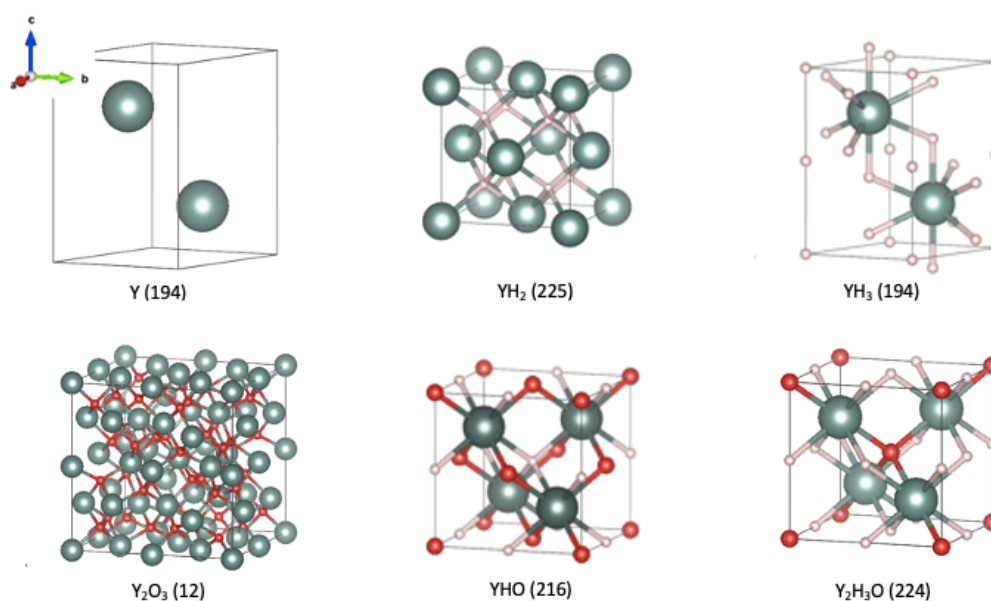


Figure 4.4: Unit cell structure of six different compounds relevant for the interpretation of the yttrium oxyhydride samples. The illustrations have been made using VESTA Software [57] with input data from ref [42], [53], [58]–[60]

Another stoichiometry of the YHO has also been studied to find the number of expected peaks of our samples. FGA was done for $\text{Y}_2\text{H}_3\text{O}$ with space group $Pn\bar{3}m$ (SPGN 224) and point group O_h . The Y, H and O atoms are positioned at Wyckoff positions (WP) 4b, 2a and 6d, respectively. Two $\text{Y}_2\text{H}_3\text{O}$ molecules occupy a single unit cell. Thus, there are 12 atoms per unit cell giving $3N = 3 \cdot 12 = 36$ normal vibrations. Following the procedure of Fig. 2.5 the total vibrational modes of this yttrium oxyhydride were found:

$$O_{vib} + Y_{vib} + H_{vib} = 3F_{2g} + 5F_{1u} + E_u + 2F_{2u} + A_{2u} + F_{1g}. \quad (4.2)$$

This coincides with the $3N$ modes due to the singly, doubly and triply degeneracy of A, E and F, respectively. According to the character table of O_h only F_{2g} is Raman active [27, p. 366]. This means three peaks are expected in Raman measurements of $\text{Y}_2\text{H}_3\text{O}$, but none of them related to any of the Y atoms. Therefore, one could conclude that our samples of YHO were not solely of this stoichiometry because peaks due to Y vibrations did occur in

experiment as discussed in section 4.1.3. However, this phase could have been present in the samples as a mixture with another phase with Raman active Y-vibrations.

Table 4.2: Output data from FGA. Raman active vibrational modes determined for the atoms of different compounds.

Compound	Raman active modes		
	H	O	Y
YH ₂	F _{2g}		
YH ₃	A _{1g} + E _{1g} + E _{2g}		E _{2g}
Y ₂ O ₃	3A _g + 3E _g + 9F _g		A _g + E _g + 5F _g
Y	E _{2g}		
Y ₂ H ₃ O	2F _{2g}	F _{2g}	
YHO	F ₂	F ₂	F ₂

4.1.2 Optimisation of measurement conditions

The aim was to obtain the best spectrum with best signal-to-noise ratio, least effect of the laser on the sample and least contribution from the glass support. For this, we varied laser wavelength, objective lens and measurement time. In the earliest attempts of measuring one of the thin films (No. 138) the lamp inside the chamber used to focus the laser beam was switched on. This left visible dark spots on the film (Fig. 4.5) which restored when the film was not exposed to the lamp. For this reason, the rest of the measurements were made with the lamp inside the chamber switched off in case this photo-darkening would influence the results.



Figure 4.5: Visible dark spots on film No. 138 due to the lamp in the the Raman instrument.

For the Raman measurements objective lenses with magnification $\times 50$ and $\times 100$ with working distances (WD) of 8.20 and 0.33 mm, respectively gave the best results together with the 532 nm laser. The relation between laser wavelength, WD and objective is given in Table 2.2. With these magnifications the spectra contained less background signal from the glass substrate. Comparing Figures 4.6 and 4.7, one observes that the Raman spectrum of YHO made with low magnification ($\times 20$) objective lens had more signal from glass than the one with high magnification ($\times 100$) objective lens. According to ref [26], the use of an objective lens with small magnification (low NA) would often be an advantage in Raman experiments including transparent, homogeneous samples. In the optimisation process for our Raman experiments this was shown not to be the case. Hence, when performing Raman measurements for samples which easily get damaged from the laser source the hypothesis of working with low NA objectives for good quality spectra may not be fulfilled.

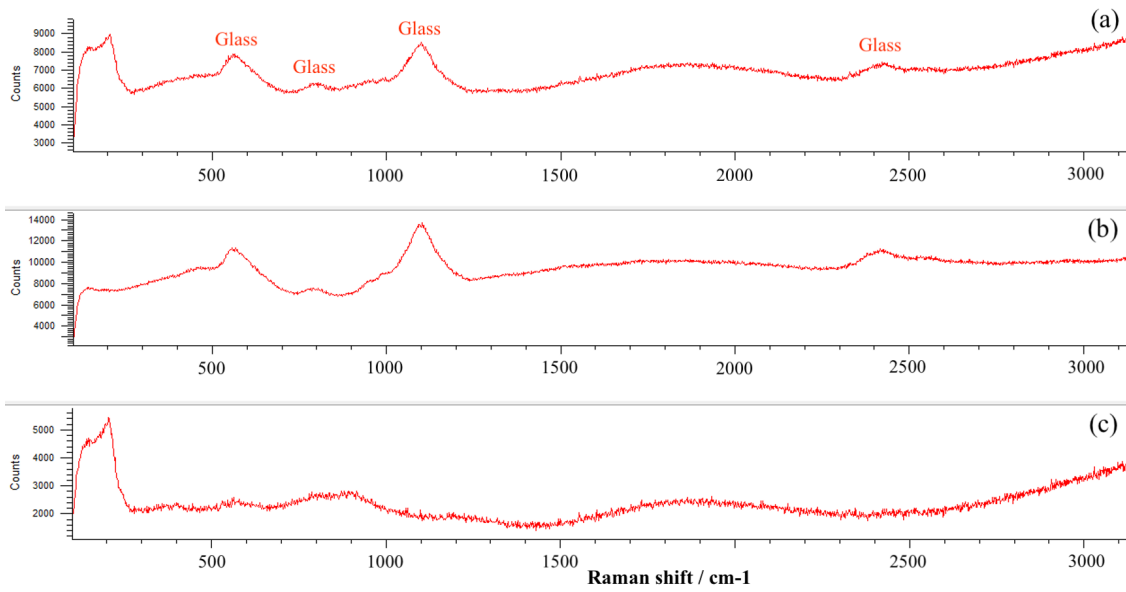


Figure 4.6: Data arithmetic of the measured spectra of YHO No. 148 with objective x20 and spectra of glass made with 532 nm laser. The three panels include measured spectrum of YHO (a), measured spectrum of glass (b) and the resulting spectrum after subtracting glass from sample spectrum (c).

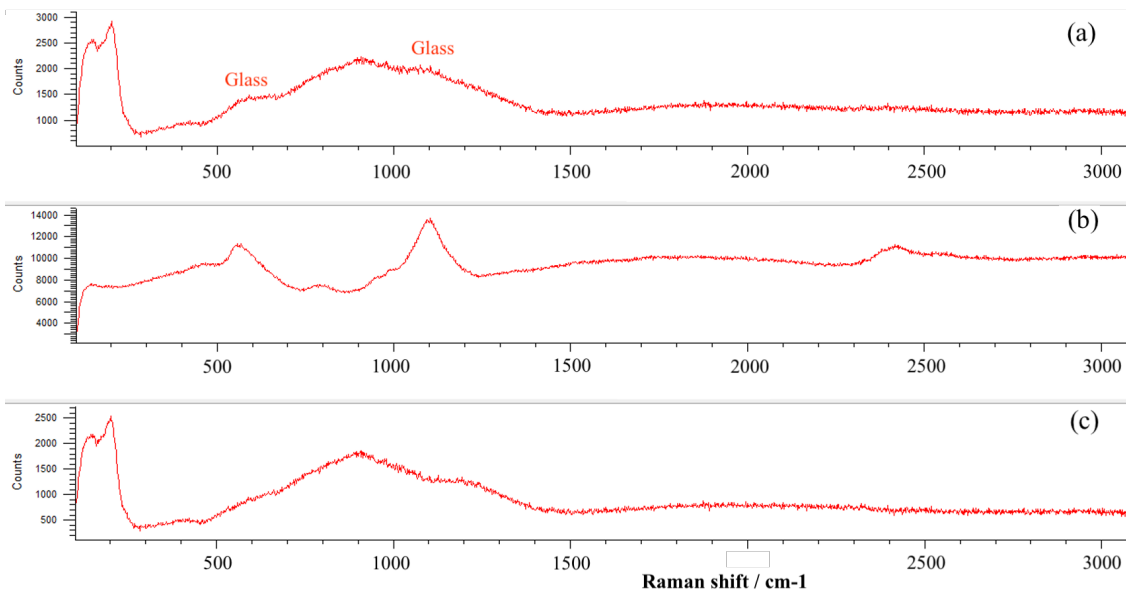


Figure 4.7: Data arithmetic of the measured Raman spectra of YHO No. 141 with objective x100 and spectra of glass made with 532 nm laser. The three panels include measured spectrum of YHO (a), measured spectrum of glass (b) and the resulting spectrum after subtracting glass from sample spectrum (c).

Of the two available lasers, with wavelengths of 532 and 633 nm, there were challenges with both. The 532 nm laser easily damaged the thin films of YHO and caused fluorescence of the resulting compound(s). This was evident from dark spots left on the sample on the microscopic scale after measurements with the laser. In order to show that the dark spots observed in the microscope were caused by sample damage and not a photodarkening effect, Raman measurements were performed at the position of the dark spots. These measurements were made with low laser power of the 633 nm laser which was found to not leave dark spots on the sample. The spectra showed neither sample peaks nor peaks from the glass substrate for the the largest spots (from 50 and 100 % laser powers) as shown in Fig. 4.9. The fact that we did not observe the peaks from glass may evidence that the destroyed sample was yttrium metal which is expected to have one single Raman active mode outside of the measurement range (centered at 88 cm^{-1} [61]). The same spots were observed the next day (after 22 hours) as well. Thus, the conclusion of the film being damaged by sufficient powers of the 532 nm laser could be made. An overview of how the different laser powers of the 532 nm laser caused sample damage is shown in Fig. 4.8. The concentric ring structure for the most damaged cases is thought to be due to laser ablation influenced by monochromatic optical aberration of the lens [62]. In Appendix A (Fig. A3), Raman of different parts of the ring structure of the most damaged spot is presented which supports the cause of laser ablation. Thus, in order to perform Raman measurements without damaging the samples the 633 nm laser was thought to be preferred. Unfortunately, the 633 nm laser introduced new difficulties. The spectrum of glass showed fluorescence with the red laser. This is clear from the intensity scale when comparing with the Raman measurements of glass with green laser in Fig. 4.14 in section 4.1.4. In Fig. 4.10 one sees the strong Raman intensity of glass compared to the Raman intensity of YHO when using the 633 nm excitation source. This comparison evidences how weak the Raman scattering is with regards to fluorescence. Thus, the glass substrate contributed a strong background to the Raman spectra of the samples and hid potential Raman signals from the sample.

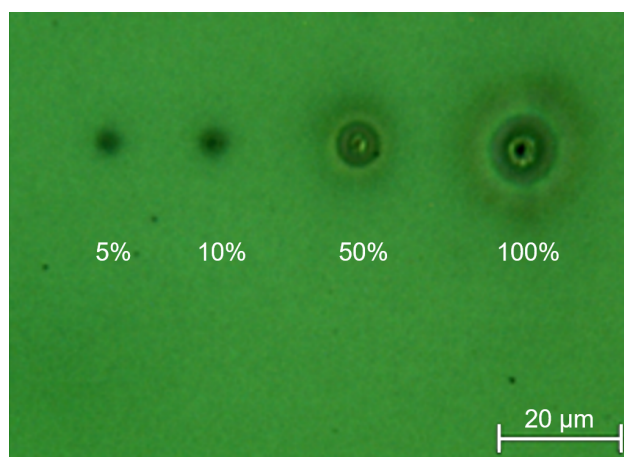


Figure 4.8: Damaged spots on thin film after Raman measurements with different percentage powers of 532 nm laser.

High laser powers like 50-100 % usually gives the highest intensity of peaks with little background noise, but in this case it damaged the samples and caused fluorescence. This was solved by reducing the laser powers to 1-10 % together with increasing the acquisition time from seconds to minutes. The fluorescence and background from the glass support made the choice of 532 nm laser and large magnification objective lens most efficient. The spectra of Fig. 4.11 were obtained with x100 magnification, 1 % of maximum power of 532 nm laser for 300 seconds acquisition time. The maximum laser power for 532 nm laser was 50 mW resulting at 0.5 mW (at most) for 1%.

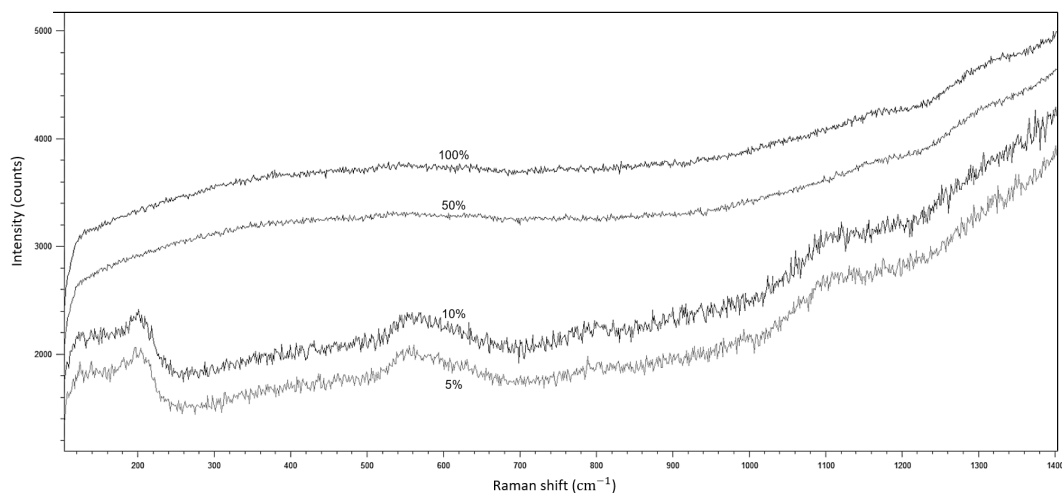


Figure 4.9: Raman measurements of YHO No. 138 made with 633 nm laser at damaged spots. The spectra for the most damaged spots (50 and 100 %) show no sample peaks. The less damaged spots (5 and 10 %) show better response of the sample in the low Raman shift region ($< 200 \text{ cm}^{-1}$).

The fluorescence of glass with 633 nm laser detected in Raman experiment (section 4.1.4) compares well with the literature of ref [27, p. 98],[30],[31]. Changing to the 532 nm laser the background from glass was reduced. According to this, the usage of shorter wavelength lasers for Raman measurements of the YHO thin films should be investigated while keeping in mind that the thin films of YHO easily burn. Measurements with shorter wavelength laser should, in that case, be performed with low percentage laser power. An UV-laser with wavelength of 325 nm would theoretically give 14 times better efficiency for the Raman measurements than the 633 nm laser. With 325 nm laser one would also obtain Raman peaks with shorter absolute wave lengths and completely eliminate the effect of fluorescence which was shown to overlap with the Raman effect for the 633 nm laser. Except for the increased energy per photon most likely to induce damage, it would possibly induce photodarkening of the films as well. Therefore, measurements of a YHO film in its complete clear state before photo darkening may be difficult and may challenge a complete comparison between Raman effect before UV and after UV. The solution points towards sputtering thin films on different support. One could also propose the usage of lasers in the IR region for Raman measurements. Raman with IR lasers of YHO have not

been reported previously and could be a good way to eliminate photodarkening when seeking clear state spectra.

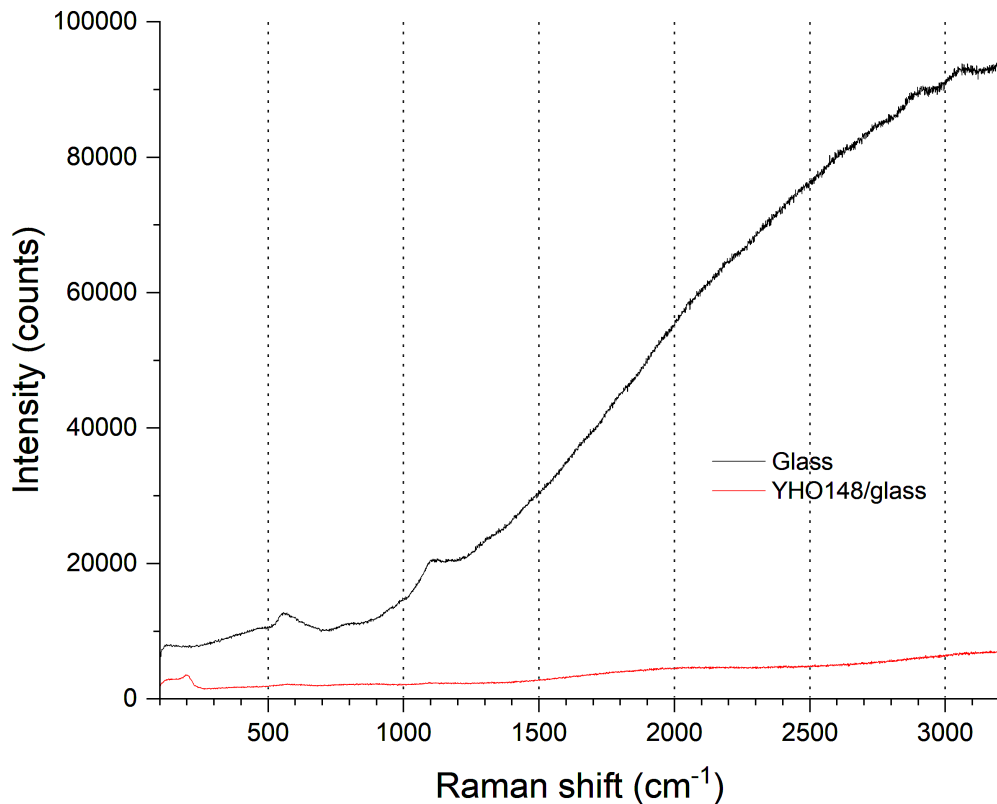


Figure 4.10: Raman spectra of glass and YHO film compared when measured with 633 nm laser with the same y-scale.

Due to the strong background from glass in the high Raman shift region, the samples should, for further research, be deposited onto other substrates when studied with Raman spectroscopy. One suggestion is to deposit the thin films on top of fused quartz substrates. Fused quartz has been observed to scatter strongly only below 500 cm^{-1} without any PL [31]. For investigation of YHO in the low wave shift region a suggestion is to deposit the thin film onto CaF_2 substrate. The Raman spectrum of CaF_2 shows a single peak at 321 cm^{-1} and minimal fluorescence [63]. This would make it easier to distinguish the sample peaks from a potential background from the substrate with lower frequency lasers to not damage the thin films.

4.1.3 Raman spectra of films before illumination

An overview of the Raman peaks of YHO and their assignments compared to previous papers and Raman spectrum of glass is presented in Table 4.3. From the table one sees that the peak positions lower than or equal to 200 cm^{-1} are all due to Y vibrations. The bands due to Y vibrations in YH_3 and Y_2O_3 have different vibrational symmetries of E_g

and F_g+A_g , respectively. In the obtained spectra for YHO films, we observe 3 modes in the low wave shift instead of the one triply degenerate mode predicted for YHO $F\bar{4}3m$ by FGA. This signifies a symmetry lower than for YHO $F\bar{4}3m$. Upon the symmetry lowering the triply degenerate mode can split. Two subgroups of O_h that provide such splitting are D_2 and C_{2v} which give the 222 and mm2 in the Hermann-Mauguin notation, respectively and point to orthorhombic crystal lattice. In such case, the other two F_2 modes related to H and O are also expected to split into 3 modes each. This corresponds well with our experimental spectra of YHO with only one suggested peak related to O and with the 4 peaks related to H if at least one out of those are due to glass.

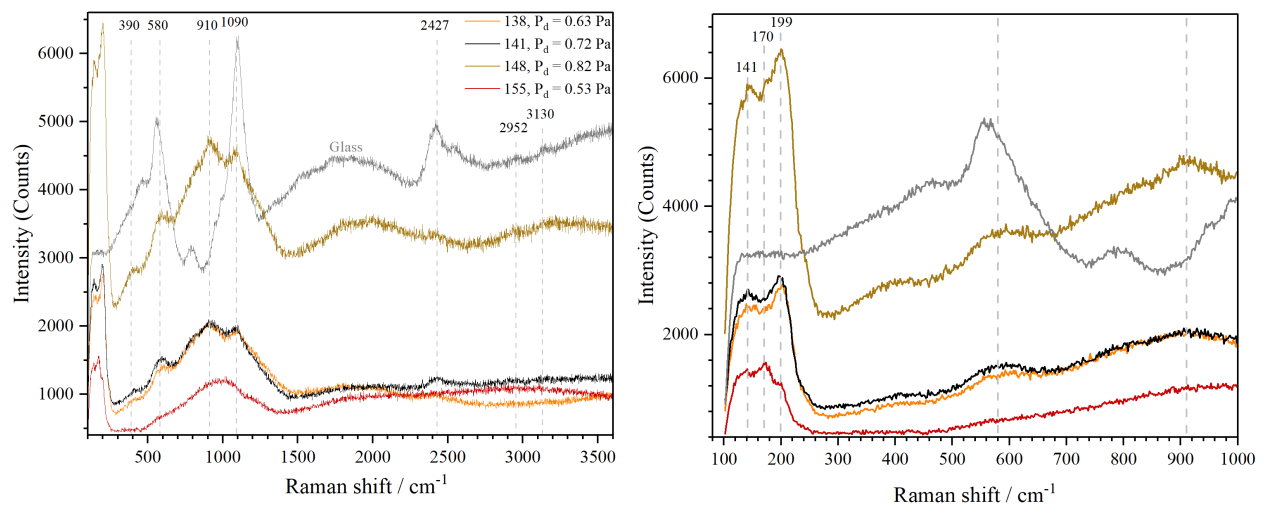


Figure 4.11: Raman spectra of four thin films of YHO deposited at different pressures and glass (grey). The measurements were made with 532 nm laser for long acquisition time (300 s) and large magnification ($\times 100$) before any radiation with UV light. The labels show manually added peak positions. The low wave shift region has been magnified and labeled in the right hand side panel. Glass spectrum has been re-scaled in y to fit the diagram.

The peak at 141 cm^{-1} could, however, be assigned to glass. To examine this, we measured a sample with different magnification of the objective. In this case, the larger amount of glass with respect to that of film was measured for smaller magnification ($\times 20$) due to deeper laser penetration into the sample. The result is shown in Fig. 4.12, and it is evident that in the case of $\times 20$ objective the glass contribution significantly increases for all peaks but those at low shifts. Thus, we can conclude that the peak at 141 cm^{-1} is due to the sample. Further, since vibrational modes of H atoms at octahedral sites appear for wavenumber shifts between 362 and 798 cm^{-1} and vibrational modes of H atoms positioned at tetrahedral sites appear for intermediate shifts [36], we suggest that the Raman band centered at 580 cm^{-1} may be due to H at octahedral sites and that the peaks positioned at approximate 910 and 1090 cm^{-1} are due to tetrahedral H. Nevertheless, there is a possibility that the 580 and 1090 cm^{-1} peaks are due to the glass substrate as can be seen by their corresponding peak positions in Fig. 4.11 and by the fact that the peak

at 580 cm^{-1} decreases in intensity when the laser penetrates deeper (Fig. 4.12). Further, it is possible that the thin films are composed of several phases, one of them being F43m and another unknown phase.

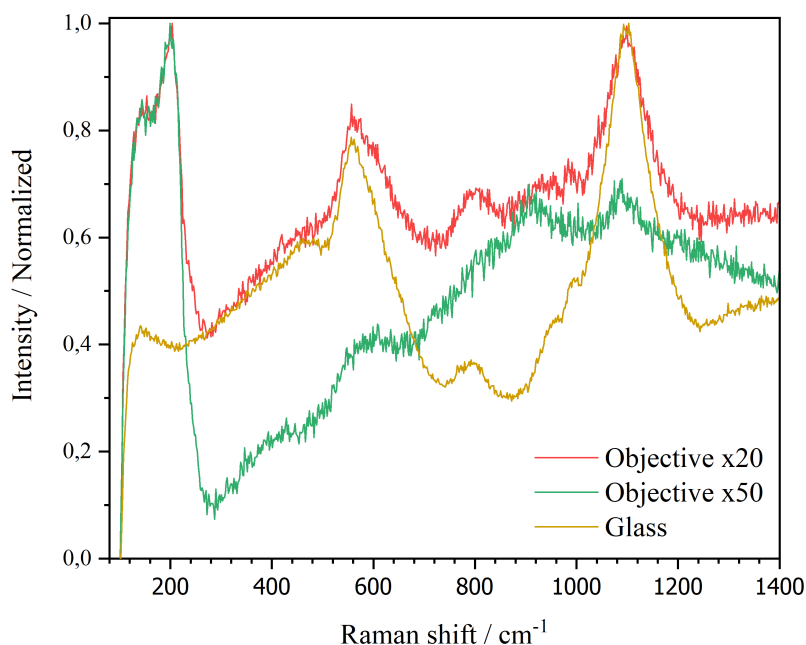


Figure 4.12: Comparison of Raman spectra of film No. 148 with different objectives with spectrum from glass.

It is known that the region above 3200 cm^{-1} can reveal OH^- anions. However, since the band appearing at 3130 cm^{-1} in the measured spectrum was very weak it was not concluded that the sample contain OH^- anions. Also, the peak positions of 3130 and 2952 cm^{-1} seem to match the peaks from glass. The suggestion of Y-O bond about 390 cm^{-1} was motivated by the general Raman band table of ref [64] assigning metal-O bonds to the region $150\text{-}450\text{ cm}^{-1}$. The spectra of YHO films with corresponding peak labels to Table 4.3 are shown in Fig. 4.11.

The most striking difference between the four Raman spectra is the measured intensity for film No. 148 in the high wave shift region compared to the other three spectra. Film No. 148 is the thickest of the four films and it was deposited at the highest pressure. Another difference is the peaks positioned around 3000 cm^{-1} for sample No. 148 which are not as clearly present for the other samples. The other three spectra are more similar to each other in intensity, but still not the same. The lowest measured intensity was obtained for sample No. 155 which is the only opaque film deposited at the lowest pressure. A prominent difference between film No. 155 and the other three is the low intensity spectrum as well as the three peaks present in the low region to the contrasting two peaks present at the same position for the other. Also, the broad peaks at about 400 and 600 cm^{-1} seem to be missing for film No. 155.

Table 4.3: Table of Raman peak positions of different, but similar compounds from literature, and suggestions on the interpretation of our spectra of YHO.

Compound	YH3			YH2	Y2O3		YHO
Atom	Kume <i>et al.</i>	Racu <i>et al.</i>	Carsteanu <i>et al.</i>		Bhadra <i>et al.</i>	Jinqiu <i>et al.</i>	Our suggestions
Y	150 (Y) 170 (Y) 190 (Y)	155 (Y) 180 (Y)	153 (Y, Eg) 180 (Y, A1)		130 (Y) 170 (Y)	130 (Y, Fg) 162 (Y, Fg+Ag)	141 - Y 170 - Y 200 - Y
O						593 (Y-O, Fg+Ag)	390 - Y-O
H	580 (HO) 780 (HT) 1100 (HT)	760 (H) 790 (H) 1300 (H)	501-783 (HO) 997 (HT) 1287 (HT)	1142 (HT)			580 - HO or glass 910 - HT 1090 - HT or glass 2427 - glass 2952 - glass 3130 - OH- or glass

Notes: HO - Hydrogen at octahedral site, HT - Hydrogen at tetrahedral site, YHO peak positions were not the same for all samples, peak positions in units of cm⁻¹

Overall, one observes the presence of peaks due to yttrium vibrations in the low wave shift region ($<200 \text{ cm}^{-1}$) in all four spectra. There are no clear shifts in peak positions, but there are differences in measured intensity between the different films. The intensity of the spectra does not correlate perfectly with the deposition pressure nor the film thickness because the spectra of film No. 138 and 141 cross each other at approximately 1500 cm^{-1} and the intensity of film No. 155 exceeds the intensity of film No. 138 in the region $2000\text{-}3500 \text{ cm}^{-1}$. Finally, one observes that the spectrum of film No. 148 is markedly more noisy compared to the other three, although it was measured with the same working parameters.

The positions of the experimentally obtained peaks in this work were compared to the experimental spectra of transparent and opaque films of YHO in ref [16]. They used a higher frequency laser ($\lambda = 325 \text{ nm}$) for the measurements and did not report possible sample damage. The peak centered at approximately 400 cm^{-1} may refer to the peak present at 374 cm^{-1} in their spectrum. Two of the peaks present in our spectra centered at 580 and 1090 cm^{-1} compare very well to their peaks at 590 and 1096 cm^{-1} , respectively. Especially, because of the agreement that the peaks are present in the case of the transparent films but missing for the opaque film. Beyond that, the Raman spectra of YHO obtained with the 532 and 325 nm lasers do not match. The potential presence of pure Y vibrations was out of scale in ref [16] and could therefore not be compared. This applied for the peaks present in the high wave shift region as well, since the maximum measured shift were set to 1700 cm^{-1} in ref [16]. For one of the transparent YHO films (No. 141) we compared the spectra measured at three different spots to investigate the sample homogeneity. The comparison showed some effect on the spectra due to slight variation of laser focus for different spots. The comparison is shown presented in Fig. 4.13.

For better interpretation of the measured spectra of YHO one could try changing hydrogen (H_2) with deuterium (D_2) (H-D isotope exchange) in the deposition. This could make the assignment of vibrations that include H easier. An exchange with D_2 should cause a linear shift towards lower Raman shifts by $\sqrt{2}$ for all H-included vibrational modes. Such isotope exchange studies for YH_2 are reported in ref [36].

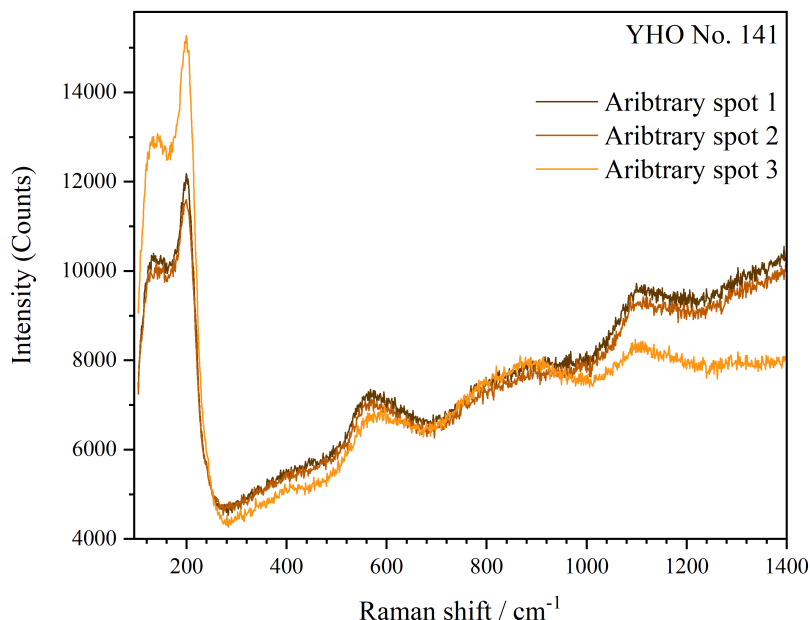


Figure 4.13: Raman measurements with laser focus at three different arbitrary points on film No. 141.

4.1.4 Effect from UV on glass

Spectra of glass with 532 and 633 nm lasers before and after illumination with UV are shown in Fig. 4.14. The obtained spectra did not show changes in the peak positions when comparing before/after illumination. The intensity of the obtained spectrum for glass with green (532 nm) laser shows an overall increase after irradiated for 30 minutes with UV-light. The peak at position 1097 cm^{-1} increases by ~ 4600 counts (33.33 %). The increase in intensity can be due to movement of the sample between measurements as well. The intensity of the obtained spectrum for glass with red (633 nm) laser shows a decrease in the first part of the wave shift range before it shows an increase from $\sim 1700\text{ cm}^{-1}$. The largest decrease between these spectra is observed to about 3800 counts (34.86 %) and the largest increase to ~ 6100 counts (11.73 %). We observe that the signal appears much stronger for glass with 633 nm laser than 532 nm laser. This does not follow from the intensity equation in section 2.2.1, and is believed to be solely due to the fluorescent effect. According to the intensity dependency, the 532 nm laser should theoretically give two times higher counts than the 633 nm laser. Hence, comparing the Raman spectra of glass for the two lasers mentioned we observed that glass is fluorescent with the red laser.

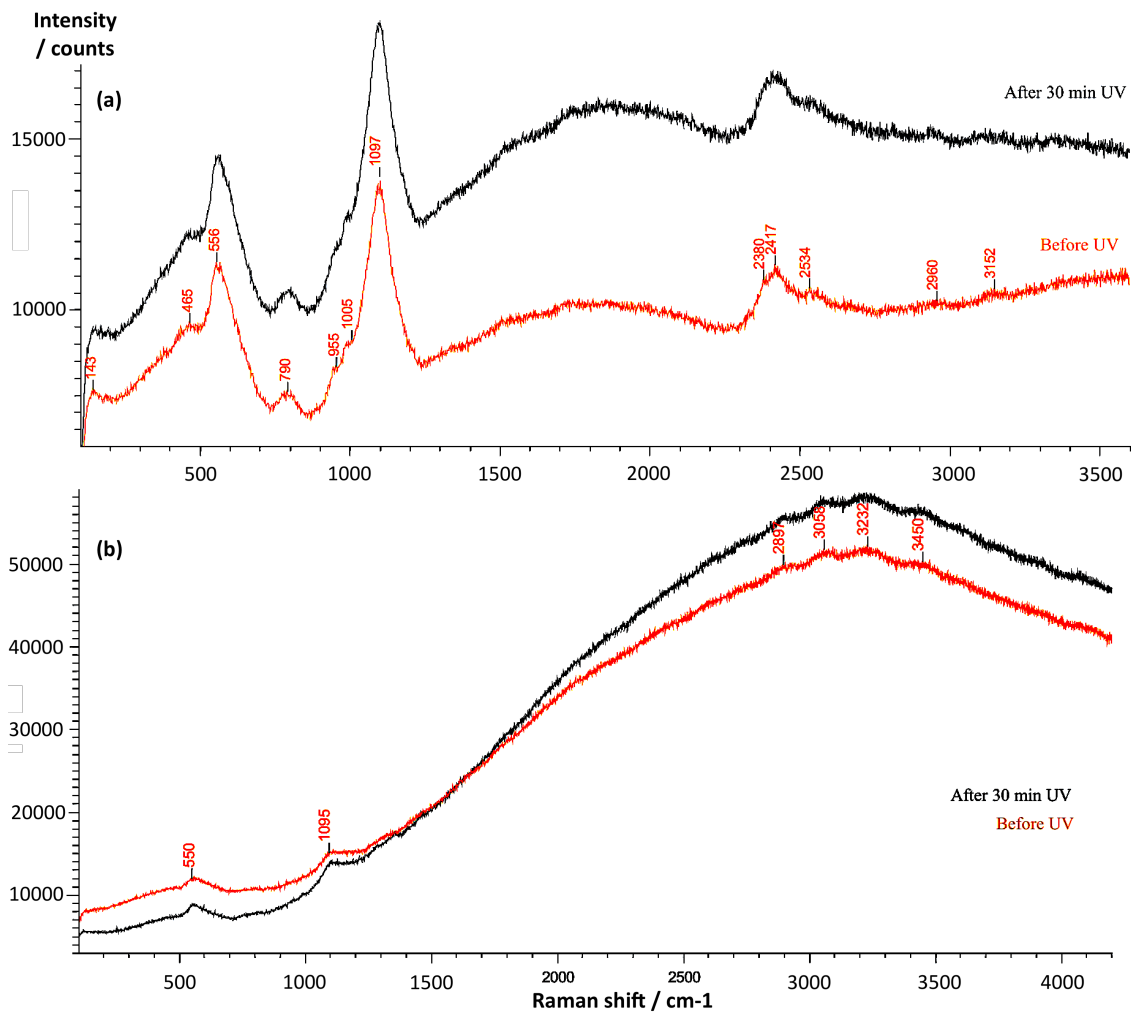


Figure 4.14: Raman spectra of glass before and after 30 minutes UV illumination measured with 532 nm laser (a) and 633 nm laser (b).

4.1.5 Raman of UV-illuminated samples

As reference the four thin films of YHO were measured in the Raman microscope before UV-illumination as shown previously in Fig. 4.11.

Illuminated in air

Raman measurement of sample No. 138 after 30 minutes UV-illumination showed both similar and decreased intensity in different parts of the Raman shift range. The spectra are presented in Fig. 4.15a. For the low wavenumber region the intensity before and after UV was similar, while for wavenumbers larger than 1500 cm^{-1} the intensity decreased by a minimum of 22 % after illumination by UV. This may be due different measurement spots. None of the Raman peaks shifted, nor vanished. Only the peak centered at 2412

cm^{-1} is close to vanish in the photodarkened state.

The comparison of the obtained Raman spectra of sample No. 141 before and after photodarkening is shown in Fig. 4.15b. For this film the comparison showed a consistent decrease in measured intensity after photodarkening. It was not observed any clear shifts in peak positions, but the peak centered at 2427 cm^{-1} was more present in the photodarkened state in this case compared to the similar peak present for the former film.

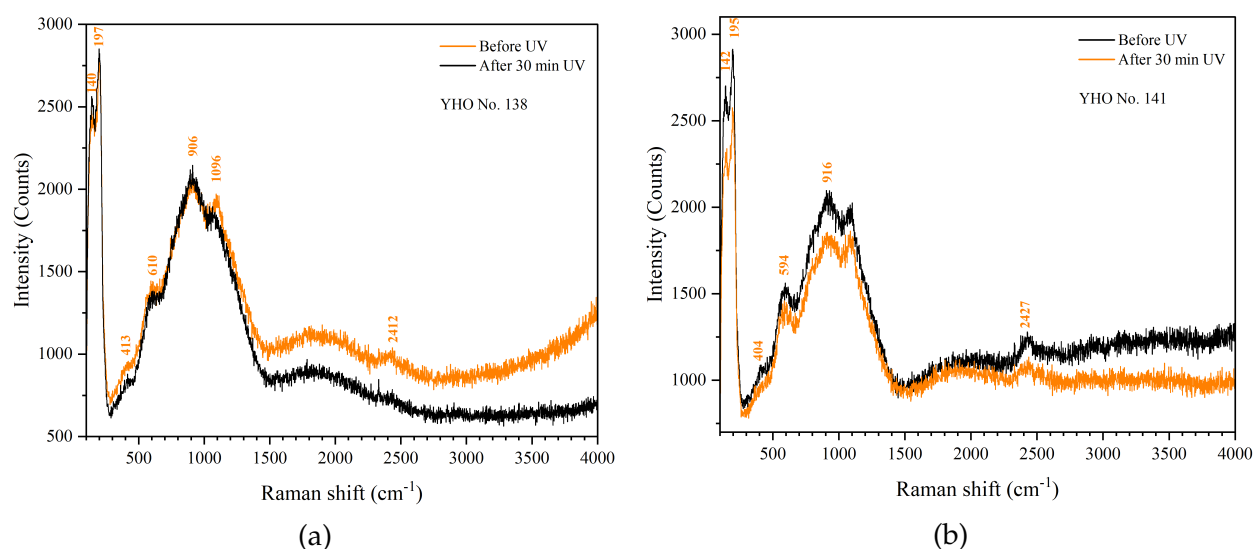


Figure 4.15: Raman of clear (coloured spectrum) and photodarkened state (black spectrum) of YHO film No. 138 and 141 after 30 minutes UV-illumination in air.

For the thickest film, No. 148, the comparison of the Raman spectrum of clear and photodarkened (in air) state is shown in Fig. 4.16. Due to the film thickness (1300 nm) it was expected the least contribution from glass compared to the other films. These Raman measurements were performed some weeks later than the others. One of the most striking differences with regards to film No. 138 and 141, is the broad peaks obtained in the high wave shift region ($>1500 \text{ cm}^{-1}$) for the clear state. This background was obtained when measuring the clear film before UV, more than once. Since the broad peaks are more or less not present for the photodarkened state, they could be described as a background effect from glass. However, this type of background was not obtained in any other measurement. Thus, we can not assign the broad peaks to the effect from glass. The other significant difference from the former transparent films is the presence of possibly three peaks between 900 and 1200 cm^{-1} rather than two. The third peak centered at approximately 1197 cm^{-1} appears more like a shoulder for the photodarkened state. In principle, this could point towards a less symmetric phase for this film. Beyond that, it is worth to mention the relatively low signal to noise ratio. This makes the peak positions approximate, and there could be a masking of other potential peaks as well.

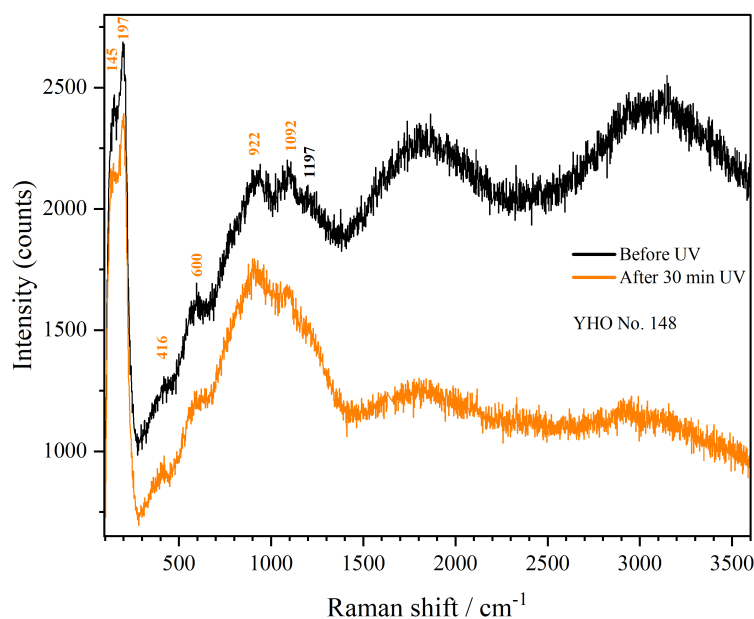


Figure 4.16: Raman of clear (coloured spectrum) and photodarkened state (black spectrum) of YHO sample No. 148 after 30 minutes UV-illumination in an air.

Illuminated in an inert atmosphere

The three initially transparent YHO samples (No. 138, 141 and 148), illuminated for 2-3 hours inside a glove box with argon atmosphere, showed changes in Raman with regards to the measured intensities. For sample No. 138 (Fig. 4.17a) the photodarkened state consistently measured lower counts for the Raman peaks, and the peak positioned at $\sim 1066 \text{ cm}^{-1}$ vanished for the photodarkened state. For these measurements the peak centered about 2400 cm^{-1} was not present in the case of either clear nor photodarkened state.

For sample No. 141 the measured intensity in the low Raman shift region ($< 200 \text{ cm}^{-1}$) was approximately the same for the photodarkened and clear state. Moving towards higher wavenumbers, the intensity from the photodarkened state decreased with respect to the clear state spectrum. The spectrum of sample No. 141 before and after UV illumination in the inert atmosphere is shown in Fig. 4.17b. Also for this sample, the peak centered about 1100 cm^{-1} (1104 cm^{-1}) nearly vanished in the case of photodarkening. The peak centered at 2427 cm^{-1} vanished as well from its broad and weak presence detected in the clear state.

In the case of sample No. 148, with obtained spectra shown in Fig. 4.18, the trend somehow differed from the two former samples. In the high Raman shift region ($< 1500 \text{ cm}^{-1}$) the measured intensity of the photodarkened state decreased by a much larger amount. Around 2000 cm^{-1} the measured counts decreased by $\sim 127 \%$. Observation of peaks present in the $\sim 3000 \text{ cm}^{-1}$ region were also made. From clear to photodarkened state the two peaks centered approximately at 2952 and 3130 cm^{-1} appear as one single peak

centered at 2910 cm^{-1} . As mentioned for film No. 138 and 141, it was observed a change between the clear and photodarkened state about 1100 cm^{-1} for this film as well.

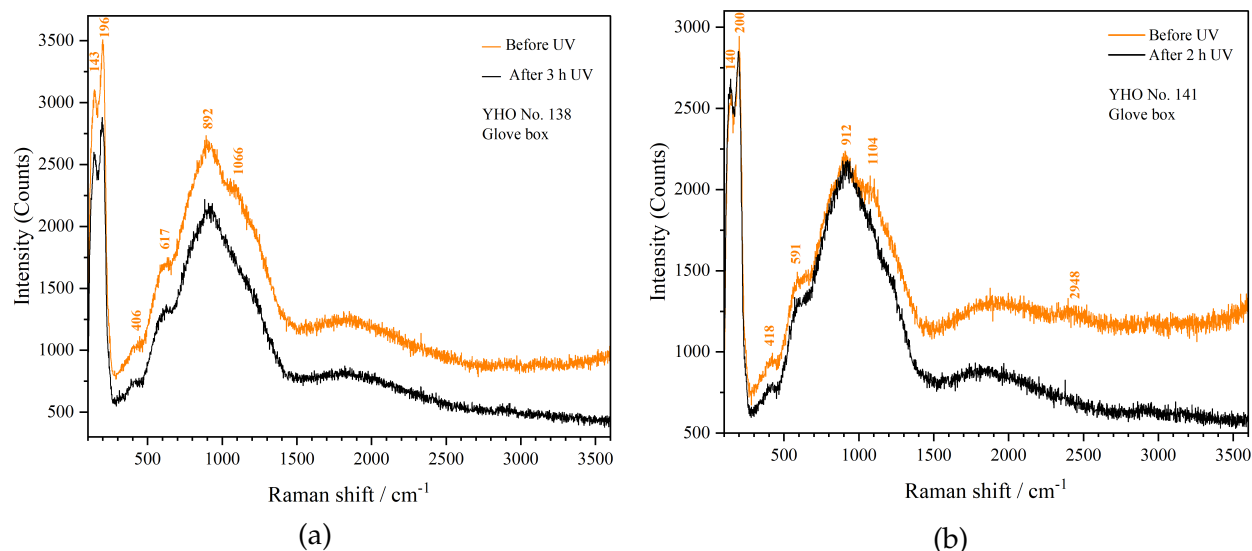


Figure 4.17: Raman of clear (coloured spectrum) and photodarkened state (black spectrum) of YHO film No. 138 and 141 after 2-3 hours UV-illumination in an argon atmosphere.

When comparing the photodarkened states induced by UV-illumination in two different atmospheres (air and Ar) for samples No. 138, 141 and 148 it was observed changes between the Raman spectra for different media of illumination. In all cases, the peak positioned about 1100 cm^{-1} vanished in the case of photodarkening when illuminated inside the glove box (Ar atmosphere) as well as in air. A possibility for the peak vanishing is the effect from glass, because when the films are photodarkened, less glass is measured than for the transparent state. The results from section 4.1.4 imply that the observed decrease in Raman intensity after UV-illumination in general, is a consequence of the photodarkening, because the UV-illuminated glass measured higher intensities in the relevant regions. The Raman spectra of films 138 and 141 before UV, after UV in air and after UV in Ar are combined in Figures A4 and A5 in Appendix A for overview.

It is important to stress the difference in time duration of the UV-illumination between the process in air and in the inert gas atmosphere. This could be a factor for the spectrum changes. The reason for the short illumination time in air was the air sensitivity of the samples. Thus, it cannot be concluded that the change is solely due to illumination in the Ar atmosphere. One should perform the measurements with the same illumination time in each medium to be more certain about the origin of the changes.

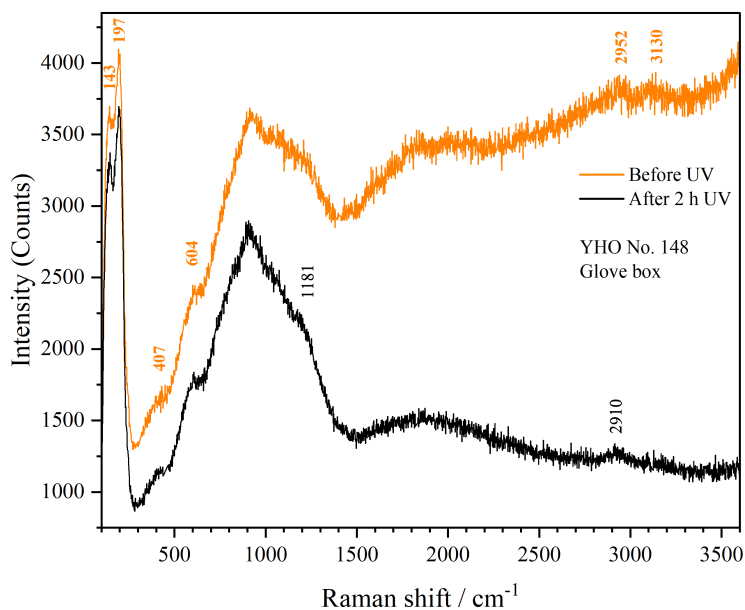


Figure 4.18: Raman measurement of clear (coloured spectrum) and photodarkened state (black spectrum) of YHO sample No. 148 after 2 hours UV-illumination in an argon atmosphere.

4.2 Cyclic Optical testing

As a reference the infrared transmittance was measured before UV illumination of the samples. These transmittance spectra are shown in Fig. 4.19 with % transmittance plotted against wavenumber w (cm⁻¹). The average transmittance of the YHO thin films between 700 and 900 cm⁻¹ were approximately 80 % for all of the samples except for sample No. 155 (Fig. 4.19d) which initially had an opaque appearance.

The cyclic measurement over 2 hours of sample No. 148 is shown in Fig. 4.20a where % transmittance is plotted as a function of time. Immediately before the first photodarkening ($t=0$) the film transmitted $\approx 80\%$ of the IR light source. During the first 30 minutes of UV illumination the % transmittance decreased to $\approx 41\%$ giving a photochromic performance of $\Delta T \approx 39\%$. When the UV-light was blocked for the next 30 minutes of the cycle the sample restored some of its transparency (%T ≈ 64). It is evident that it takes more time for the sample to bleach back to initial transparency from the photodarkened state than for it to obtain the same amount of photochromic contrast. One also sees that as the sample was illuminated for the second time the % transmittance decreased to lower values. The total photochromic performance of sample No. 148 during the 2 cycles was determined to approximately $\Delta T = 45\%$.

The cyclic testing of sample No. 141 (Fig. 4.20b) shows similar performance starting from 79 % transmittance. During the first 30 minutes of UV illumination the % transmittance reduced to ≈ 47 before the UV source was blocked and the sample restored some of its

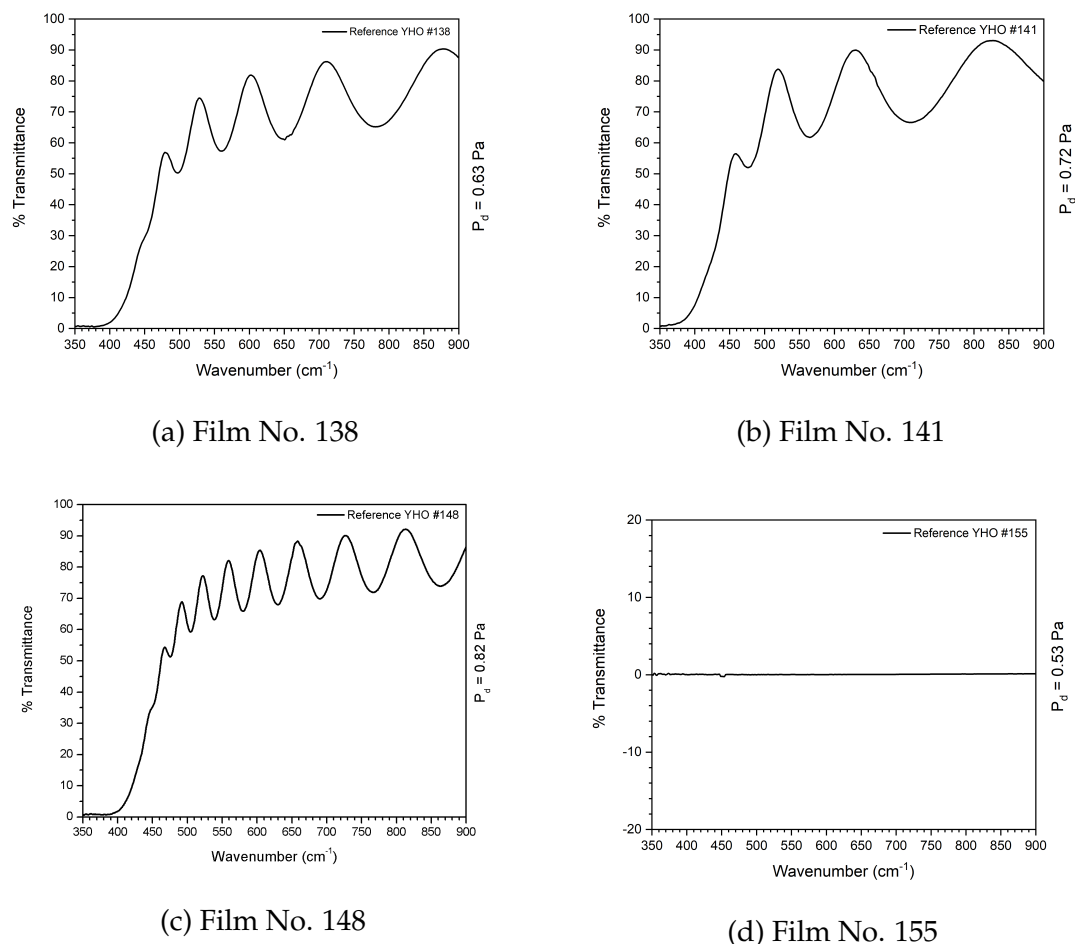


Figure 4.19: IR transmittance spectra of YHO thin films No. 138 (a), 141 (b), 148 (c) and 155 (d) before UV-illumination. Film No. 155 is as we can see (d) opaque from start and does not transmit any of the incident IR light.

transparency ($\%T \approx 59$). The total photochromic performance of sample No. 141 during 2 hours of cyclic testing was determined to approximately $\Delta T = 36\%$ which is the lowest performance compared with sample No. 148 and 138.

The same cyclic measurement setup over 2 hours for sample No. 138 showed that during the first 30 minutes of UV illumination the transmittance decreased from 77% to 36%. During the next 30 minutes the film bleached back to $\approx 48\%$ transmittance before it got illuminated again. The thin film darkens much faster than it bleaches. As soon as the film was exposed to UV light the steepness of the graph shows how quickly it darkens the first couple of minutes ($t < 5$) before the curve evens out. The total photochromic performance of sample No. 138 during 2 cycles of darkening and bleaching was determined to approximately $\Delta T = 46\%$. The thin film got darker for each set of illumination which agrees with the memory effect mentioned for this compound by Baba *et al.* in ref [65].

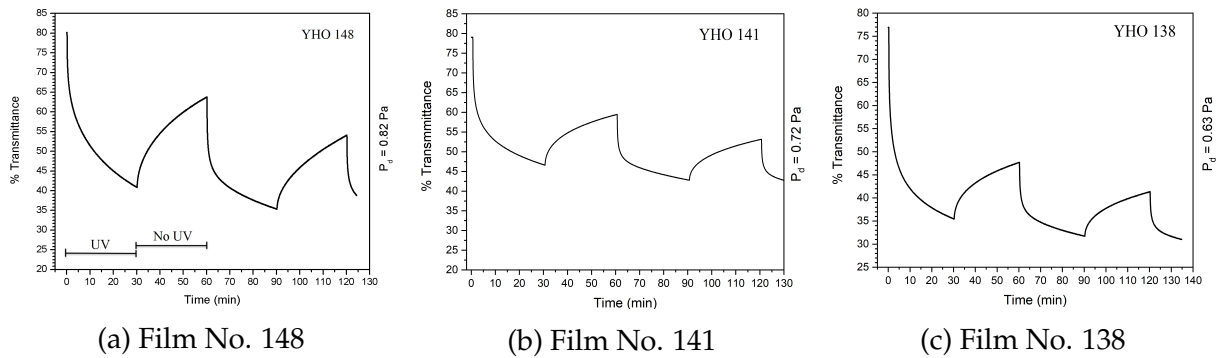


Figure 4.20: Average % transmittance between 700 and 900 cm^{-1} during 2 hours of photodarkening and bleaching of thin films No. 148 (a) and No. 138 (b) of YHO.

Comparing the cyclic optical testing of the three samples of YHO deposited at different deposition pressures we observed that the initial transparency of the samples tend to be higher for higher deposition pressures and thus higher oxygen content. This compares well with literature. Sample No. 148 deposited at 0.82 Pa showed initial % transmittance of 80 while sample No. 141 and 138 deposited at 0.72 and 0.63 Pa , respectively showed initial % transmittance of 79 and 77 , respectively. Another observation was that the amount of bleaching per time also is higher for samples with higher oxygen content. During the first bleaching of the cycle sample No. 148 increased in % transmittance by 23% while sample No. 141 and 138 had an increase of 16 and 13% , respectively, in the same part of the cycle.

4.3 Electrical measurements

Electrical measurements with the four-point probe (discussed in section 2.4) were proceeded in order to study potential changes in electrical resistivity of the Pd layer in the Pd-capped films. Sufficient changes could reveal hydrogenation of the Pd coating layer at the YHO samples. This could indicate H leaving the sample under photodarkening.

An overview of the results of the six samples is presented in Table 4.4. This table includes sample number, thickness of the Pd coating in nm, arithmetic mean of the 10 data points of measurement sets A and B for each sample before and after UV-illumination. The three right most columns show total estimated change in sheet resistance for both measurement sets. Estimation of measurement uncertainty (random error) for the two different sets, A and B, of 10 data points was calculated by taking the square root of the sum of squares of the mean standard deviation before and after UV-illumination. In Appendix D a spreadsheet containing the data of the collected measurement sets is included.

Only three out of six samples showed sufficient changes with regards to measurement uncertainty during two sets of measurements, A and B, one month apart. Sample No. TY121B coated with 50 nm Pd had a total increase in resistivity of $(0.092 \pm 0.032)\ \Omega$ for measurement set B after 1 hour and 10 minutes light soaking in the solar simulator (sec-

tion 3.2.3). Sample No. TY121A with 10 nm Pd coating had a total increase in resistivity of (0.011 ± 0.003) k Ω after light soaking for 1 hour and 30 minutes in the solar simulator for measurement set A. The last of the three samples which showed sufficient changes in resistivity for both sets A and B was sample No. TY122B coated with 5 nm Pd. This sample had most change in measured sheet resistance, but the largest measurement uncertainty. As much as 70% of the measured values from the four-point probe were not able to settle at an exact value during measurement. Therefore, the values from 7 of the measurements needed to be averaged before added to the data set of 10 measurements for this sample. A large decrease in resistivity after 1 h illumination was observed. The four-point probe measured a total decrease of (16 ± 5) M Ω in sheet resistance corresponding to a negative change in resistivity of (72.5 ± 22.7) M Ω .

Table 4.4: A summary of the electrical measurement results of Pd/YHO/glass samples. Yellow lettered values of resistance change in measurement sets A and B indicate most sufficient changes in sheet resistance with respect to total measurement uncertainty.

Sample	Pd (nm)	Before UV		After UV		Change in sheet resistance		Units
		A	B	A	B	A	B	
TY121B	50	1,78	1,77	1,80	1,79	0,018 \pm 0,004	0,020 \pm 0,007	Ω
TY121C	50	2,22	2,25	2,24	2,22	0,02 \pm 0,05	-0,03 \pm 0,03	Ω
TY120A	20	12,32	11,86	12,36	11,97	0,04 \pm 0,05	0,11 \pm 0,05	Ω
TY120C	10	0,14	0,14	0,15	0,15	0,002 \pm 0,002	0,0008 \pm 0,0009	k Ω
TY121A	10	0,12	0,11	0,12	0,11	0,0025 \pm 0,0007	0,0008 \pm 0,0005	k Ω
TY122B	5	85,81	128,97	70,09	113,27	-16 \pm 2	-16 \pm 5	M Ω

In summary, for thinner coatings of Pd we observed greater changes in sheet resistance upon illumination than for the case of thicker coating. This may indicate hydrogenation of the corresponding films. Other than this, the results show no clear trends. The total calculated uncertainties were large and varying with regards to measured values of the different samples. From this, one cannot conclude that the Pd layers were hydrogenated and that H diffuse from YHO when photodarkened. Moreover, the samples were prepared as small rectangles of each 26×25 mm² surface area. For further studies on the electrical properties of Pd/YHO/glass samples by a four-point probe it could be ideal to prepare samples with larger surface area since the area is assumed to be of infinite dimensions theoretically. Also, the sample edges can be of deficient quality and thus influence greater variation in the measurements.

4.4 XRD

4.4.1 Diffraction pattern

The XRD patterns measured for the thin films of YHO deposited at different deposition pressures are shown in Fig. 4.21. The intensity scale is arbitrary and the Bragg angle (2θ) is plotted in units of degrees. The patterns seem to match the previously measured patterns of $\text{YH}_{2+\delta}$ in ref [12]. The most striking difference between the four obtained patterns of YHO is the intensity ratio of the peaks at 29° and $33\text{-}34^\circ$ in the pattern of No. 155 and the other three samples. Sample No. 155 is the only opaque of the four and was deposited with the lowest deposition pressure. The other difference is the extra peaks at 26° and 60.6° and the absence of the peak at 70.3° for sample No. 155. The overall pattern of 155 is shifted to higher 2θ with respect to the other three patterns indicating a larger unit cell. At about 23° one can see an amorphous hallow which is particularly prominent when the patterns are normalized with respect to the most intense peak. The intensity of this hallow correlates with the film thickness being the largest for the thinnest film. Therefore, it can be explained by the contribution from the amorphous glass support.

The other three patterns have the most intense peak at about 33° for 2θ . In sample 148 this peak appears to be shifted by 0.1° with respect to the other two patterns. In fact, among the remaining three patterns sample No. 138 and 141 seem to be nearly identical differing only in the intensity of the peaks at 28.7° , 43.6° and 47.9° and slight shifts in peak positions. The XRD pattern of film No. 148 differs in the relative intensity of the most intense peak at 33.5° and all the other peaks, with exception from the peak at 70.2° which is lower in intensity compared to the other two patterns. In addition, the peaks at $\sim 64^\circ$ and 80° are missing and the peak at 30.2° is more pronounced than in the patterns of films 138 and 141. The peaks at 70.2° and 33.5° are most notably shifted for film No. 148 with respect to the similar peaks in the other patterns. Shift towards lower angles can indicate small increase in the unit cell

Table 4.5: Peak positions for the experimentally obtained patterns of YHO films by XRD.

Film No.	2theta	Remarks
155	26,3	very weak
155	29,2	most intense
148	29,0	
141	28,8	
138	28,7	
148	30,2	
141	30,0	very weak
155	33,8	
148	33,5	most intense
141	33,4	most intense
138	33,4	most intense
155	44,0	very weak
141	44,0	very weak
138	44,0	
155	48,6	possibly two peaks
148	48,1	weak
141	47,9	weak
138	47,9	
155	57,7	
148	57,1	
141	56,9	
138	56,9	possibly two peaks
155	60,6	
155	63,9	very weak
141	64,0	
138	64,0	
155	71,0	very weak
148	70,2	
141	70,0	very weak
138	70,0	very weak
155	79,0	very weak
155	98,0	
148	97,0	
141	98,0	
138	98,0	

volume. The only distinction of sample No. 148 from the other two is its thickness. The peak positions obtained in experiment are summarised in Table 4.4.1.

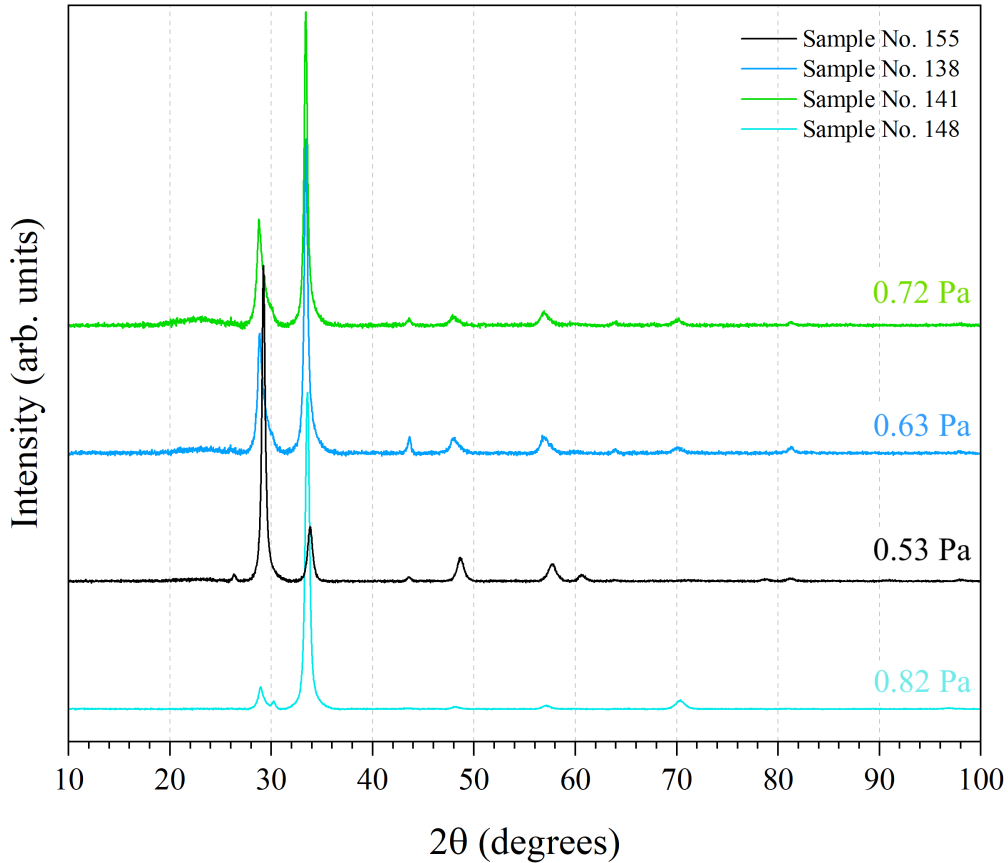


Figure 4.21: Overview of the measured x-ray diffraction patterns of four thin films of YHO deposited at different pressures ranging from 0.53 to 0.82 Pa as labeled in the diagram.

The patterns of our samples were compared with a number of reference structures. The comparison with the structures $\text{YH}_{1.94}$, YH_2 and Y_2O_3 shown in Fig. 4.23 (b) shows that some of the peaks can be explained by means of the reference structures. Difference in lattice parameters of $\text{YH}_{1.94}$ and YH_2 is evident from the shift in peak positions. The relative intensities are only corresponding well to the pattern of YHO No. 155 which is opaque like expected for YH_2 . However, the intensity of the peaks in the patterns can be affected with the preferential crystal orientation. In fact, it is possible to control the preferred crystal growth orientation by varying the deposition pressure [46]. The preferential orientation changes from (111) for film No. 155 deposited at 0.53 Pa to (200) for the films deposited at pressures higher than or equal to 0.63 Pa.

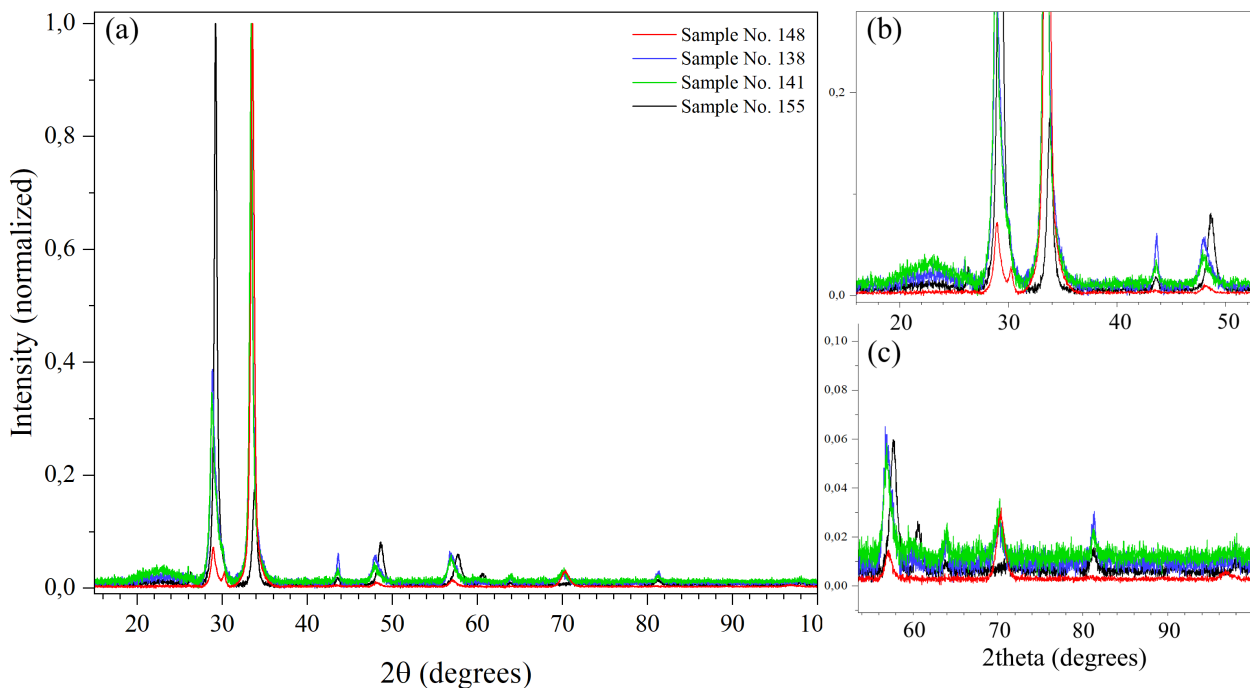


Figure 4.22: Overview of the measured x-ray diffraction patterns of YHO with normalized intensities plotted non-stacked to study shifts and intensity ratios (a). The same patterns are magnified in (b) and (c).

The theoretical pattern of YHO ($Fm\bar{4}3$) obtained in the example of section 2.5.2 has been compared to the experimental pattern as well as presented in Fig. 4.23 (a). From this comparison one sees that there are missing peaks in the theoretical pattern at approximate positions for 2θ of 26° , 30° , 44° and 64° . That is why the experimental patterns were compared to the series of 17 predicted structures of various YHO by Pishtshev *et al.* [42]. We did not find a perfect correspondence for any of the structures. Thus, none of them could perfectly explain the peaks in our experimental patterns. Because of this, we will consider that our samples crystallize as YHO ($Fm\bar{4}3$) structure with different preferred crystal orientations and a small fraction of an unknown phase responsible for the unidentified peaks. It can be recommended that the high quality patterns, preferably synchrotron, should be obtained. That can help to solve the crystal structures.

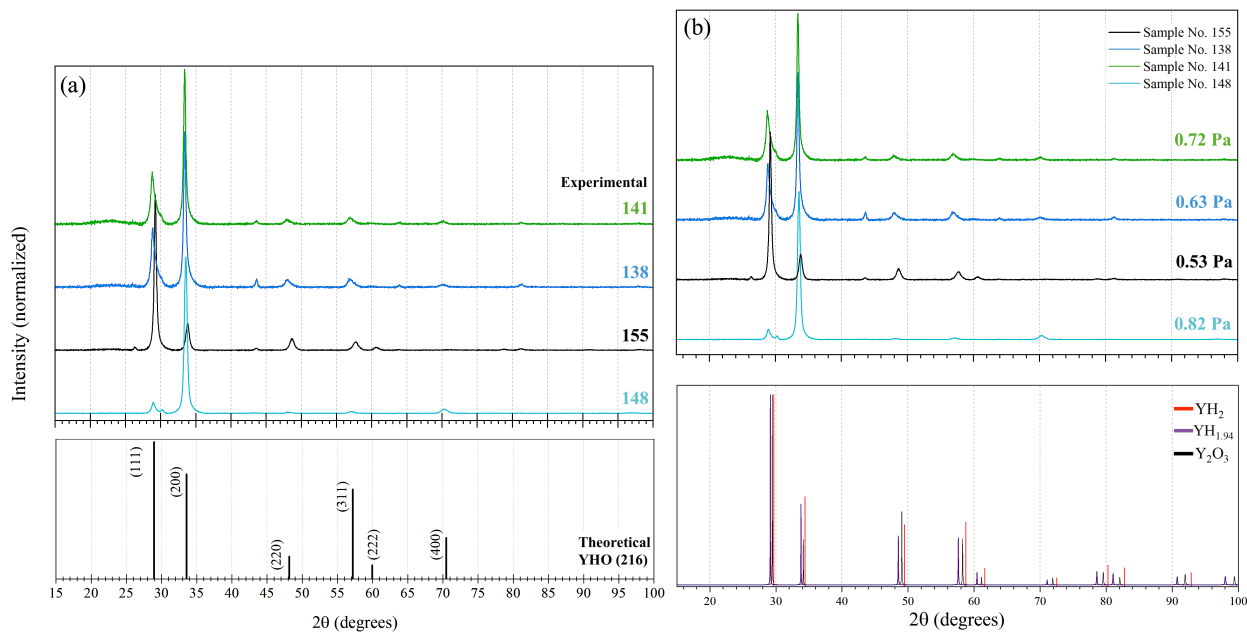


Figure 4.23: Experimental patterns of YHO compared with theoretical pattern of YHO (F43m, No. 216) (a). Experimental patterns of YHO compared with the theoretical reference patterns of YH_{1.94} (PDF 04-004-4827), YH₂ (PDF 04-006-6935) and Y₂O₃ (PDF 00-043-0661) [66]–[68] retrieved from ICDD [69](b). The intensities are normalized and the experimental patterns are stacked by a constant value.

4.4.2 Grain size estimation

The average grain size of the samples was estimated to $(158.8 \pm 3.6) \text{ \AA}$, $(157.8 \pm 3.8) \text{ \AA}$, $(136.2 \pm 2.6) \text{ \AA}$ and $(117.8 \pm 3.4) \text{ \AA}$ for sample No. 155, 138, 141 and 148, respectively. The grain size decreased consistently with increasing deposition pressure. This negatively correlated relation between the grain size and deposition pressure was also shown by Moldarev *et al.* in ref [51]. With the grain size also dependent on the sample thickness, the relation between estimated grain size (\AA), thickness (nm) and deposition pressure (Pa) is presented in a 3D scatter plot in Fig. 4.24.

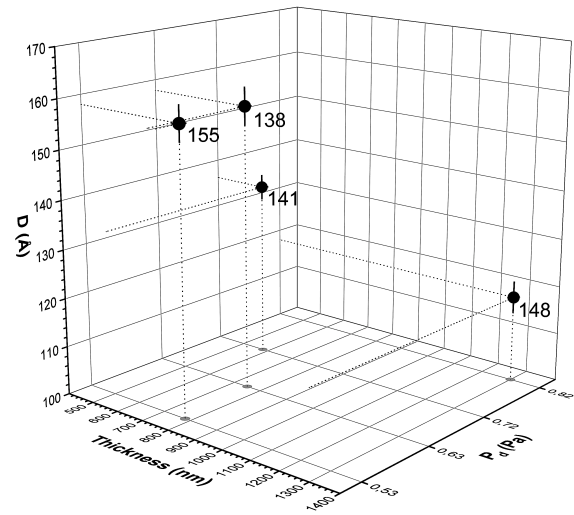
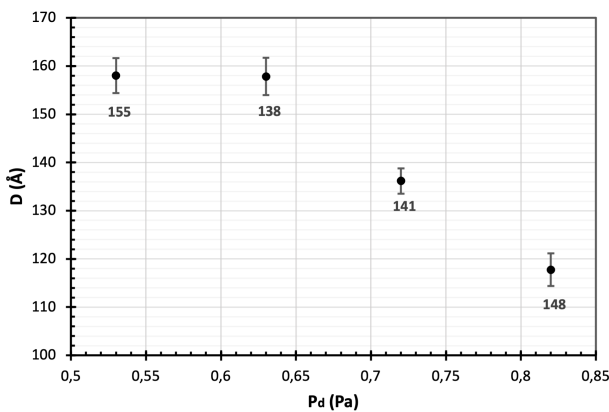
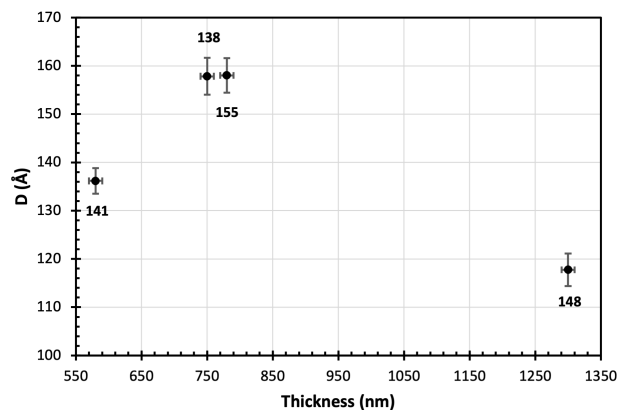


Figure 4.24: Estimated grain size average D plotted against film thickness and deposition pressure P_d . The numbered labels correspond to the sample numbers.

To study the trend of these three related variables, grain size D was plotted against one of the parameters at a time (P_d and Thickness) in 2D scatter plots with error bars shown in Fig. 4.25. From Fig. 4.25a one sees, as expected, a descending trend of the grain size with increasing deposition pressure. A clear resemblance in the grain size between two of the films was observed, with a small decrease of only 1 \AA ($= 0.1 \text{ nm}$) from film No. 155 to 138. These were the two films deposited at the lowest pressures. Between the grain size and the film thickness the plot showed no clear trend (Fig. 4.25).



(a) Grain size D plotted as a function of deposition pressure P_d .



(b) Grain size D plotted as a function of film thickness.

Figure 4.25: Estimated grain size average for thin film samples of YHO plotted as functions of deposition pressure (a) and film thickness (b).

In order to study the dependence between grain size, deposition pressure and film thickness more systematically by means of XRD methods, one should vary one parameter at a time during film preparation. This would explicitly mean to perform the deposition of thin films with the same thickness for varying pressures and to perform another deposition of thin films with varying film thickness under constant pressure.

Chapter 5

Conclusions

The purpose of this work was to study the photochromic properties of the mixed-anion compound yttrium oxyhydride by Raman spectroscopy, X-ray diffraction, cyclic optical testing and four-point probe measurements. The former three methods utilized the same thin film samples of YHO on glass, while the four-point probe measurements included a different YHO sample capped with palladium.

the Raman measurements before UV and after UV-illumination may revealed some kind of distortion of hydrogen as a result of the photochromic effect with the peak centered about 1100 cm^{-1} vanishing for the photodarkened state. Even though, this could be explained by the decreased film transparency and thus less contribution from the glass support.

Raman spectroscopy was used for studying potential changes in the chemical structure after illumination with UV-light. Some challenges were met when using the available lasers of 532 and 633 nm wavelength for the YHO/glass samples. The thin films proved to burn easily and the glass substrate showed fluorescence with the latter light source. Therefore, a great amount of time was used for optimising the measurement conditions for Raman. This optimization process showed that, for the transparent films, the large magnification objective lens gave less background signal from the glass support together with low percentage laser powers of the 532 nm laser for long acquisition times to reduce the chances of damage. The peaks were assigned by literature study to pure Y vibrations, Y-O bonds and H on tetrahedral and octahedral sites. Moreover, some of the obtained peaks corresponded well with the spectrum of glass and were thus assigned to glass. The Raman measurements before and after UV-illumination may revealed some kind of distortion of hydrogen as a result of the photochromic effect with the peak centered about 1100 cm^{-1} vanishing for the photodarkened state. Even though, this could be explained by the decreased film transparency and thus less contribution from the glass support. To overcome these shortcomings, we are planning further Raman studies: Raman study of the films deposited on CaF_2 in order to obtain spectra with less background contribution, since CaF_2 only have one, strong Raman active mode. Studies of YHO and YDO powders

in order to better assign the peaks which involve H/D (isotope exchange studies).

The cyclic optical testing was performed to measure the photochromic effect (contrast) of the thin films. The resulting transmittance spectra showed an initial % transmission of about 80% for the transparent films, whereas no transmittance for the opaque (No. 155). The total cycle of 2 hours with illumination and bleaching showed a photochromic response of 45-46% for film No. 148 and 138. The photochromic response for film No. 141 was only 36% in comparison. The overall message from the cyclic optical testing is that the photodarkening develops much faster than the bleaching process which is confirmed by observations. Also, the initial transparency of the films showed to decrease with decreasing deposition pressure.

The electrical measurements performed with a four point probe did not, with confidence, confirm a hydrogenation of the Pd coated layer due to photodarkening of the YHO thin films. There were large variations in the measurement sets and thus a high measurement uncertainty. However, if the measurements should be performed again, the sample surfaces should be larger to better assure the assumption of an infinite surface area. Also, thinner Pd coatings should be preferred, as they showed better response in the measurements.

By XRD methods we searched for the proper crystal structure by comparison to theoretical reference patterns and previous literature. This showed no perfect match to the obtained patterns. However, we assigned the F43m phase with two supplementary peaks which can indicate an additional phase. From the obtained patterns we observed a change in preferential growth orientation from the proposed (111) to the proposed (200) for deposition pressures larger than 0.53 Pa. Patterns obtained from synchrotron could be helpful for a more precise decision on the crystal structures. Grain size estimation was performed by means of the obtained data from XRD for the different films and showed a negative correlation to the deposition pressure.

The comparison of experimental diffraction patterns with theoretical patterns for different stoichiometries of YHO may have shown the possibility of multiple crystal phases present in our thin films. However, the origin for the photochromic effect in YHO thin films was not obtained in this work. Hence, further studies on the photochromic mixed anion rare-earth yttrium oxyhydride should be considered as it may be a promising material for the future with regards to e.g. energy saving smart windows [2] and efficient hydrogen sensors [1].

Bibliography

- [1] R. Westerwaal, N. Duim, I. Nieuwenhuijse, C. Perrotton, A. Dabirian, J. van Leeuwen, V. Palmisano, and B. Dam, "Thin film based sensors for a continuous monitoring of hydrogen concentrations," *Sensors and Actuators B: Chemical: international journal devoted to research and development of physical and chemical transducers*, vol. 165, no. 1, pp. 88–96, 2012, ISSN: 0925-4005.
- [2] S. Bao, K. Tajima, Y. Yamada, M. Okada, and K. Yoshimura, "Color-neutral switchable mirrors based on magnesium-titanium thin films," *Applied physics. A, Materials science & processing*, vol. 87, no. 4, pp. 621–624, 2007, ISSN: 0947-8396. DOI: 10.1007/s00339-007-3991-z.
- [3] J. Montero, A. Galeckas, and S. Z. Karazhanov, "Photoluminescence properties of photochromic yttrium hydride films containing oxygen," *physica status solidi (b)*, vol. 255, no. 8, 1 800 139–n/a, 2018, ISSN: 0370-1972.
- [4] H. Kageyama, K. Hayashi, K. Maeda, Z. Attfield J. Hiroi, J. M. Rondinelli, and K. R. Poeppelmeier, "Expanding frontiers in materials chemistry and physics with multiple anions," *Nature Communications*, vol. 9, p. 772, 2018. DOI: 10.1038/s41467-018-02838-4.
- [5] S. Cornelius, G. Colombi, F. Nafezarefi, H. Schreuders, R. Heller, F. Munnik, and B. Dam, "Oxyhydride nature of rare-earth-based photochromic thin films," *The journal of physical chemistry letters*, vol. 10, no. 6, pp. 1342–1348, 2019, ISSN: 1948-7185.
- [6] A. Pishtshev and S. Z. Karazhanov, "Role of oxygen in materials properties of yttrium trihydride," *eng, Solid state communications*, vol. 194, pp. 39–42, 2014, ISSN: 0038-1098.
- [7] C. C. You, D. Moldarev, T. Mongstad, D. Primetzhofer, M. Wolff, E. S. Marstein, and S. Z. Karazhanov, "Enhanced photochromic response in oxygen-containing yttrium hydride thin films transformed by an oxidation process," *Solar Energy Materials and Solar Cells*, vol. 166, pp. 185–189, 2017. DOI: <https://doi.org/10.1016/j.solmat.2017.03.023>.

- [8] E. M. Baba, J. Montero, E. Strugovshchikov, E. Ö. Zayim, and S. Karazhanov, "Light-induced breathing in photochromic yttrium oxyhydrides," *Phys. Rev. Materials*, vol. 4, p. 025 201, 2 Feb. 2020. DOI: 10.1103/PhysRevMaterials.4.025201.
- [9] M. Moro, S. Aðalsteinsson, T. Tran, D. Moldarev, A. Samanta, and D. Primetzhofer, "Photochromic response of encapsulated oxygen-containing yttrium hydride thin films," *physica status solidi - Rapid Research Letters*, p. 2000 608, Apr. 2021. DOI: 10.1002/pssr.202000608.
- [10] J. N. Huiberts, R. Griessen, J. H. Rector, R. J. Wijngaarden, J. P. Dekker, D. G. de Groot, and N. J. Koeman, "Yttrium and lanthanum hydride films with switchable optical properties," *Nature*, vol. 380, pp. 231–234, 1996. DOI: 10.1038/380231a0.
- [11] R. Griessen, J. Huiberts, M. Kremers, A. van Gogh, N. Koeman, J. Dekker, and P. Notten, "Yttrium and lanthanum hydride films with switchable optical properties," *Journal of Alloys and Compounds*, vol. 253-254, pp. 44–50, 1997. DOI: [https://doi.org/10.1016/S0925-8388\(96\)02891-5](https://doi.org/10.1016/S0925-8388(96)02891-5).
- [12] T. Mongstad, C. Platzer Björkman, S. Karazhanov, A. Holt, J. Maehlen, and B. Hauback, "Transparent yttrium hydride thin films prepared by reactive sputtering," *Journal of Alloys and Compounds*, vol. 509, S812–S816, Feb. 2011. DOI: 10.1016/j.jallcom.2010.12.032.
- [13] J. Montero, F. A. Martinsen, M. Lelis, S. Z. Karazhanov, B. C. Hauback, and E. S. Marstein, "Preparation of yttrium hydride-based photochromic films by reactive magnetron sputtering," *Solar Energy Materials and Solar Cells*, vol. 177, pp. 106–109, 2018. DOI: <https://doi.org/10.1016/j.solmat.2017.02.001>.
- [14] C. C. You and S. Karazhanov, "Effect of temperature and illumination conditions on the photochromic performance of yttrium oxyhydride thin films," 2020. [Online]. Available: <https://doi.org/10.1063/5.0010132>.
- [15] F. Nafezarefi, H. Schreuders, B. Dam, and S. Cornelius, "Photochromism of rare-earth metal-oxy-hydrides," *Applied Physics Letters*, vol. 111, no. 10, p. 103 903, 2017. DOI: 10.1063/1.4995081.
- [16] J. Montero, F. A. Martinsen, M. García-Tecedor, S. Z. Karazhanov, D. Maestre, B. Hauback, and E. S. Marstein, "Photochromic mechanism in oxygen-containing yttrium hydride thin films: An optical perspective," *Phys. Rev. B*, vol. 95, p. 201 301, 20 Mar. 2017. DOI: 10.1103/PhysRevB.95.201301.
- [17] J. Maehlen, T. Mongstad, C. You, and S. Karazhanov, "Lattice contraction in photochromic yttrium hydride," *Journal of Alloys and Compounds*, vol. 580, S119–S121, 2013, SI: MH2012. DOI: <https://doi.org/10.1016/j.jallcom.2013.03.151>.

- [18] T. Mongstad, C. Platzer-Björkman, J. P. Maehlen, L. P. Mooij, Y. Pivak, B. Dam, E. S. Marstein, B. C. Hauback, and S. Z. Karazhanov, "A new thin film photochromic material: Oxygen-containing yttrium hydride," *Solar Energy Materials and Solar Cells*, vol. 95, no. 12, pp. 3596–3599, 2011. DOI: <https://doi.org/10.1016/j.solmat.2011.08.018>.
- [19] C. C. You, T. Mongstad, J. P. Maehlen, and S. Karazhanov, "Engineering of the band gap and optical properties of thin films of yttrium hydride," *Applied Physics Letters*, vol. 105, no. 3, p. 031910, 2014. DOI: 10.1063/1.4891175.
- [20] S. Rosnagel, "8 - sputtering and sputter deposition," in *Handbook of Thin Film Deposition Processes and Techniques (Second Edition)*, K. Seshan, Ed., Second Edition, William Andrew Publishing, 2001, pp. 319–348. DOI: <https://doi.org/10.1016/B978-081551442-8.50013-4>.
- [21] F. Shi, *Introductory Chapter: Basic Theory of Magnetron Sputtering [Online First]*. Nov. 2018. DOI: 10.5772/intechopen.80550.
- [22] M. Hughes, *What is dc sputtering?* SEMICORE Equipment, Inc. [Online], Accessed: 2020-11-11. [Online]. Available: <http://www.semicore.com/news/94-what-is-dc-sputtering>.
- [23] R. A. Cowley, "The theory of raman scattering from crystals," *Proceedings of the Physical Society*, vol. 84, no. 2, pp. 281–296, Aug. 1964. DOI: 10.1088/0370-1328/84/2/311.
- [24] C. V. Raman, "A new radiation," *Indian Journal of physics*, vol. 2, pp. 387–398, 1928.
- [25] C. V. Raman and K. S. Krishnan, "A new type of secondary radiation," *Nature*, vol. 121, pp. 501–502, 1928. DOI: 10.1038/121501c0.
- [26] F. Adar. (Jul. 2019). Understanding the hardware of a raman microscope. HORIBA Scientific, Accessed: 2021-04-14, [Online]. Available: <https://www.youtube.com/watch?v=2kriKBDhBqI>.
- [27] K. Nakamoto, *Infrared and Raman Spectra of Inorganic and Coordination Compounds*, Sixth Edition. John Wiley & Sons, Ltd, 2008, pp. 1–147. DOI: <https://doi.org/10.1002/9780470405840.ch1>.
- [28] J. Toporski, T. Dieing, and O. Hollricher, *Confocal Raman Microscopy*, ser. Springer Series in Optical Sciences. Springer Berlin Heidelberg, 2011, vol. 158, ISBN: 3-642-12522-0.
- [29] J. Hollas, *Modern Spectroscopy*. Wiley, 2013, ISBN: 9781118681602.

- [30] D. Tuschel. (Jul. 2019). Introduction to raman spectroscopy applications explained. HORIBA Scientific, Accessed: 2021-04-14, [Online]. Available: <https://www.youtube.com/watch?v=pXVSOQ0WuUY>.
- [31] D. Tuschel, "Selecting an excitation wavelength for raman spectroscopy," vol. 31, no. 3, pp. 14–23, Mar. 2016, Accessed: 2021-05-10. [Online]. Available: <https://www.spectroscopyonline.com/view/selecting-excitation-wavelength-raman-spectroscopy>.
- [32] S. W. Ellingson, *Radiation from a hertzian dipole*, Accessed: 2020-04-22, May 2020. [Online]. Available: <https://phys.libretexts.org/@go/page/24835>.
- [33] J. Ferraro, K. Nakamoto, and C. Brown, *Introductory Raman Spectroscopy (2nd ed.)* Academic Press, 2003. [Online]. Available: <https://ebookcentral.proquest.com/lib/uisbib/reader.action?docID=299529>.
- [34] G. Bertsch, "Vibrations of the atomic nucleus," *Scientific American*, vol. 248, pp. 62–73, May 1983, Provided by the SAO/NASA Astrophysics Data System. DOI: 10.1038/scientificamerican0583-62.
- [35] B. A. DeAngelis, R. E. Newnham, and W. B. White, "Factor group analysis of the vibrational spectra of crystals: A review and consolidation," *American Mineralogist: Journal of Earth and Planetary Materials*, vol. 57, no. 1-2, pp. 255–268, 1972.
- [36] A. Carsteanu, M. Rode, D. Zur, A. Borgschulte, H. Schroter, and J. Schoenes, "Short-range ordering in beta-yh₂+delta and beta-yd₂+delta thin films studied by raman spectroscopy," *Physical Review B*, vol. 69, no. 13, 2004. DOI: 10.1103/PhysRevB.69.134102.
- [37] D. K. Schroder, *Semiconductor Material and Device Characterization*, eng. Hoboken: John Wiley & Sons, Incorporated, 2015, ISBN: 0471739065.
- [38] The Editors of Encyclopaedia Britannica, "Electrical impedance," Jun. 2008, Accessed: 2021-05-06. [Online]. Available: <https://www.britannica.com/science/electrical-impedance>.
- [39] O. Zavorotynska, "Diffraction - i," X-ray and Neutron Scattering, FYS620. Lecture., Mar. 2020.
- [40] O. H. Seeck, *X-Ray Diffraction*. 2013, ISBN: 9789814303590.
- [41] Y. Waseda, *X-Ray Diffraction Crystallography: Introduction, Examples and Solved Problems*, 1st ed. 2011. Springer Berlin Heidelberg, 2011, ISBN: 1-283-08194-6.

- [42] A. Pishtshev, E. Strugovshchikov, and S. Karazhanov, "Conceptual design of yttrium oxyhydrides: Phase diagram, structure, and properties," *Crystal Growth & Design*, vol. 19, no. 5, pp. 2574–2582, 2019. DOI: 10.1021/acs.cgd.8b01596.
- [43] P. J. Brown, A. G. Fox, E. N. Maslen, M. A. O'Keefe, and B. T. M. Willis, *International Tables for Crystallography*, E. Prince, Ed. 2006, vol. C, ch. 6, pp. 555–558, ISBN: 978-1-4020-1900-5.
- [44] A. Mikrajuddin and K. Khairurrijal, "Derivation of scherrer relation using an approach in basic physics course," *Jurnal Nanosains & Nanoteknologi*, vol. 1, Jan. 2008, ISSN: 1979-0880.
- [45] C. Ulutas and C. Gumus, "Annealing effect on structural and optical properties of chemical bath deposited mns thin film," *AIP Conference Proceedings*, vol. 1722, no. 1, 2016. DOI: 10.1063/1.4944173.
- [46] E. Baba, J. Montero, D. Moldarev, M. Moro, D. Primetzhofer, S. Sartori, E. Zayim, and S. Karazhanov, "Preferential orientation of photochromic gadolinium oxyhydride films," *Molecules*, vol. 25, Jul. 2020. DOI: 10.3390/molecules25143181.
- [47] D. M. Mishra, K. Parasuraman, S. T.N., A. Singh, and E. Mohandas, "Effect of substrate temperature and oxygen partial pressure on microstructure and optical properties of pulsed laser deposited yttrium oxide thin films," *Applied Surface Science*, vol. 257, pp. 7665–7670, Jun. 2011. DOI: 10.1016/j.apsusc.2011.03.156.
- [48] R. Dahal, "X-ray studies on partially decomposed γ -mg(bh₄)₂," Master's thesis, University of Stavanger - Norway, 2020.
- [49] C. C. You, T. Mongstad, E. S. Marstein, and S. Z. Karazhanov, "The dependence of structural, electrical and optical properties on the composition of photochromic yttrium oxyhydride thin films," *Materialia*, vol. 6, p. 100307, 2019, ISSN: 2589-1529. DOI: <https://doi.org/10.1016/j.mtla.2019.100307>.
- [50] D. Moldarev, D. Primetzhofer, C. C. You, S. Z. Karazhanov, J. Montero, F. Martinsen, T. Mongstad, E. S. Marstein, and M. Wolff, "Composition of photochromic oxygen-containing yttrium hydride films," *Solar Energy Materials and Solar Cells*, vol. 177, pp. 66–69, 2018, SI:IME-12 Delft, ISSN: 0927-0248. DOI: <https://doi.org/10.1016/j.solmat.2017.05.052>.
- [51] D. Moldarev, M. Wolff, E. Baba, M. Moro, C. C. You, D. Primetzhofer, and S. Karazhanov, "Photochromic properties of yttrium oxyhydride thin films: Surface versus bulk effect," *Materialia*, vol. 11, p. 100706, Apr. 2020. DOI: 10.1016/j.mtla.2020.100706.

- [52] M. I. Aroyo, Ed., *International Tables for Crystallography*. 2016, vol. A, ch. 2, pp. 582–631. DOI: 10.1107/97809553602060000114.
- [53] R. W. G. Wyckoff, “Second edition,” *Crystal Structures*, vol. 1, pp. 239–444, 1963, Cadmium Iodide Structure. [Online]. Available: <http://www.crystallography.net/cod/9009050.html>.
- [54] H. Olijnyk, “Lattice vibrations and electronic transitions in the rare-earth metals: Yttrium, gadolinium and lutetium,” *Journal of Physics: Condensed Matter*, vol. 17, no. 1, pp. 43–52, Dec. 2004. DOI: 10.1088/0953-8984/17/1/005.
- [55] R. Bhadra, T. Brun, M. Beno, B. Dabrowski, D. Hinks, J. Liu, J. Jorgensen, L. Nowicki, A. Paulikas, I. K. Schuller, *et al.*, “Raman scattering from high- T_c superconductors,” *Physical Review B*, vol. 37, no. 10, p. 5142, 1988. DOI: 10.1103/PhysRevB.37.5142.
- [56] E. Kroumova, M. Aroyo, J. Perez-Mato, A. Kirov, C. Capillas, S. Ivantchev, and H. Wondratschek, “Bilbao crystallographic server : Useful databases and tools for phase-transition studies,” *Phase Transitions*, vol. 76, no. 1-2, pp. 155–170, 2003. DOI: 10.1080/0141159031000076110.
- [57] K. Momma and F. Izumi, “VESTA 3 for three-dimensional visualization of crystal, volumetric and morphology data,” *Journal of Applied Crystallography*, vol. 44, no. 6, pp. 1272–1276, Dec. 2011. DOI: 10.1107/S0021889811038970.
- [58] R. W. G. Wyckoff, *Crystal Structures*, vol. 1, pp. 7–83, 1963, Hexagonal closest packed, hcp, structure. [Online]. Available: <http://www.crystallography.net/cod/9008521.html>.
- [59] P. Kristin, “Materials data on y2o3 (sg:206) by materials project,” Nov. 2014. DOI: 10.17188/1201184.
- [60] P. Kristin, “Materials data on yh3 (sg:194) by materials project,” Feb. 2016. DOI: 10.17188/1200128.
- [61] H. Kierey, M. Rode, A. Jacob, A. Borgschulte, and J. Schoenes, “Raman effect and structure of yh3 and yd3 thin epitaxial films,” *Physical Review B*, vol. 63, Mar. 2001. DOI: 10.1103/PhysRevB.63.134109.
- [62] B. Lan, M.-H. Hong, S.-X. Chen, K.-D. Ye, Z.-B. Wang, G.-X. Chen, and T.-C. Chong, “Laser-ablation-induced concentric ring structures,” *Japanese Journal of Applied Physics*, vol. 42, no. Part 1, No. 8, pp. 5123–5126, 2003. DOI: 10.1143/jjap.42.5123.

- [63] L. T. Kerr, H. J. Byrne, and B. M. Hennelly, "Optimal choice of sample substrate and laser wavelength for raman spectroscopic analysis of biological specimen," *Anal. Methods*, vol. 7, pp. 5041–5052, 2015. DOI: 10.1039/C5AY00327J.
- [64] *Raman data and analysis*, Horiba Jobin Yvon Raman application Note. [Online]. Accessed: 2020-11-11. [Online]. Available: https://static.horiba.com/fileadmin/Horiba/Technology/Measurement_Techniques/Molecular_Spectroscopy/Raman_Spectroscopy/Raman_Academy/Raman_Tutorial/Raman_bands.pdf.
- [65] E. Baba, P. Weiser, E. Zayim, and S. Karazhanov, "Temperature-dependent photochromic performance of yttrium oxyhydride thin films," *physica status solidi (RRL) - Rapid Research Letters*, vol. 15, Jan. 2021. DOI: 10.1002/pssr.202000459.
- [66] S. Katagiri, N. Ishizawa, and F. Marumo, "A new high temperature modification of face-centered cubic Y_2O_3 ," *Powder Diffraction*, vol. 8, no. 1, p. 60, 1993.
- [67] D. L. Uhrich, "Measurement of the lattice constant in the dihydrides of gadolinium—yttrium alloys," *Journal of Chemical Physics*, vol. 44, pp. 2202–2203, 1966.
- [68] J. N. Daou and P. Vajda, "Hydrogen ordering and metal-semiconductor transitions in the system YH_{2+x} ," *Phys. Rev. B*, vol. 45, pp. 10 907–10 913, 19 1992. DOI: 10.1103/PhysRevB.45.10907.
- [69] S. Gates Rector and T. Blanton, "The powder diffraction file: A quality materials characterization database," *Powder Diffraction*, vol. 34, no. 4, 2019. DOI: 10.1017/S0885715619000812.

List of Figures

2.1	Simplified model of angular emission distribution for sputtered atoms [20].	11
2.2	Magnetron sputtering illustrated on the atomic scale.	12
2.3	Schematic of the DC Magnetron Sputtering. Illustration inspired by [22]. . .	12
2.4	The Stokes, anti-Stokes, Rayleigh, resonance Raman (RR) and resonance fluorescence (RF) phenomena illustrated.	15
2.5	The procedure used to find Raman active modes of a compound by factor group analysis.	19
2.6	Schematic of the Renishaw inVia Raman instrument adapted from the Renishaw user manual.	20
2.7	Illustration showing how the laser's wavelength affects CCD coverage due to the dispersion [26].	20
2.8	Schematic of the four-point probe configuration. All point probes are equally separated. The circular geometry of Eq. 2.21 is shown in the left hand side of the sample surface.	22
2.9	Geometry of two parallel x-ray beams, 1 and 2, incident on two crystal planes separated by a distance, d.	25
2.10	Diffraction peaks of YHO (216) obtained by theory. The intensity scale shows the relative intensities in the data set (Table 2.4).	28
3.1	The collection of four YHO thin films prepared by reactive magnetron sputtering. The right most sample had a photodarkened spot at the moment. The deposition pressure used for each sample increases from left to right. . .	31
3.2	Simplified overview of the cyclic optical measurement setup.	33
3.3	Setup for the UV illumination of YHO thin films in air and in glove box of before Raman measurements.	35
3.4	Picture of six Pd coated thin films of YHO used for electrical measurements with the four-point probe.	35
3.5	Geometry of the XRD setup.	36
4.1	The lowermost spectrum for metallic Y in hcp phase shows one broad peak at approximately 90 cm^{-1} . Modified to not include all the measured spectra [54].	40
4.2	Raman spectrum of Y_2O_3 shows 9 peaks in the range $100 - 700\text{ cm}^{-1}$. Modified to include less of the measured spectra of other compounds [55].	40

4.3	Raman spectra of three phases of yttrium hydride [36].	40
4.4	Unit cell structure of six different compounds relevant for the interpretation of the yttrium oxyhydride samples. The illustrations have been made using VESTA Software [57] with input data from ref [42], [53], [58]–[60] . . .	41
4.5	Visible dark spots on film No. 138 due to the lamp in the the Raman instrument.	42
4.6	Data arithmetic of the measured spectra of YHO No. 148 with objective x20 and spectra of glass made with 532 nm laser. The three panels include measured spectrum of YHO (a), measured spectrum of glass (b) and the resulting spectrum after subtracting glass from sample spectrum (c).	43
4.7	Data arithmetic of the measured Raman spectra of YHO No. 141 with objective x100 and spectra of glass made with 532 nm laser. The three panels include measured spectrum of YHO (a), measured spectrum of glass (b) and the resulting spectrum after subtracting glass from sample spectrum (c).	43
4.8	Damaged spots on thin film after Raman measurements with different percentage powers of 532 nm laser.	44
4.9	Raman measurements of YHO No. 138 made with 633 nm laser at damaged spots. The spectra for the most damaged spots (50 and 100 %) show no sample peaks. The less damaged spots (5 and 10 %) show better response of the sample in the low Raman shift region ($< 200 \text{ cm}^{-1}$).	45
4.10	Raman spectra of glass and YHO film compared when measured with 633 nm laser with the same y-scale.	46
4.11	Raman spectra of four thin films of YHO deposited at different pressures and glass (grey). The measurements were made with 532 nm laser for long acquisition time (300 s) and large magnification (x100) before any radiation with UV light. The labels show manually added peak positions. The low wave shift region has been magnified and labeled in the right hand side panel. Glass spectrum has been re-scaled in y to fit the diagram.	47
4.12	Comparison of Raman spectra of film No. 148 with different objectives with spectrum from glass.	48
4.13	Raman measurements with laser focus at three different arbitrary points on film No. 141.	50
4.14	Raman spectra of glass before and after 30 minutes UV illumination measured with 532 nm laser (a) and 633 nm laser (b).	51
4.15	Raman of clear (coloured spectrum) and photodarkened state (black spectrum) of YHO film No. 138 and 141 after 30 minutes UV-illumination in air.	52
4.16	Raman of clear (coloured spectrum) and photodarkened state (black spectrum) of YHO sample No. 148 after 30 minutes UV-illumination in an air.	53
4.17	Raman of clear (coloured spectrum) and photodarkened state (black spectrum) of YHO film No. 138 and 141 after 2-3 hours UV-illumination in an argon atmosphere.	54

4.18	Raman measurement of clear (coloured spectrum) and photodarkened state (black spectrum) of YHO sample No. 148 after 2 hours UV-illumination in an argon atmosphere.	55
4.19	IR transmittance spectra of YHO thin films No. 138 (a), 141 (b), 148 (c) and 155 (d) before UV-illumination. Film No. 155 is as we can see (d) opaque from start and does not transmit any of the incident IR light.	56
4.20	Average % transmittance between 700 and 900 cm^{-1} during 2 hours of photodarkening and bleaching of thin films No. 148 (a) and No. 138 (b) of YHO.	57
4.21	Overview of the measured x-ray diffraction patterns of four thin films of YHO deposited at different pressures ranging from 0.53 to 0.82 Pa as labeled in the diagram.	60
4.22	Overview of the measured x-ray diffraction patterns of YHO with normalized intensities plotted non-stacked to study shifts and intensity ratios (a). The same patterns are magnified in (b) and (c).	61
4.23	Experimental patterns of YHO compared with theoretical pattern of YHO (F43m, No. 216) (a). Experimental patterns of YHO compared with the theoretical reference patterns of $\text{YH}_{1.94}$ (PDF 04-004-4827), YH_2 (PDF 04-006-6935) and Y_2O_3 (PDF 00-043-0661) [66]–[68] retrieved from ICDD [69](b). The intensities are normalized and the experimental patterns are stacked by a constant value.	62
4.24	Estimated grain size average D plotted against film thickness and deposition pressure P_d . The numbered labels correspond to the sample numbers.	63
4.25	Estimated grain size average for thin film samples of YHO plotted as functions of deposition pressure (a) and film thickness (b).	63
A1	Film No. 148 measured with 532 and 633 nm lasers compared with spectrum of glass.	78
A2	Picture made in the microscopic view of thin film damages with different percentage laser powers (5-100%) with 633 and 532 nm lasers.	79
A3	The Raman spectra obtained with 633 nm laser for low laser power with x50 objective. The spectra show the Raman effect in different parts of a damaged spot by 100% 532 nm laser for 30 seconds with x50 objective. The colors of the spectra correspond to the parts shown in the picture on the right hand side	79
A4	Comparison of the UV-illumination in air with UV-illumination in Ar atmosphere and reference spectrum of film No. 138.	80
A5	Comparison of the UV-illumination in air with UV-illumination in Ar atmosphere and reference spectrum of film No. 141.	80
A6	Comparison of the UV-illumination in air with UV-illumination in Ar atmosphere and reference spectrum of film No. 148.	81

List of Tables

2.1	Meaning of the Mulliken symbols	18
2.2	Relevant objective and laser beam properties for the Raman measurements. WD is short for working distance. NA and laser spot sizes have been calculated by Eqs. 2.18 - 2.19 with $M^2 = 1$ and refractive index $n = 1.0003$	21
2.3	Position of the atoms in the unit cell of fcc YHO $F\bar{4}3m$ [42].	26
2.4	Spreadsheet for calculating the theoretical diffraction pattern of YHO (SPGN 216). The table includes explanations and notes (in blue) to the different columns.	27
3.1	Working parameters for the preparation of YHO thin films by reactive magnetron sputtering in a Leybold Optics sputter unit [13].	32
3.2	Properties of the thin films of YHO used for Raman spectroscopy, X-ray diffraction and cyclic optical testing.	32
3.3	An overview of the six Pd/YHO/glass samples measured with the four-point probe before and after UV-illumination and the chosen properties of illumination in the solar simulator for each sample.	36
4.1	Data for input to the FGA retrieved from ref [52]. WP is short for Wyckoff position and the right most column (Sym.) shows the site symmetries of the atomic positions.	39
4.2	Output data from FGA. Raman active vibrational modes determined for the atoms of different compounds.	42
4.3	Table of Raman peak positions of different, but similar compounds from literature, and suggestions on the interpretation of our spectra of YHO.	49
4.4	A summary of the electrical measurement results of Pd/YHO/glass samples. Yellow lettered values of resistance change in measurement sets A and B indicate most sufficient changes in sheet resistance with respect to total measurement uncertainty.	58
4.5	Peak positions for the experimentally obtained patterns of YHO films by XRD.	59

Appendices

A Additional Raman spectra

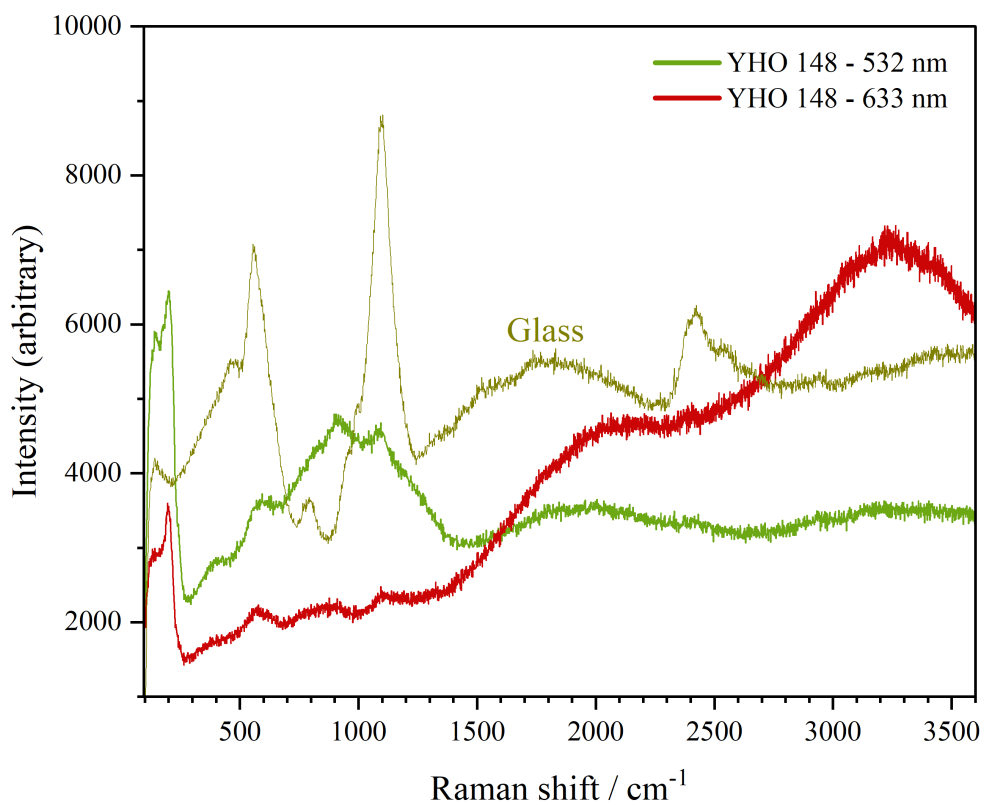


Figure A1: Film No. 148 measured with 532 and 633 nm lasers compared with spectrum of glass.

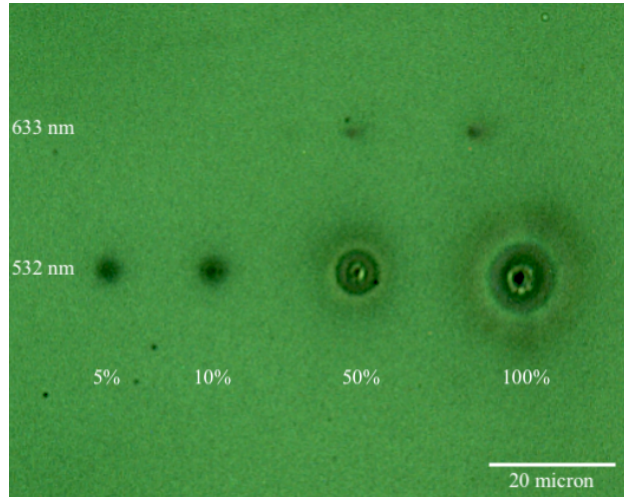


Figure A2: Picture made in the microscopic view of thin film damages with different percentage laser powers (5-100%) with 633 and 532 nm lasers.

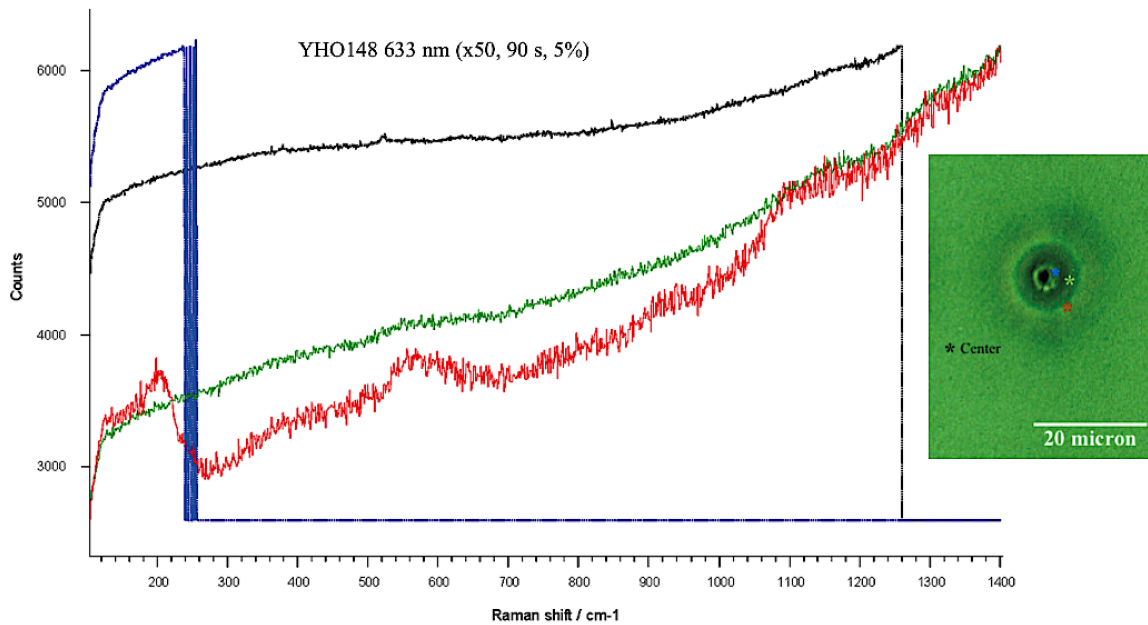


Figure A3: The Raman spectra obtained with 633 nm laser for low laser power with x50 objective. The spectra show the Raman effect in different parts of a damaged spot by 100% 532 nm laser for 30 seconds with x50 objective. The colors of the spectra correspond to the parts shown in the picture on the right hand side

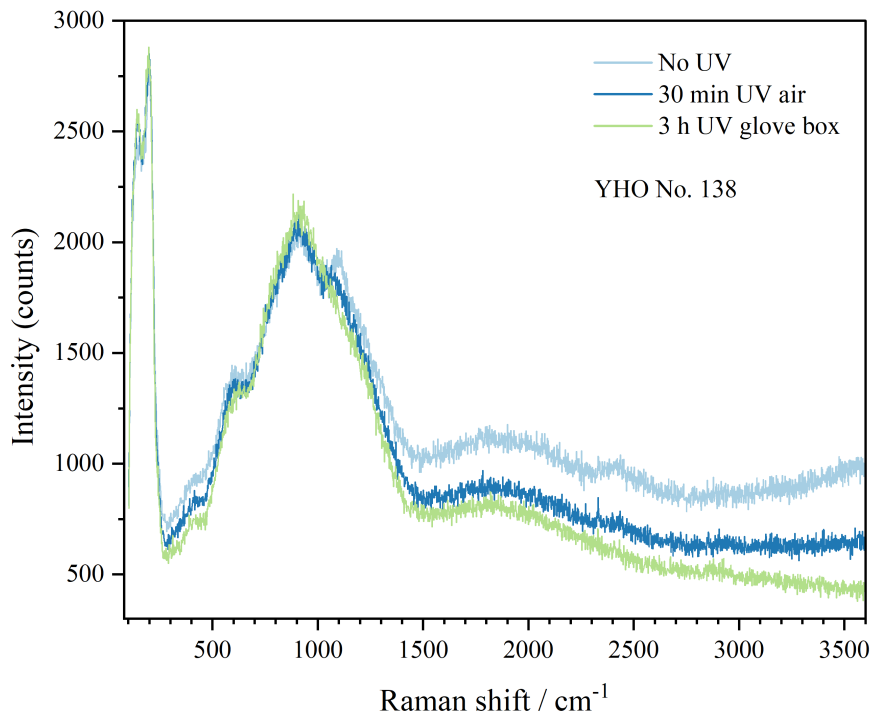


Figure A4: Comparison of the UV-illumination in air with UV-illumination in Ar atmosphere and reference spectrum of film No. 138.

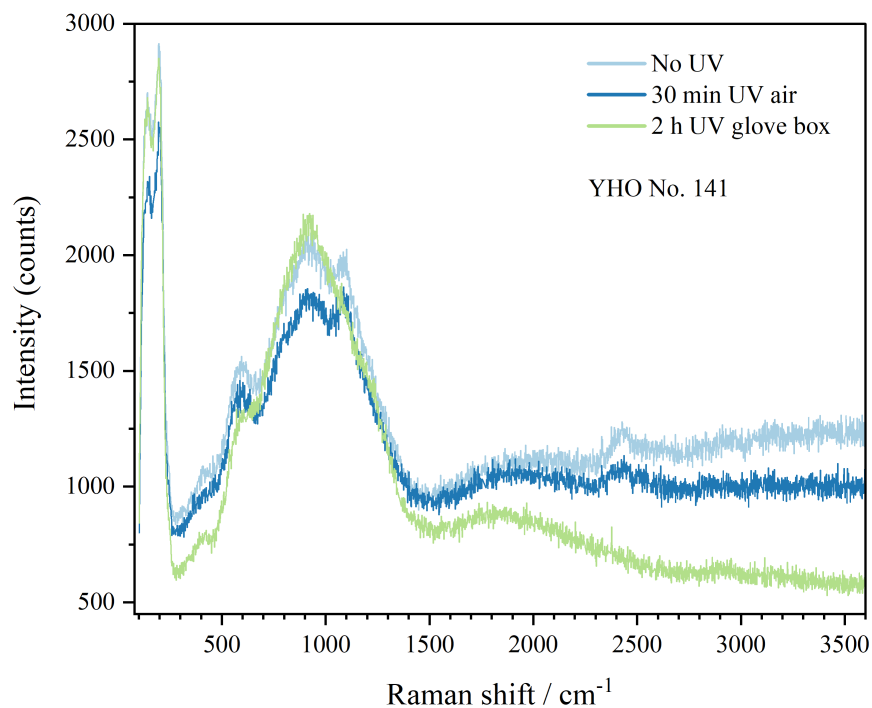


Figure A5: Comparison of the UV-illumination in air with UV-illumination in Ar atmosphere and reference spectrum of film No. 141.

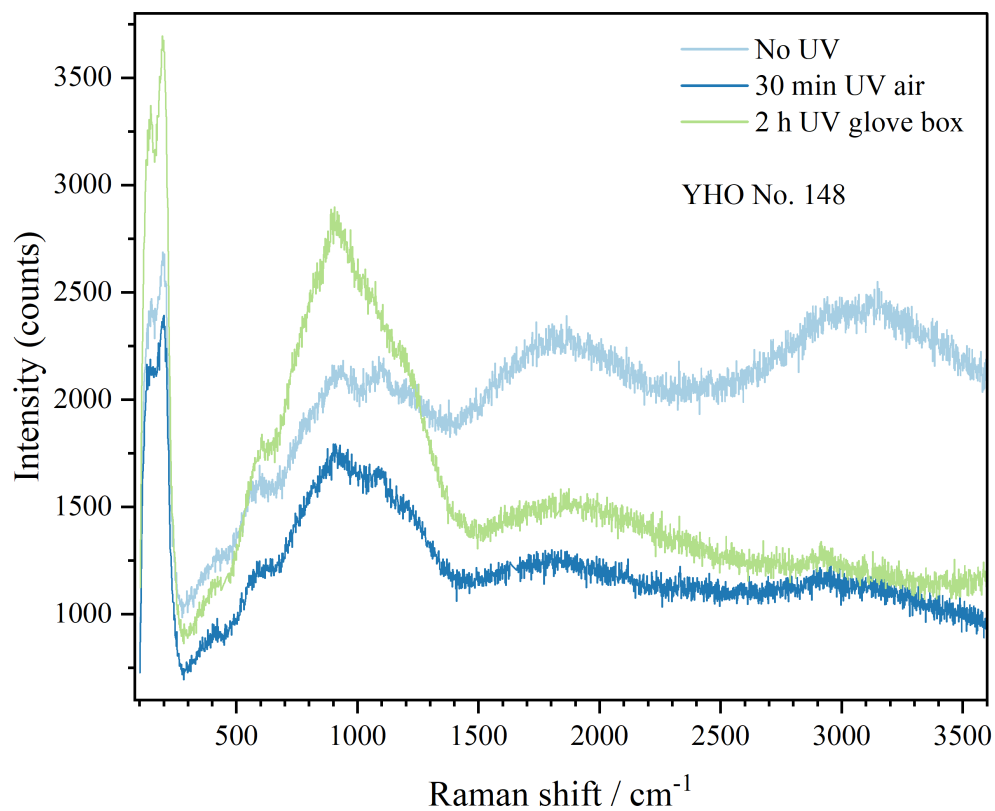


Figure A6: Comparison of the UV-illumination in air with UV-illumination in Ar atmosphere and reference spectrum of film No. 148.

B Factor group analysis

Factor group analysis

Procedure shown for Y and YH₂

Tables from

J. Ferraro, K. Nakamoto, and C. Brown, *Introductory Raman Spectroscopy (2nd ed.)* Academic Press, 2003. [Online]. Available: <https://ebookcentral.proquest.com/lib/uisbib/reader.action?docID=299529>.

Atomic coordinates from

R. W. G. Wyckoff, "Second edition," *Crystal Structures*, vol. 1, pp. 239–444, 1963, Cadmium Iodide Structure. [Online]. Available: <http://www.crystallography.net/cod/9009050.html>.

R. W. G. Wyckoff, *Crystal Structures*, vol. 1, pp. 7–83, 1963, Hexagonal closest packed, hcp, structure. [Online]. Available: <http://www.crystallography.net/cod/9008521.html>.

Metallic Y

- Hexagonal close packed (hcp)
- Space group No. 194 P6₃/mmc
- Point group D_{6h}
- $(\frac{1}{3}, \frac{2}{3}, \frac{1}{4})$ Atomic coordinates
- Site symmetry $\bar{6}m2 = D_{3h}$

D _{3h}	I	2C ₃ (z)	3C ₂	σ _h	2S ₃	3σ _v		
A' ₁	+1	+1	+1	+1	+1	+1		α _{xx} + α _{yy} , α _{zz}
A'' ₁	+1	+1	+1	-1	-1	-1		
A' ₂	+1	+1	-1	+1	+1	-1	R _z	
A'' ₂	+1	+1	-1	-1	-1	+1	T _z	(α _{xx} - α _{yy} , α _{xy}) (α _{yz} , α _{xz})
E'	+2	-1	0	+2	-1	0	(T _x , T _y)	
E''	+2	-1	0	-2	+1	0	(R _x , R _y)	

D _{6h}	C' ₂		C'' ₂		C _{6u}	C _{6h}	C' ₂		C'' ₂		σ _h → σ(xy)		C ₆	C _{3h}	C' ₂	C'' ₂	σ _v	σ _d	S ₆	D ₂
	D ₆	D _{3h}	D _{3h}	D _{3d}			D _{3d}	D _{2h}	D _{2h}											
A _{1g}	A ₁	A' ₁	A' ₁	A ₁	A _g	A _{1g}	A _{1g}	A _g	A	A'	A ₁	A ₁	A ₁	A ₁	A ₁	A ₁	A ₁	A _g	A	
A _{2g}	A ₂	A' ₂	A' ₂	A ₂	A _g	A _{2g}	A _{2g}	B _{1g}	A	A'	A ₂	A ₂	A ₂	A ₂	A ₂	A ₂	A ₂	A _g	B ₁	
B _{1g}	B ₁	A'' ₁	A'' ₁	B ₂	B _g	A _{1g}	A _{2g}	B _{2g}	B	A''	A ₁	A ₂	A ₂	A ₁	A ₁	A ₂	A ₁	A _g	B ₂	
B _{2g}	B ₂	A'' ₂	A'' ₂	B ₁	B _g	A _{2g}	A _{1g}	B _{3g}	B	A''	A ₂	A ₁	A ₁	A ₂	A ₁	A ₂	A ₂	A _g	B ₃	
E _{1g}	E ₁	E''	E''	E ₁	E _{1g}	E _g	E _g	B _{2g} + B _{3g}	E ₁	E''	E	E	E	E	E	E	E	E _g	B ₂ + B ₃	
E _{2g}	E ₂	E'	E'	E ₂	E _{2g}	E _g	E _g	A _g + B _{1g}	E ₂	E'	E	E	E	E	E	E	E	E _g	A + B ₁	
A _{1u}	A ₁	A'' ₁	A'' ₁	A ₂	A _u	A _{1u}	A _{1u}	A _u	A	A''	A ₁	A ₁	A ₂	A ₂	A ₂	A ₂	A _u	A _u	A	
A _{2u}	A ₂	A'' ₂	A'' ₂	A ₁	A _u	A _{2u}	A _{2u}	B _{1u}	A	A''	A ₂	A ₂	A ₁	A ₁	A ₁	A ₁	A ₂	A _u	B ₁	
B _{1u}	B ₁	A'' ₁	A'' ₁	B ₂	B _u	A _{1u}	A _{2u}	B _{2u}	B	A'	A ₁	A ₂	A ₁	A ₂	A ₁	A ₂	A ₁	A _u	B ₂	
B _{2u}	B ₂	A'' ₂	A'' ₂	B ₁	B _u	A _{2u}	A _{1u}	B _{3u}	B	A'	A ₂	A ₁	A ₂	A ₁	A ₂	A ₁	A ₂	A _u	B ₃	
E _{1u}	E ₁	E'	E'	E ₁	E _{1u}	E _u	E _u	B _{2u} + B _{3u}	E ₁	E'	E	E	E	E	E	E	E	E _u	B ₂ + B ₃	
E _{2u}	E ₂	E''	E''	E ₂	E _{2u}	E _u	E _u	A _u + B _{1u}	E ₂	E''	E	E	E	E	E	E	E	E _u	A + B ₁	

$$E' \rightarrow E_{2g}, E_{1u}$$

$$A_2'' \rightarrow B_{2g}, A_{2u}$$

D _{6h}	I	2C ₆ (z)	2C ₆ ² ≡ 2C ₃	C ₆ ³ ≡ C ₂	3C' ₂	3C'' ₂	σ _h	3σ _v	3σ _d	2S ₆	2S ₃	S ₆ ³ ≡ S ₂ ≡ i		
A _{1g}	+1	+1	+1	+1	+1	+1	+1	+1	+1	+1	+1	+1	R _z T _z	α _{xx} + α _{yy} , α _{zz}
A _{1u}	+1	+1	+1	+1	+1	+1	-1	-1	-1	-1	-1	-1		
A _{2g}	+1	+1	+1	+1	-1	-1	+1	+1	-1	+1	+1	+1		
A _{2u}	+1	+1	+1	+1	-1	-1	-1	+1	+1	-1	-1	-1	(R _x , R _y) (T _x , T _y)	(α _{yz} , α _{xz})
B _{1g}	+1	-1	+1	-1	+1	-1	-1	-1	+1	+1	-1	+1		
B _{1u}	+1	-1	+1	-1	+1	-1	+1	+1	-1	-1	+1	-1		
B _{2g}	+1	-1	+1	-1	-1	+1	-1	+1	-1	+1	-1	+1	(R _x , R _y) (T _x , T _y)	(α _{xx} - α _{yy} , α _{xy})
B _{2u}	+1	-1	+1	-1	-1	+1	+1	-1	+1	-1	+1	-1		
E _{1g}	+2	+1	-1	-2	0	0	-2	0	0	-1	+1	+2		
E _{1u}	+2	+1	-1	-2	0	0	+2	0	0	+1	-1	-2	(R _x , R _y) (T _x , T _y)	(α _{xx} - α _{yy} , α _{xy})
E _{2g}	+2	-1	-1	+2	0	0	+2	0	0	-1	-1	+2		
E _{2u}	+2	-1	-1	+2	0	0	-2	0	0	+1	+1	-2		

$$\Gamma = A_{2u} + B_{2g} + E_{2g} + E_{1u}$$

Raman active mode

YH2

- Face centered cubic (fcc)
- Space group No. 225 $Fm\bar{3}m$
- Point group O_h^5
- Coordinates of atoms from cif file:
 Y (0 0 0) with site symmetry $m\bar{3}m = O_h$
 H ($\frac{1}{4}$ $\frac{1}{4}$ $\frac{1}{4}$) with site symmetry $43m = T_d$
 H ($\frac{3}{4}$ $\frac{3}{4}$ $\frac{3}{4}$)

O_h	I	$8C_3$	$6C_2$	$6C_4$	$3C_4^2 \equiv 3C_2'$	$S_2 \equiv i$	$6S_4$	$8S_6$	$3\sigma_h$	$6\sigma_d$		
A_{1g}	+1	+1	+1	+1	+1	+1	+1	+1	+1	+1		$\alpha_{xx} + \alpha_{yy} + \alpha_{zz}$
A_{1u}	+1	+1	+1	+1	+1	-1	-1	-1	-1	-1		
A_{2g}	+1	+1	-1	-1	+1	+1	-1	+1	+1	-1		
A_{2u}	+1	+1	-1	-1	+1	-1	+1	-1	-1	+1		
E_g	+2	-1	0	0	+2	+2	0	-1	+2	0		$(\alpha_{xx} + \alpha_{yy} - 2\alpha_{zz}, \alpha_{xx} - \alpha_{yy})$
E_u	+2	-1	0	0	+2	-2	0	+1	-2	0		
F_{1g}	+3	0	-1	+1	-1	+3	+1	0	-1	-1	(R_x, R_y, R_z)	
F_{1u}	+3	0	-1	+1	-1	-3	-1	0	+1	+1	(T_x, T_y, T_z)	
F_{2g}	+3	0	+1	-1	-1	+3	-1	0	-1	+1		$(\alpha_{xy}, \alpha_{yz}, \alpha_{xz})$
F_{2u}	+3	0	+1	-1	-1	-3	+1	0	+1	-1		

T_d	I	$8C_3$	$6\sigma_d$	$6S_4$	$3S_4^2 \equiv 3C_2$		
A_1	+1	+1	+1	+1	+1		$\alpha_{xx} + \alpha_{yy} + \alpha_{zz}$
A_2	+1	+1	-1	-1	+1		
E	+2	-1	0	0	+2		$(\alpha_{xx} + \alpha_{yy} - 2\alpha_{zz}, \alpha_{xx} - \alpha_{yy})$
F_1	+3	0	-1	+1	-1	(R_x, R_y, R_z)	
F_2	+3	0	+1	-1	-1	(T_x, T_y, T_z)	$(\alpha_{xy}, \alpha_{yz}, \alpha_{xz})$

O_h	O	T_d	T_h	T	D_{3d}	D_{4h}	C_{3v}	D_3	$C_{3i} \equiv S_6$
A_{1g}	A_1	A_1	A_g	A	A_{1g}	A_{1g}	A_1	A_1	A_g
A_{2g}	A_2	A_2	A_g	A	A_{2g}	B_{1g}	A_2	A_2	A_g
E_g	E	E	E_g	E	E_g	$A_{1g} + B_{1g}$	E	E	E_g
F_{1g}	F_1	F_1	F_g	F	$A_{2g} + E_g$	$A_{2g} + E_g$	$A_2 + E$	$A_2 + E$	$A_g + E_g$
F_{2g}	F_2	F_2	F_g	F	$A_{1g} + E_g$	$B_{2g} + E_g$	$A_1 + E$	$A_1 + E$	$A_g + E_g$
A_{1u}	A_1	A_2	A_u	A	A_{1u}	A_{1u}	A_2	A_1	A_u
A_{2u}	A_2	A_1	A_u	A	A_{2u}	B_{1u}	A_1	A_2	A_u
E_u	E	E	E_u	E	E_u	$A_{1u} + B_{1u}$	E	E	E_u
F_{1u}	F_1	F_2	F_u	F	$A_{2u} + E_u$	$A_{2u} + E_u$	$A_1 + E$	$A_2 + E$	$A_u + E_u$
F_{2u}	F_2	F_1	F_u	F	$A_{1u} + E_u$	$B_{2u} + E_u$	$A_2 + E$	$A_1 + E$	$A_u + E_u$

$$F_{1u} \rightarrow F_{1u}$$

$$F_2 \rightarrow F_{2g} + F_{1u}$$

$$\Gamma = F_{1u} + F_{1u} + F_{2g}$$

$$= F_{2g} + 2F_{1u}$$

Raman active mode

C Grain size estimation

	A	B	C	D	E	F	G	H	I
1	Origin Pro 9 Software multiple peak analyser used for fitting experimental XRD patterns								
2									
3									
4	SAMPLE 155								
5	2theta	st.error	FWHM	st.error	D (nm)	Uncertainty	Uncertainty ^2	Avg. D (nm)	Tot. Uncertainty
6	26,3336	0,0289	0,3437	0,0681	23,7360	0,0739	0,0055	15,8022	0,3596
7	29,2357	0,0007	0,4601	0,0016	17,8448	0,0017	0,0000		
8	33,8220	0,0044	0,6232	0,0103	13,3235	0,0112	0,0001		
9	43,5804	0,0549	0,4001	0,1295	21,3852	0,1406	0,0198		
10	48,6611	0,0119	0,8103	0,0281	10,7602	0,0305	0,0009		
11	57,7091	0,0174	0,9360	0,0412	9,6911	0,0447	0,0020		
12	60,6355	0,0448	0,7067	0,1058	13,0223	0,1149	0,0132		
13	81,2503	0,1156	0,6285	0,2729	16,6544	0,2964	0,0878		
14	Reduced Chi-Sqr								
15	1,3500	Adj. R-Square							
16	0,9756								
17									
18	SAMPLE 148								
19	2theta	st.error	FWHM	st.error	D (nm)	Uncertainty	Uncertainty ^2	Avg. D (nm)	Tot. Uncertainty
20	28,9654	0,0107	0,7827	0,0253	10,4835	0,0275	0,0008	11,7755	0,3383
21	33,5422	0,0006	0,5431	0,0013	15,2775	0,0014	0,0000		
22	57,1014	0,0678	0,8155	0,1604	11,0909	0,1741	0,0303		
23	70,3062	0,0300	1,0549	0,0709	9,2106	0,0769	0,0059		
24	48,1694	0,1085	0,6791	0,2563	12,8147	0,2784	0,0775		
25	Reduced Chi-Sqr								
26	4,0249	Adj. R-Square							
27	0,9875								
28									
29	SAMPLE 141								
30	2theta	st.error	FWHM	st.error	D (nm)	Uncertainty	Uncertainty ^2	Avg. D (nm)	Tot. Uncertainty
31	28,8877	0,0042	0,9392	0,0099	8,7343	0,0108	0,0001	13,6173	0,2638

	A	B	C	D	E	F	G	H	I	
32	33,3894	0,0009	0,4619	0,0021	17,9576	0,0022	0,0000			
33	43,5596	0,0467	0,3909	0,1102	21,8876	0,1196	0,0143			
34	47,9722	0,0462	0,8254	0,1091	10,5342	0,1185	0,0140			
35	56,9426	0,0327	0,9623	0,0773	9,3911	0,0839	0,0070			
36	70,0705	0,0720	0,7351	0,1701	13,1992	0,1847	0,0341			
37	Reduced Chi-Sqr									
38	0,6873	Adj. R-Square								
39		0,9632								
40										
41	SAMPLE 138									
42	2theta	st.error	FWHM	st.error	D (nm)	Uncertainty	Uncertainty ^2	Avg. D (nm)	Tot. Uncertainty	
43	28,8877	0,0042	0,9395	0,0099	8,7319	0,0108	0,0001	15,7839	0,3845	
44	33,3894	0,0009	0,4619	0,0021	17,9564	0,0022	0,0000			
45	43,5596	0,0467	0,3918	0,1101	21,8328	0,1196	0,0143			
46	47,9723	0,0462	0,8269	0,1091	10,5153	0,1185	0,0140			
47	56,9427	0,0327	0,9635	0,0772	9,3794	0,0839	0,0070			
48	70,0705	0,0719	0,7371	0,1700	13,1632	0,1846	0,0341			
49	81,2442	0,1092	0,3621	0,2577	28,9082	0,2798	0,0783			
50	Reduced Chi-Sqr									
51	0,6872	Adj. R-Square								
		0,9632								

	A	B	C	D	E	F
1	Formulae					
2						
3	SAMPLE 155					
4	2theta	st.error	FWHM	st.error	D (nm)	Uncertainty
5	26,33364	0,02886	0,34373	0,06807	= $(0,9*0,15406)/(\text{COS}(\text{RADIANNER}(A5/2))*\text{RADIANNER}(C5))$	= $\text{ROT}(B5^2+D5^2)$
6	29,23566	0,000668611	0,46008	0,00158	= $(0,9*0,15406)/(\text{COS}(\text{RADIANNER}(A6/2))*\text{RADIANNER}(C6))$	= $\text{ROT}(B6^2+D6^2)$
7	33,82199	0,00438	0,62321	0,01034	= $(0,9*0,15406)/(\text{COS}(\text{RADIANNER}(A7/2))*\text{RADIANNER}(C7))$	= $\text{ROT}(B7^2+D7^2)$
8	43,58041	0,05487	0,40007	0,12946	= $(0,9*0,15406)/(\text{COS}(\text{RADIANNER}(A8/2))*\text{RADIANNER}(C8))$	= $\text{ROT}(B8^2+D8^2)$
9	48,66112	0,01186	0,81027	0,02805	= $(0,9*0,15406)/(\text{COS}(\text{RADIANNER}(A9/2))*\text{RADIANNER}(C9))$	= $\text{ROT}(B9^2+D9^2)$
10	57,70906	0,01741	0,93595	0,04118	= $(0,9*0,15406)/(\text{COS}(\text{RADIANNER}(A10/2))*\text{RADIANNER}(C10))$	= $\text{ROT}(B10^2+D10^2)$
11	60,63552	0,04479	0,7067	0,10582	= $(0,9*0,15406)/(\text{COS}(\text{RADIANNER}(A11/2))*\text{RADIANNER}(C11))$	= $\text{ROT}(B11^2+D11^2)$
12	81,25026	0,11555	0,62848	0,27291	= $(0,9*0,15406)/(\text{COS}(\text{RADIANNER}(A12/2))*\text{RADIANNER}(C12))$	= $\text{ROT}(B12^2+D12^2)$
13	Reduced Chi-Sqr	Adj. R-Square				
14	1,35002	0,97561				∞
15						
16						
17						
18						
19	SAMPLE 148					
20	2theta	st.error	FWHM	st.error	D (nm)	Uncertainty
21	28,96543	0,01071	0,78266	0,0253	= $(0,9*0,15406)/(\text{COS}(\text{RADIANNER}(A21/2))*\text{RADIANNER}(C21))$	= $\text{ROT}(B21^2+D21^2)$
22	33,54224	0,000550138	0,5431	0,0013	= $(0,9*0,15406)/(\text{COS}(\text{RADIANNER}(A22/2))*\text{RADIANNER}(C22))$	= $\text{ROT}(B22^2+D22^2)$
23	57,10141	0,06784	0,81545	0,16035	= $(0,9*0,15406)/(\text{COS}(\text{RADIANNER}(A23/2))*\text{RADIANNER}(C23))$	= $\text{ROT}(B23^2+D23^2)$
24	70,30622	0,02995	1,05491	0,07086	= $(0,9*0,15406)/(\text{COS}(\text{RADIANNER}(A24/2))*\text{RADIANNER}(C24))$	= $\text{ROT}(B24^2+D24^2)$
25	48,16937	0,10852	0,67905	0,25634	= $(0,9*0,15406)/(\text{COS}(\text{RADIANNER}(A25/2))*\text{RADIANNER}(C25))$	= $\text{ROT}(B25^2+D25^2)$
26	Reduced Chi-Sqr	Adj. R-Square				
27	4,02487	0,98745				

	G	H	I
1			
2			
3			
4	Uncertainty $\sqrt{2}$	Avg. D (nm)	Tot. Uncertainty
5	=F5 $\sqrt{2}$	=GIENNOMSNIIT(E5:E12)	=ROT(SUMMER(G5:G12))
6	=F6 $\sqrt{2}$		
7	=F7 $\sqrt{2}$		
8	=F8 $\sqrt{2}$		
9	=F9 $\sqrt{2}$		
10	=F10 $\sqrt{2}$		
11	=F11 $\sqrt{2}$		
12	=F12 $\sqrt{2}$		
13			
14			
15			
16			
17			
18			
19			
20	Uncertainty $\sqrt{2}$	Avg. D (nm)	Tot. Uncertainty
21	=F21 $\sqrt{2}$	=GIENNOMSNIIT(E21:E25)	=ROT(SUMMER(G21:G25))
22	=F22 $\sqrt{2}$		
23	=F23 $\sqrt{2}$		
24	=F24 $\sqrt{2}$		
25	=F25 $\sqrt{2}$		
26			
27			

D Electrical measurements data

	A	B	C	D	E	F	G	H	I
1	Electrical Measurements Data								
2	Measured value: V/I (Sheet resistance)								
3	Resistivity = (change in V/I) * $\pi/l \ln 2$								
4									
5									
6									
7	Experiment day A								
8	TY121B 50 nm Pd	Before	1 h AM1.5G	10 min UV channels					
9	1	1,7770	1,8000	1,8140	Before	1,7849	±	0,0026	Ω
10	2	1,7790	1,8040	1,8190	After 1 h AM1.5	1,8025	±	0,0028	Ω
11	3	1,7750	1,7950	1,8360					
12	4	1,7720	1,7890	1,8240					
13	5	1,7940	1,8060	1,8180	Total uncertainty	0,004	Ω		
14	6	1,7890	1,7990	1,8130					
15	7	1,7910	1,8020	1,8050					
16	8	1,7900	1,8100	1,8090	Difference	0,018	±	0,004	Ω
17	9	1,7920	1,8220	1,8140					
18	10	1,7900	1,7980	1,8140					
19	Arithmetic mean	1,7849	1,8025	1,8166	Resistivity				
20	Standard deviation	0,0082	0,0090	0,0086	$\Delta * \pi/l \ln 2$	0,080	Ω		
21	Standard dev. Mean	0,0026	0,0028	0,0027					
22									
23									
24	TY121C 50 nm Pd	Before	1 h AM1.5G	15 min UV channels					
25	1	2,0840	2,3440	2,2740	Before	2,2194	±	0,112	Ω
26	2	2,0830	2,2800	2,2710	After 1 h AM1.5	2,2422	±	0,102	Ω
27	3	2,0790	2,2870	2,3390					
28	4	2,3580	2,1040	2,3370					
29	5	2,3400	2,1080	2,3550	Total uncertainty	0,048	Ω		
30	6	2,3140	2,1050	2,1090					
31	7	2,1420	2,2720	2,1340					

	A	B	C	D	E	F	G	H	I
32	8	2,2360	2,2750	2,1250	Difference	0,02	±	0,05	Ω
33	9	2,2730	2,3920	2,1220					
34	10	2,2850	2,2550	2,3020					
35	Arithmetic mean	2,2194	2,2422	2,2368					
36	Standard deviation	0,1120	0,1024	0,1021					
37	Standard dev. Mean	0,0354	0,0324	0,0323					
38									
39									
40	TY120A 20 nm Pd	Before	1 h AM1.5G						
41	1	12,2150	12,4560		Before	12,3221	±	0,078	Ω
42	2	12,3180	12,4850		After 1 h AM1.5	12,3587	±	0,121	Ω
43	3	12,2610	12,5250						
44	4	12,4300	12,4350						
45	5	12,3030	12,2190		Total uncertainty	0,046	Ω		
46	6	12,4080	12,2920						
47	7	12,3160	12,1410						Ω
48	8	12,2280	12,3100		Difference	0,04	±	0,05	Ω
49	9	12,4290	12,3690						
50	10	12,3130	12,3550						
51	Arithmetic mean	12,3221	12,3587						
52	Standard deviation	0,0782	0,1214						
53	Standard dev. Mean	0,0247	0,0384						
54									
55									
56	TY120C 10 nm Pd	Before	1 h AM1.5G	20 min UV channels					
57	1	0,1480	0,1400	0,1480	Before	0,1443	±	0,0012	KΩ
58	2	0,1490	0,1390	0,1500	After 1 h AM1.5	0,1436	±	0,001	KΩ
59	3	0,1470	0,1380	0,1500	1 h AM1.5 + 20 min UV	0,1464	±	0,0014	KΩ
60	4	0,1490	0,1400	0,1490					
61	5	0,1460	0,1500	0,1390					

	A	B	C	D	E	F	G	H	I
62	6	0,1420	0,1490	0,1410	Total uncertainty	0,002	K Ω		
63	7	0,1420	0,1480	0,1490					
64	8	0,1410	0,1480	0,1500					
65	9	0,1390	0,1400	0,1470	Difference	0,002	\pm	0,002	K Ω
66	10	0,1400	0,1440	0,1410					
67	Arithmetic mean	0,1443	0,1436	0,1464					
68	Standard deviation	0,0039	0,0047	0,0043					
69	Standard dev. Mean	0,0012	0,0015	0,0014					
70									
71									
72	TY121A 10 nm Pd	Before	1 h AM1.5G	30 min UV channels					
73	1	0,1160	0,1200	0,1210	Before	0,1172	\pm	0,0004	K Ω
74	2	0,1160	0,1200	0,1160	After 1 h AM1.5	0,1197	\pm	0,0007	K Ω
75	3	0,1170	0,1170	0,1180	Uncertainty			0,0007	
76	4	0,1170	0,1160	0,1190	Difference	0,0025	\pm	0,0007	K Ω
77	5	0,1160	0,1220	0,1220	$\Delta * \pi/\ln 2$	0,0113	K Ω		
78	6	0,1170	0,1220	0,1220					
79	7	0,1190	0,1210	0,1210					
80	8	0,1180	0,1210	0,1220	Before	0,1172	\pm	0,000	K Ω
81	9	0,1190	0,1200	0,1190	30 min UV channels	0,1201	\pm	0,001	K Ω
82	10	0,1170	0,1180	0,1210	Uncertainty			0,001	
83	Arithmetic mean	0,1172	0,1197	0,1201	Difference	0,003	\pm	0,001	K Ω
84	Standard deviation	0,0011	0,0021	0,0020	$\Delta * \pi/\ln 2$	0,0131	K Ω		
85	Standard dev. Mean	0,0004	0,0007	0,0006					
86									
87									
88	TY122B 5nm Pd	Before	1 h AM1.5G						
89	1	85,9200	62,8750		Before	86	\pm	1,0	M Ω
90	2	85,9400	68,7500		After 1 h AM1.5	70	\pm	1	M Ω
91	3	89,8950	67,1800						
92	4	89,4400	69,1000						
93	5	84,3200	77,1750		Total uncertainty	2	M Ω		

	A	B	C	D	E	F	G	H	I
94	6	88,3300	71,6000						
95	7	81,5300	69,6600						
96	8	80,3350	67,4200		Difference	-16	±	2	MΩ
97	9	86,5750	74,7450		$\Delta * r/\ln 2$	-71,2328	MΩ		
98	10	85,7600	72,3750						
99	Arithmetic mean	85,8045	70,0880						
100	Standard deviation	3,1153	4,0822						
101	Standard dev. Mean	0,9851	1,2909						
102									
103									
104									
105									
106	Experiment day B								
107	TY121B 50 nm Pd	Before	After						Units
108	1	1,7590	1,7700						Ω
109	2	1,7940	1,7850						Ω
110	3	1,7790	1,8010						Ω
111	4	1,7690	1,7900						Ω
112	5	1,7760	1,7840						Ω
113	6	1,7800	1,8430						Ω
114	7	1,7660	1,7860						Ω
115	8	1,7650	1,7980						Ω
116	9	1,7640	1,7900						Ω
117	10	1,7700	1,7780						Ω
118	Sum	17,7220	17,9250						Ω
119	Mean	1,7722	1,7925	Difference	0,0203				Ω
120	Standard deviation	0,0102	0,0199						Ω
121	Standard dev. Mean	0,0032	0,0063	Uncertainty	0,0071				Ω
122	Representation	R_i = 1.772 ± 0.003	R_f = 1.793 ± 0.006		R_{delta} = 0.020 ± 0.007				Ω
123									

	A	B	C	D	E	F	G	H	I
124									
125	TY121C 50 nm Pd	Before	After			Units			
126	1	2,2340	2,3190			Ω			
127	2	2,2310	2,3010			Ω			
128	3	2,2310	2,2540			Ω			
129	4	2,2920	2,2440			Ω			
130	5	2,2310	2,2260			Ω			
131	6	2,2940	2,0970			Ω			
132	7	2,2220	2,0900			Ω			
133	8	2,2890	2,2330			Ω			
134	9	2,2670	2,2350			Ω			
135	10	2,2310	2,2460			Ω			
136	Sum	22,5220	22,2450			Ω			
137	Mean	2,2522	2,2245	Difference	-0,0277	Ω			
138	Standard deviation	0,0297	0,0753			Ω			
139	Standard dev. Mean	0,0094	0,0238	Uncertainty	0,0256	Ω			
140	Representation	R_i = 2.25 ± 0.01	R_f = 2.22 ± 0.02		R_{delta} = -0.03 ± 0.03	Ω			
141									
142									
143	TY120A 20 nm Pd	Before	After			Units			
144	1	11,6920	11,9760			Ω			
145	2	11,7390	12,1610			Ω			
146	3	11,9150	12,0480			Ω			
147	4	11,9210	11,7820			Ω			
148	5	11,8680	12,0220			Ω			
149	6	11,8810	12,0040			Ω			
150	7	11,8970	11,9780			Ω			
151	8	11,7980	11,9480			Ω			
152	9	11,9310	11,7680			Ω			
153	10	11,9560	12,0080			Ω			
154	Sum	118,5980	119,6950			Ω			

	A	B	C	D	E	F	G	H	I
155	Mean	11,8598	11,9695	Difference	0,1097	Ω			
156	Standard deviation	0,0879	0,1177			Ω			
157	Standard dev. Mean	0,0278	0,0372	Uncertainty	0,0464	Ω			
158	Representation	$R_{_i} = 11.86 \pm 0.03$	$R_{_f} = 11.97 \pm 0.04$		$R_{_delta} = 0.11 \pm 0.05$	Ω			
159									
160									
161	TV120C 10 nm Pd	Before	After			Units			
162	1	0,1390	0,1480			k Ω			
163	2	0,1390	0,1410			k Ω			
164	3	0,1400	0,1390			k Ω			
165	4	0,1300	0,1680			k Ω			
166	5	0,1400	0,1480			k Ω			
167	6	0,1390	0,1450			k Ω			
168	7	0,1390	0,1410			k Ω			
169	8	0,1370	0,1480			k Ω			
170	9	0,1340	0,1400			k Ω			
171	10	0,1390	0,1390			k Ω			
172	Sum	1,3760	1,4570			k Ω			
173	Mean	0,1376	0,1457	Difference	0,0081	k Ω			
174	Standard deviation	0,0032	0,0087			k Ω			
175	Standard dev. Mean	0,0010	0,0027	Uncertainty	0,0093	k Ω			
176	Representation	$R_{_i} = 0.14 \pm 0.01$	$R_{_f} = 0.15 \pm 0.03$		$R_{_delta} = 0.008 \pm 0.009$	k Ω			
177									
178									
179	TV120C 10 nm Pd	Before	After			Units			
180	1	0,1090	0,1100			k Ω			
181	2	0,1100	0,1100			k Ω			
182	3	0,1090	0,1110			k Ω			
183	4	0,1110	0,1120			k Ω			
184	5	0,1090	0,1120			k Ω			

	A	B	C	D	E	F	G	H	I
185	6	0,1090	0,1080			kΩ			
186	7	0,1110	0,1100			kΩ			
187	8	0,1110	0,1100			kΩ			
188	9	0,1090	0,1120			kΩ			
189	10	0,1100	0,1110			kΩ			
190	Sum	1,0980	1,1060			kΩ			
191	Mean	0,1098	0,1106	Difference	0,0008	kΩ			
192	Standard deviation	0,0009	0,0013			kΩ			
193	Standard dev. Mean	0,0003	0,0004	Uncertainty	0,0005	kΩ			
194	Representation	R_i = 0.1098 ± 0.0003	R_f = 0.1106 ± 0.0004		R_{delta} = 0.0008 ± 0.0005	kΩ			
195									
196									
197	TY122B 5 nm Pd	Before	Uncertainty	After	Uncertainty				Units
198	1	128,9850	1,4400	98,9050	0,2900				MΩ
199	2	125,0000	1,4100	106,2850	0,5400				MΩ
200	3	122,9300	0,9500	100,4450	0,4500				MΩ
201	4	119,8000	0,4200	112,1900	0,9100				MΩ
202	5	129,8500	1,3400	118,8450	0,8700				MΩ
203	6	126,6550	0,9970	119,3300	1,7900				MΩ
204	7	141,3500	0,9200	119,3250	2,1700				MΩ
205	8	141,3500	2,1900	119,3950	1,6300				MΩ
206	9	143,9200	1,3300	125,0850	0,5000				MΩ
207	10	109,9000	0,5700	112,9400	1,4990				MΩ
208	Sum	1289,7400	11,5670	1132,7450	10,6490				MΩ
209	Mean	128,9740	1,1567	113,2745	1,0649				MΩ
210	Standard deviation	10,7298		8,8348					MΩ
211	Standard dev. Mean	3,3931		2,7938	Difference	-15,70			MΩ
212	Total uncertainty	3,5848		2,9899	Uncertainty	4,67			MΩ
213	Representation	R_i = 129 ± 4		R_f = 113 ± 3		R_{delta} = -16 ± 5			MΩ

	A	B	C	D	E	F	G	H
1	Formulae							
2	TY122B 5 nm Pd	Before	Uncertainty	After	Uncertainty		Units	
3	1	$= (127.97+130)/2$	1,44	$= (98.7+99.11)/2$	0,29		MΩ	
4	2	$= (124+126)/2$	1,41	$= (105.9+106.67)/2$	0,54		MΩ	
5	3	$= (122.26+123.6)/2$	0,95	$= (100.13+100.76)/2$	0,45		MΩ	
6	4	$= (119.5+120.1)/2$	0,42	$= (111.55+112.83)/2$	0,91		MΩ	
7	5	$= (128.9+130.8)/2$	1,34	$= (118.23+119.46)/2$	0,87		MΩ	
8	6	$= (125.95+127.36)/2$	0,997	$= (117.8+120.86)/2$	1,79		MΩ	
9	7	$= (140.7+142)/2$	0,92	$= (117.79+120.86)/2$	2,17		MΩ	
10	8	$= (139.8+142.9)/2$	2,19	$= (118.24+120.55)/2$	1,63		MΩ	
11	9	$= (142.98+144.86)/2$	1,33	$= (124.73+125.44)/2$	0,5		MΩ	
12	10	$= (109.5+110.3)/2$	0,57	$= (111.88+114)/2$	1,499		MΩ	
13	Sum	$= \text{SUMMER}(B3:B12)$	$= \text{SUMMER}(C3:C12)$	$= \text{SUMMER}(D3:D12)$	$= \text{SUMMER}(E3:E12)$		MΩ	
14	Mean	$= B13/10$	$= C13/10$	$= D13/10$	$= E13/10$		MΩ	
15	Standard deviation	$= \text{STDAV.S}(B3:B12)$		$= \text{STDAV.S}(D3:D12)$			MΩ	
16	Standard dev. Mean	$= B15/\text{ROT}(10)$		$= D15/\text{ROT}(10)$	Difference	$= D14-B14$	MΩ	
17	Total uncertainty	$= \text{ROT}(B16^2+C14^2)$		$= \text{ROT}(D16^2+E14^2)$	Uncertainty	$= \text{ROT}(B17^2+D17^2)$	MΩ	
18	Representation	R_i = 129 ± 4		R_f = 113 ± 3		R_{delta} = -16 ± 5	MΩ	
19								
20								
21	TY121B 50 nm Pd	Before	1 h AM1.5G	10 min UV channels				
22	1	1,777	1,8	1,814		Before =B32	±	=B34
23	2	1,779	1,804	1,819		After 1 h AM1.5 =C32	±	=C34
24	3	1,775	1,795	1,836				
25	4	1,772	1,789	1,824				
26	5	1,794	1,806	1,818		Total uncertainty = $\text{ROT}(B34^2+C34^2)$	Ω	
27	6	1,789	1,799	1,813				
28	7	1,791	1,802	1,805				
29	8	1,79	1,81	1,809		Difference =F23-F22	±	=F26
30	9	1,792	1,822	1,814				
31	10	1,79	1,798	1,814				
32	Arithmetic mean	$= \text{SUMMER}(B2:B31)/10$	$= \text{SUMMER}(C2:C31)/10$	$= \text{SUMMER}(D2:D31)/10$		Resistivity		
33	Standard deviation	$= \text{STDAV.S}(B2:B31)$	$= \text{STDAV.S}(C2:C31)$	$= \text{STDAV.S}(D2:D31)$		$\Delta * \pi/\ln2$	Ω	
34	Standard dev. Mean	$= B33/\text{ROT}(10)$	$= C33/\text{ROT}(10)$	$= D33/\text{ROT}(10)$				